UNIVERSITY OF CALIFORNIA SAN DIEGO

Light Helicopter Sound for Underwater Acoustics Experiments

A dissertation submitted in partial satisfaction of the requirements for the degree Doctor of Philosophy

in

Oceanography

by

Dieter Alexander Bevans

Committee in charge:

Professor Michael J. Buckingham, Chair
Professor William A. Coles
Professor William S. Hodgkiss
Professor Jules S. Jaffe
Professor William A. Kuperman

2018

The Dissertation of Dieter Alexander Bevans is approved, and it is acceptable in quality and form for publication on microfilm and electronically:

_____

_____

_____

_____

_____

Chair

University of California San Diego

2018

DEDICATION

To my father Dr. Duane Arlo Bevans and
my mother Deseiree Dawn Maureen Easy Bevans

TABLE OF CONTENTS

LIST OF FIGURES

LIST OF TABLES

ACKNOWLEDGEMENTS

I would like to thank the chair of my committee Professor Mike Buckingham, who accepted me as a PhD student while I was still in my masters program. He used his considerable patience and expertise to guide me through the world of underwater acoustics, a new territory for me. Through his guidance I developed the skills required that made this work possible.

I would also like to thank the SIO dive locker, who provided necessary equipment and experience for the experiments conducted. I would like to extend a special thanks to Richard Walsh and Brett Pickering who assisted me during the first and second experiments. Their knowledge in conducting underwater experiments was invaluable to the experiments success. I wish to also acknowledge the expert flying by helicopter pilot Eddie Kisfaludy of SciFly, who also provided the Robinson R44 helicopters during both experiments.

I wish to thank my committee for their insights and feedback over my years as a graduate student, both in science and in life. In addition I would like to thank my friends and colleagues at SIO for their help, encouragement, and support.

Finally I wish to thank my friends and family for their tremendous support and words of wisdom that has carried me to today.

Chapters 1-6, in part, is a reprint of the material as it appears in the Journal of the Acoustical Society of America: D. A. Bevans, M. J. Buckingham, “Estimating the Sound Speed of a Shallow-water Marine Sediment from the Head Wave Excited by a Low-flying Helicopter”, 142: 2273 (2017). The dissertation author was the primary investigator and author of this manuscript, and Dr. Michael J. Buckingham directed and supervised the research.

This work was supported by the Navel Air Systems Command and Heat, Light and Sound Research, Inc. under Navy SBIR 12.2 Topic N122-122, and also by the Office of Naval Research, Ocean Acoustics, Code 322OA, under Grant No. N00014-14-1-0247. I'd also like to acknowledge The Department of Defense Science, Mathematics, and Research for Transformation Fellowship, which supported me as a graduate student.

VITA

August 19, 1980	Born in Edmonton, Alberta Canada
2012	Bachelor of Science in Physics, University of Utah
2014	Teaching Assistant, University of California San Diego
2014	Master of Science in Oceanography, Scripps Institution of Oceanography, University of California San Diego
2015-2018	SMART Scholar
2018	Doctor of Philosophy in Oceanography, Scripps Institution of Oceanography, University of California San Diego

PUBLICATIONS

T. K. Djidjou, D. A. Bevans, S. Li, A. Rogachev, *Observation of Shot Noise in Phosphorescent Organic Light-Emitting Diodes.* IEEE Transactions, 61: 3252-3257 (2014).

D. R. Barclay, M. J. Buckingham, D. A. Bevans, *The Depth Dependence of Ambient Noise in Deep Ocean Trenches.* J. Acoust. Soc. Am., 140(4): 2977-2977 (2016).

D. A. Bevans, M. J. Buckingham, *Estimating the Sound Speed of a Shallow-water Marine Sediment from the Head Wave Excited by a Low-flying Helicopter.* J. Acoust. Soc. Am., 142: 2273 (2017).

D. R. Barclay, D. A. Bevans, M. J. Buckingham, *Estimation of the geo-acoustic properties of the New England Mud Patch from the vertical coherence of the ambient noise in the water column.* IEEE J. Ocean. Eng., Submitted 2018.

CONFERENCES

D. A. Bevans, M. J. Buckingham, "The Exponential Decay of Underwater Acoustic Intensity with Increasing "Altitude of Low-Frequency Sound from a Robinson R44 Helicopter". ASA Jacksonville Meeting, 2nd-6th November 2015. *Best Student Paper*

D. A. Bevans, P. Husky, M. J. Buckingham, "A Geoacoustic Inversion Technique using the Low-Frequency "Sound from the Main Rotor of a Robinson R44 Helicopter". ASA Hawaii Meeting, 28th November – 2nd December 2016.

D. A. Bevans, M. J. Buckingham, "Head Wave Inversion Technique utilizing the Low-Frequency Sound from a Robinson R44 Helicopter". UACE2017 Greece Meeting, 3rd-8th September 2017.

D. A. Bevans, D. R. Barclay, M. J. Buckingham, "The Measurement of Muddy Sediment Properties using Ambient Noise Coherence". ASA New Orleans Meeting, 4th-8th December 2017.

FIELDS OF STUDY

Major Field: Oceanography

Studies in Theoretical and Computational Ocean Acoustics
Professors Michael J. Buckingham and William A. Kuperman

Studies in Advanced Signal Processing
Professors William A. Kuperman

Studies in Data Analysis
Professors Michael J. Buckingham, Daniel L. Ruddnick, and Sarah T. Gille

Studies in Applied Mathematics
Professors Stefan L. Llewellyn Smith and Forman A. Williams

Studies in Seismology
Professor Peter M. Shearer

Studies in Wave Physics
Professors W. Ken Melville, William A. Kuperman, Dariusz Stramski, and Peter Gerstoft

Studies in Biological Oceanography
Professors David M. Checkley, and Lisa A. Levin

Studies in Physical Oceanography
Professors Lynne D. Talley and Uwe Send

Studies in Fluid Dynamics
Myrl C. Hendershott

Studies in Chemical Oceanography
Professors Lihini I. Aluwihare and Andrew G. Dickson

ABSTRACT OF THE DISSERTATION

Light Helicopter Sound for Underwater Acoustics Experiments

by

Dieter Alexander Bevans

Doctor of Philosophy in Oceanography

University of California San Diego, 2018

Professor Michael J. Buckingham, Chair

The frequency bandwidth of the sound from a light helicopter, such as a Robinson R44, extends from about 13 Hz to 2.5 kHz. As such, the R44 has potential as a low-frequency sound source in underwater acoustics applications. To explore this idea, a series of experiments has been conducted in shallow water off the coast of southern California in which a horizontal line of hydrophones detected the sound of an R44 hovering in an end-fire position relative to the array. Some of the helicopter sound interacted with seabed to excite the head wave in the water column. A theoretical analysis of the sound field in the water column generated by a stationary airborne source leads to an expression for the two-point horizontal coherence function of the head wave, which, apart from frequency, depends only on two parameters: the horizontal separation of the two receivers and the sound speed in the sediment. By matching the zero

crossings of the measured and theoretical horizontal coherence functions, the sound speed in the sediment was recovered and found to take a value of $1682.42 \pm 16.20\ m/s$. This is consistent with the sediment type at the experiment site, which is known from a previous survey to be a fine to very- fine sand.

Chapter 1

Introduction

Shallow water marine environments are located along coastlines on the continental shelf to water depths of $200\,m$. Bounded by the air-surface interface and the seabed, these environments act as a waveguide for underwater sound. The large impedance mismatch between air and water allows for the top boundary to be treated as an ideal pressure release boundary[1]. However, this assumption breaks down in rough surface conditions for high frequencies well above the bandwidth (13 Hz – 2.5 kHz) used in this work. The water column in shallow water is often characterized by a downward refracting, or nearly isovelocity, sound-speed profile, in which case long-range propagation is exclusively via bottom-interacting paths[2]. As sound interacts with the ocean floor the physical structure and geoacoustic properties of the seabed become important.

Extensive studies[2] in theory and geoacoustic models of sound propagation in shallow water have been performed. Multiple parameters are required for a geoacoustic model, including sound speed profile of the water column, as well as sediment sound speed, attenuation, porosity and density of the sediment. Retrieving the sound speed within the water column is well established through the use of various conductivity, temperature, and depth (CTD) sensors, which have been developed for easy deployment under varying conditions. Structural and material properties of the seabed are the remaining parameters for modeling sound transmission within the waveguide[2]. The structure of the sediment may only be required to a depth of several meters for high frequencies ($> 100\,Hz$), but at lower frequencies ($\sim 10\,Hz$) the acoustic penetration depth increases requiring knowledge of the entire sediment column, including the

properties of the underlying bedrock[2]. Measuring the sediment sound speed is more difficult than measuring the water column sound speed and has challenged underwater acousticians for decades. Direct measurements, constrained to the sample area (cores, grabs, and probes), and indirect measurements of the sediment sound speed (inversions), have both been used with various degrees of success[3-5].

Direct measurements of the geoacoustic properties of marine sediments can be performed by the removal of sediment cores from a site[6]. A core is tested in a laboratory setting for porosity and density as well as acoustic properties, but is restricted to higher frequencies due to the short propagation path of their narrow cross-section. To obtain lower frequency data, in situ measurements are required. In situ measurements of sediment sound speed have been preformed, primarily with the In-Situ Sediment Geoacoustic Measurement System (ISSAMS) system[3]. This system works with probes, which act as sources and receivers of a known separation, driven into the sediment with computer controlled hydraulic rams. Sound speed and attenuation of the sediment between a set of probes can be determined by sound transmissions between two probes by time of flight and signal intensity respectively. This is typically performed at high frequencies within a $5 - 100\ kHz$ band due to the difficulties in producing and receiving compressional waves at lower frequencies, where as shear wave measurements made by ISSAMS are typically in a lower band of $300\ Hz$ to $1\ kHz$[7]. Low-frequency experiments using geophones have been performed[8, 9], but this method can have a large error[10]. Although cores and in situ measurements are ways to measure both compressional and shear speed and attenuation, they are expensive, requiring a ship capable of deployment and retrieval of the instruments, are very time consuming, and require several samples to be taken along a given propagation path.

As sound propagates in a marine environment, the acoustic signal is altered as it interacts

with the bottom. Inversion methods are used to extract this information with sources and receivers within the water column[11]. The signals received at a hydrophone array from a source can be matched to an acoustic numerical model with geoacoustic properties that provide the best fit, a technique commonly known as match-field processing[12]. This method requires a minimum number of sensor elements, requiring large expensive arrays, and the water column sound speed profile to be effective[13], but has the advantage of covering large areas of ocean. For many years, impulsive signals such as air-gun or explosive sources have been used to generate a head wave for seabed surveying[14] as well as in seismology for investigating the layering structure of the sea floor[15]. A head wave is produced when an acoustic ray incident on the sediment boundary at the critical angle is refracted to propagate horizontally through the sediment as a lateral wave. As it progresses, it radiates acoustic energy back up into the water column at the critical angle, this is known as the head wave (Figure 1.1).

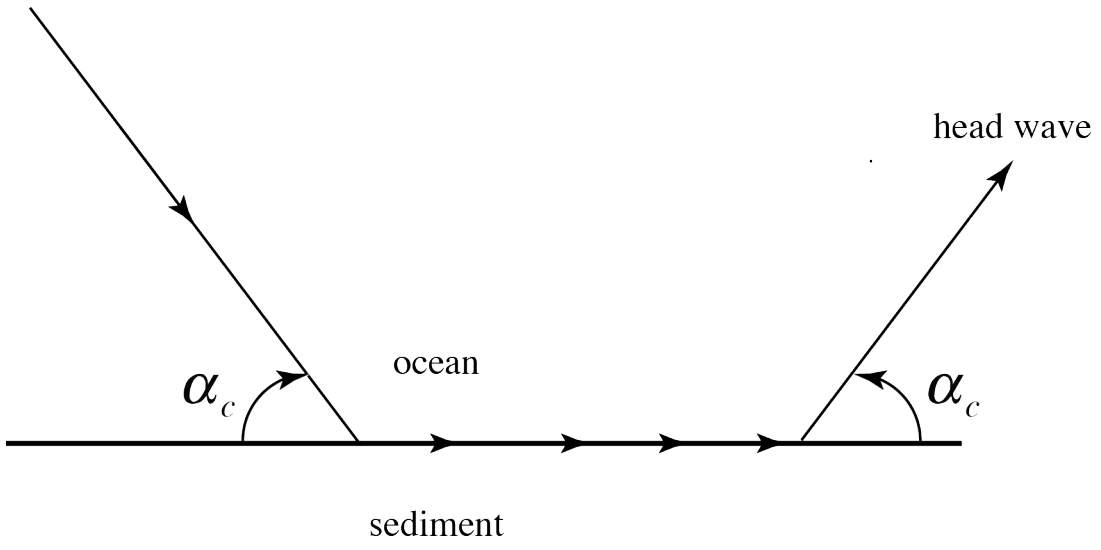

Figure 1.1: Ray schematic of the head wave produced by a ray incident on the bottom at the critical grazing angle, α_c, is refracted at the interface, travels horizontally through the sediment, and, as is progresses, radiates energy back into the water column at the critical grazing angle α_c.

Recently the head wave, although relatively weak, has been detected in surface-generated ambient noise on a vertical line array steered upwards and downwards at the critical angle of the seawater-sediment interface[16].

Theories of compressional wave and shear wave propagation in marine sediment have also been developed, the two most prominent being Buckingham's Grain-Shearing theory (GS)[17-19] and the Biot model[20, 21]. These theories both predict the logarithmic dispersion and attenuation as it scales with frequency approximate as a power law. Both models predict the attenuation of mid to high frequencies ($> 1\,kHz$) in proportion with the first power of frequency, f^1, and compare favorably with the current available data sets. However, at low frequencies, the Biot model predicts a frequency relationship of f^2, whereas the GS theory predicts the continuous first power law of frequency, f^1. Complete broadband measurements as low as several hertz, $< 100\,Hz$, are still required for theoretical model verification. Some, if not all, of these measurements could be recovered from a geoacoustic inversion in which a helicopter acts as the source of the acoustic excitation.

Until recently, little was known about the coupling of low-frequency sound generated by aircraft into the ocean. Apart from the serendipitous capture of passing aircraft sound on underwater sensors, there have been few studies where aircraft sound transmission across the air-sea interface was the subject of an experimental acoustic investigation. In 1972, Urick observed overflights of the Navy P-3 Orion fixed-wing aircraft comparing the received acoustic intensity on underwater receivers with predicted values[22]. It was not till 1992 that underwater sound from fixed-wing aircraft was used by Ferguson[23-26] to determine the aircraft velocity and altitude from the received signals. By this time the book *Marine Mammals and Noise* [27] had been published, containing a section on underwater sound from aircraft with a focus on fixed-wing aircraft with

limited detail on helicopters[27]. In 2002 the first geoacoustic inversion technique was developed using sound from light aircraft[28-30]. Using the Doppler-shifted fundamental frequency, $79\ Hz$, of the fixed-wing aircraft propeller received on a single underwater sensor to estimate the sound speed and attenuation of the very-fine sand sediment of the experiment area.

The sources of sound in helicopters include the engine, main rotor, and tail rotor producing low frequencies in the band beginning at tens of Hertz. For a two-bladed light helicopter such as the Robinson R44, the fundamental frequency of the sound from the main rotor is significantly less, $\sim 65\ Hz$, than that from the propeller of a fixed-wing, light aircraft. The slow rotation rate, several hundred revolutions per minute (RPM), of the main rotor contains frequencies as low as a few Hertz, depending on the helicopter and operating conditions. This provides a cost-effective alternative to a dedicated low-frequency in-water acoustic source, and couples into the water column and subsequent seawater-sediment interface as a head wave, Figure 1.1. In this work a theoretical analysis of the underwater sound field generated by a stationary helicopter, positioned in-line with two sensors within the water column, yields an expression for the horizontal coherence function for the head wave. This Horizontal coherence function depends on only the horizontal separation of the two sensors and the sediment sound speed. This expression for the coherence function provides a robust inversion method for recovery of the sound speed in the sediment.

1.1 Outline

Chapter 2 will characterize the sound produced by the Robinson R44 helicopter in the atmosphere and underwater. Chapter 3 presents the analytical head wave horizontal coherence model (air-water-sediment) developed for an airborne source positioned above a shallow water channel. Chapter 4 will discuss the initial helicopter experiment in a series that have been performed off the coast of Southern California 2 km north of Scripps Pier. This chapter will including two flight operations: two over-flights and 20 hovers performed by the helicopter. In Chapter 4 a serendipitous capture of the helicopter passing through the end-fire position to the array, which produced a head wave coherence function, will be discussed. Chapter 5 discusses an additional experiment that was designed and implemented to recover the sediment sound speed from the data collected on an array with the helicopter hovering at end-fire at ranges from $0 - 300\ m$ range. The chapter also discusses the fitting and error analysis of the data's horizontal coherence function zero crossings with the analytical model. In addition the data is matched to the wavenumber integration computer model SCOOTER. Closing remarks, including conclusions, applications, and possibilities of this research are presented in Chapter 6.

Chapters 1, in part, is a reprint of the material as it appears in the Journal of the Acoustical Society of America: D. A. Bevans, M. J. Buckingham, "Estimating the Sound Speed of a Shallow-water Marine Sediment from the Head Wave Excited by a Low-flying Helicopter", 142: 2273 (2017). The dissertation author was the primary investigator and author of this manuscript, and Dr. Michael J. Buckingham directed and supervised the research.

References

1. L. E. Kinsler, A. R. Frey, A. B. Coppens, et al., *Fundamentals of Acoustics*, Third ed. (John Wiley, New York, 1982).

2. F. B. Jensen, W. A. Kuperman, M. B. Porter, et al., *Computational Ocean Acoustics*. (American Institute of Physics, New York, 1994).

3. A. Barbagelata, M. Richardson, B. Miaschi, et al., in *Shear Waves in Marine Sediments*, edited by J. M. Hovem, M. D. Richardson and R. D. Stoll (Kluwer, Dordrecht, 1991), pp. 305-312.

4. M. J. Buckingham and M. D. Richardson,"On tone-burst measurements of sound speed and attenuation in sandy marine sediments", IEEE J. Ocean. Eng. **27** (3), 429-453 (2002).

5. E. I. Thorsos, K. L. Williams, N. P. Chotiros, et al.,"An overview of SAX99: acoustic measurements", IEEE J. Ocean. Eng. **26** (1), 4-25 (2001).

6. E. L. Hamilton, presented at the Physics of Sound in Marine Sediments, Austin, Texas, 1973 (unpublished).

7. K. M. Lee, M. S. Ballard, A. R. McNeese, et al.,"In situ measurements of sediment acoustic properties in Currituck Sound and comparison to models", J. Acoust. Soc. Am., **140** (5), 3593-3606 (2016).

8. R. D. Stoll,"Velocity dispersion in water-saturated granular sediment", J. Acoust. Soc. Am., **111** (No. 2), 785-793 (2002).

9. M. D. Richardson, K. B. Briggs, D. L. Bibee, et al.,"Overview of SAX99: environmental considerations", IEEE J. Ocean. Eng. **26** (1), 26-53 (2001).

10. K. L. Williams, D. R. Jackson, E. I. Thorsos, et al.,"Comparison of sound speed and attenuation measured in a sandy sediment to predictions based on the Biot theory of porous media", IEEE J. Ocean. Eng. **27** (3), 413-428 (2002).

11. A. Tolstoy, N. R. Chapman and G. Brooke,"Workshop '97: benchmarking for geoacoustic inversion in shallow water", Journal of Computational Acoustics **6** (1 & 2), 1-28 (1998).

12. H. P. Bucker,"Use of calculated sound fields and matched-field detection to locate sound sources in shallow water", J. Acoust. Soc. Am., **59**, 368-373 (1976).

13. A. Tolstoy,"Sensitivity of matched field processing to sound-field profile mismatch for vertical arrays in a deep water Pacific environment", J. Acoust. Soc. Am., **85** (6), 2394-2404 (1989).

14. M. V. Hall,"Measurement of seabed sound speeds from head waves in shallow water", IEEE J. Ocean. Eng. **21** (4), 413-422 (1996).

15. K. Aki and P. G. Richards, *Quantitative Seismology*. (University Science Books, 2002).

16. J. Gebbie and M. Siderius,"Head wave correlations in ambient noise", J. Acoust. Soc. Am., **140** (1), EL62-EL66 (2016).

17. M. J. Buckingham,"The Viscous Grain-Shearing (VGS) theory of wave propagation in marine sediments", J. Acoust. Soc. Am., **123** (No. 5, Pt. 2), 3440 (2008).

18. M. J. Buckingham,"Wave propagation, stress relaxation, and grain-to-grain shearing in saturated, unconsolidated marine sediments", J. Acoust. Soc. Am., **108** (6), 2796-2815 (2000).

19. M. J. Buckingham,"Extension of the grain-shearing theory of wave propagation in marine sediments to include pore-fluid viscosity", J. Acoust. Soc. Am., **122** (N0. 5, Pt. 2), 2974 (2007).

20. M. A. Biot,"Theory of propagation of elastic waves in a fluid-saturated porous solid: I. Low-frequency range", J. Acoust. Soc. Am., **28** (2), 168-178 (1956).

21. M. A. Biot,"Theory of propagation of elastic waves in a fluid-saturated porous solid: II. Higher frequency range", J. Acoust. Soc. Am., **28** (2), 179-191 (1956).

22. R. J. Urick,"Noise signature of an aircraft in level flight over a hydrophone in the sea", J. Acoust. Soc. Am., **52** (No. 3, Pt. 2), 993-999 (1972).

23. B. G. Ferguson,"A ground-based narrow-band passive acoustic technique for estimating the altitude and speed of a propeller-driven aircraft", J. Acoust. Soc. Am., **92** (3), 1403-1407 (1992).

24. B. G. Ferguson,"Doppler effect for sound emitted by a moving airborne source and received by acoustic sensors located above and below the sea surface", J. Acoust. Soc. Am., **94** (6), 3244-3247 (1993).

25. B. G. Ferguson and B. G. Quinn,"Application of the short-time Fourier transform and the Wigner-Ville distribution to the acoustic localization of aircraft", J. Acoust. Soc. Am., **96** (2), 821-827 (1994).

26. B. G. Ferguson,"Time-frequency analysis of hydrophone data", IEEE J. Ocean. Eng. **21** (4), 537-544 (1996).

27. W. J. Richardson, C. R. Greene Jr., C. I. Malme, et al., *Marine Mammals and Noise*. (Academic Press, New York, 1995).

28. M. J. Buckingham and E. M. Giddens,"Estimating the low-frequency (0.1 - 1 kHz) sound speed in marine sediments using the harmonics from the propeller of a light aircraft", J. Acoust. Soc. Am., **113** (4, Pt. 2), 2203-2204 (2003).

29. E. M. Giddens and B. M. J.,"Geoacoustic inversions in shallow water using Doppler-shifted modes from a moving source", J. Acoust. Soc. Am., **116** (4, Pt. 2), 2557 (2004).

30. M. J. Buckingham and E. M. Giddens,"Inversions of underwater sound from a high-Doppler airborne source (a light aircraft) for the geoacoustic properties of the sea bed", J. Acoust. Soc. Am., **118** (No. 3, Pt. 2), 1845 (2005).

Chapter 2

In-Air and Underwater Sound from a Robinson R44 Helicopter

2.1 Introduction

The Robinson R44 helicopter was the chosen helicopter in a series of experiments performed in shallow-water off the coast of Del Mar, California. Being a light helicopter, with a reciprocating engine, it is highly maneuverable and inexpensive to operate. In this Chapter the general dynamics of helicopter sound will be covered, from its acoustic signature in air as well as its acoustic signature after transmission into a shallow-water waveguide. The frequency characteristics of the sound producing elements of helicopters will be discussed, along with the propagation of the sound through the air-sea interface. The propagation of the transmitted sound within the underwater waveguide will also be discussed with emphasis on the head wave within the water column produced by the in flight helicopter. This will provide an in-depth understanding of the acoustic field produced by the Robinson R44 helicopter before an analytic solution for the head wave horizontal coherence function is presented in Chapter 3.

2.2 Robinson R44 Helicopter Sound

The engine, the drive train, the main and tail rotor, and the airframe all produce sound in Robinson R44 light helicopter. However, the main sources of sound in flight, at low frequencies

$(1 - 500\,Hz)$, are the reciprocating engine and the two rotors. The engine, which typically operates at ~ 2700 revolutions per minute (RPM), supplies the energy to the main and tail rotor. Reduction gearboxes convert the high rotation rate from the engine to lower rates for the main and tail rotor. The slow rotation rate, several hundred RPM, of the main rotor produces sound with frequencies as low as a few Hertz, providing a cost-effective, highly mobile alternative to a conventional low frequency in water acoustic source. However, the use of a helicopter as an acoustic source is not without drawbacks. The helicopter's acoustic signature is uncontrolled, and although it is a continuous-wave source its frequency characteristics are not constant, with the harmonics varying slightly in frequency with the changing pitch of the main rotor blades to change altitude. In addition, the mobility comes with a limited flight range, restricting helicopter operation to shallow-water coastal regions. However, in these coastal regions the underwater acoustic field is largely dependent on the seabed boundary condition, making the geo-acoustic properties of the seabed important input parameters in ocean-acoustic propagation models[1].

The Robinson R44 is a 4-seater light helicopter with a 2-blade, 10.06 m diameter main rotor and 1.5 m tail rotor. The R44 is powered by a Lycoming six-cylinder horizontal opposed, air-cooled, normally aspirated reciprocating engine, that when operated at a maximum cruise power rotates at 2718 RPM[2] with a maximum continuous power rating of 205 bhp. Reduction gearboxes feed power to the main and tail rotor resulting in operating RPMs of 408 and 2448[2] respectively, given the tail-to-main rotation rate of roughly 6:1. The engine and rotors are rotational sources of sound producing a fundamental frequency plus high-order harmonics which are multiples of the fundamental[3]. The dominant source of sound from the engine comes from the firing of the cylinders. The fundamental frequency of a reciprocating engine is given by[4],

$$f_{eng} = \frac{RC}{60N} \tag{2.1}$$

where R is the RPM, C is the number of cylinders, and N is the number of rotations per firing per cylinder. For a four-stroke engine the number of rotations of the crankshaft for each firing of a cylinder is $N = 2$, the number of cylinders in the R44 helicopter is $C = 6$, and at a constant RPM of 2718 results in a fundamental frequency of 136 Hz with harmonics being multiples of this at frequencies of 272 Hz, 408 Hz, etc.

In flight, the engine produces a significant level of noise with contributions from the main rotor and tail rotor. The pitch of the main rotor blades is the mechanism that creates the lift required for the helicopter to remain airborne. This differs from a fix-wing aircraft where the lift arises by the difference in pressure above and below the wing. The fundamental frequency for the main and tail rotor are found from the same expression as for a aircraft propeller:[4]

$$f_{rotor} = \frac{RB}{60} \tag{2.2}$$

where R is the RPM and B is the number of blades on the rotor. For the 2-blade main rotor of the Robinson R44 helicopter rotating at the load operating RPM=408 results in a fundamental frequency of 13.6 Hz with harmonics being multiples the fundamental at 27.2 Hz, 40.8 Hz …136 Hz … 272 Hz, etc. For comparison, the fundamental frequency from a two-bladed propeller on a typical fixed-wing light aircraft[5-10], at around 80 Hz, is approximately a factor of 6 higher than that of the R44 helicopter main rotor. The pitch of the tail rotor blades maintains the yaw of the helicopter, although not a significant source of sound compared to the engine or main rotor, the tail rotor still produces a fundamental frequency of 81 Hz with harmonics of 162 Hz, 243 Hz, etc.

In addition to the two rotors and reciprocating engine, the Robinson R44 helicopter produces additional sound generated by the reduction gearboxes and drivetrain, ranging from hundreds of Hz to several kHz. As the two rotors and the engine are mechanically coupled

together, certain harmonic frequencies overlap between the individual acoustic sources. For example, the fundamental frequency of the tail rotor corresponds to the 6^{th} harmonic of the main rotor and the 10^{th} harmonic of the main rotor overlaps with the fundamental frequency of the engine. Overall, the helicopter may be regarded as a broadband acoustic generator with a bandwidth extending over several decades in frequency, from about 13 Hz upward to 4 kHz.

2.3 Robinson R44 Helicopter Sound Signature in Air

The air-borne acoustic signature of a R44 helicopter hovering, above water, from an in-air ITC 6050C receiver located approximately 1 m above the sea surface is shown in Figure 2.1. The experimental setup, procedure, and instrument specifications will be detailed in Chapter 4. The first six harmonics of the main rotor are prominent in the spectrum below $100\,Hz$, diminishing in power before a sharp increase with the sixth harmonic, coinciding with the fundamental frequency of the tail rotor.

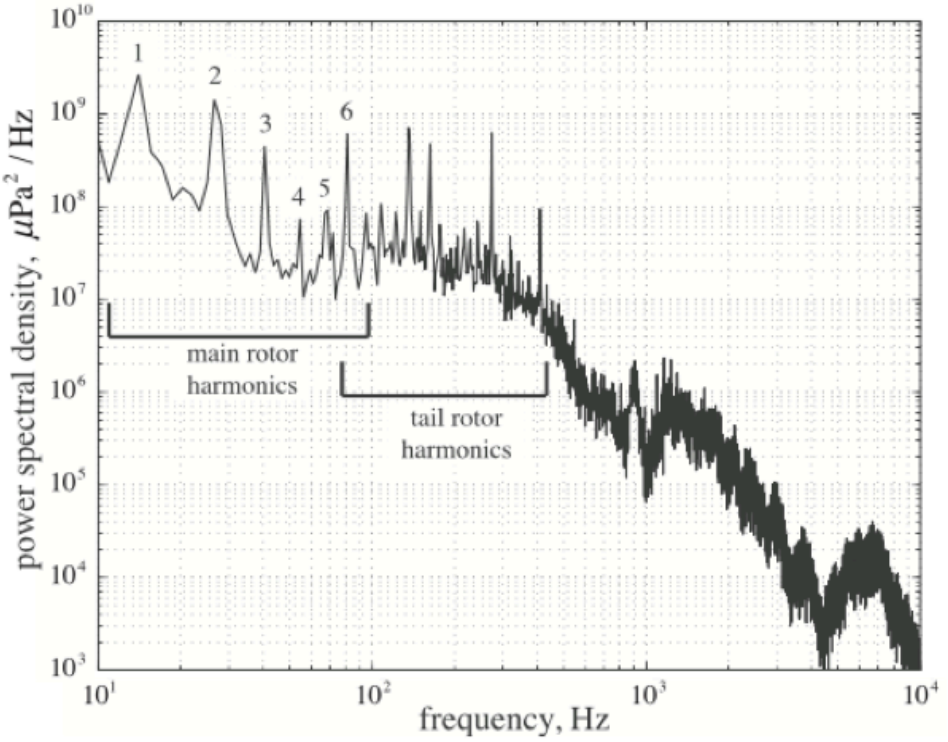

Figure 2.1: Power spectral density of the airborne sound from the hovering R44 helicopter, analysis bandwidth 1.56 Hz averaged over 6.4 s. The first main-rotor harmonics, labeled 1 to 6, are prominent below 100 Hz. The tail rotor harmonics are also discernible, a factor of 6 higher in frequency than their main-rotor counterparts.

The tail rotor harmonics continue from 80 Hz to 600 Hz and within this bandwidth, the engine harmonics contribute to the power density beginning at 136 Hz. The superposition of the engine and main rotor harmonics at 136 Hz, 272 Hz, and 408 Hz are prominent, in addition to the superposition of the tail and main rotor at 160 Hz and 240 Hz. At higher frequencies, the mechanical gearboxes and drivetrain produce spectral lines, but these are masked by broadband noise generated by interaction of a moving rotor blade with turbulent eddies (Figure 2.1). Such eddies can be shed from the blade itself, from previous rotor blades, or from natural occurrences in the atmosphere[11]. Special noise levels above 2.5 kHz decays rapidly, which places an upper frequency limit on the useful bandwidth available for underwater acoustics experiments (Figure

2.1). These features within Figure 2.1 are consistent with previous reports of the external noise spectra of light helicopters[4, 11].

2.4 Underwater Sound from a Robinson R44 Helicopter

A portion of the sound from an in-flight helicopter over water is transmitted into the water column by refraction through the air-sea interface. This transmission is restricted by Snell's Law to be within the air-sea critical angle cone[3, 4]. The air-sea critical angle cone (illustrated in red in Figure 2.2), outside of which there is no transmission for a perfectly flat air-sea interface, is 13^{O} from the vertical. However, the surface of the ocean is subject to wind forcing which creates a choppy surface. This allows sound rays incident at greater than the critical angle to surface scatter into the water column[12].

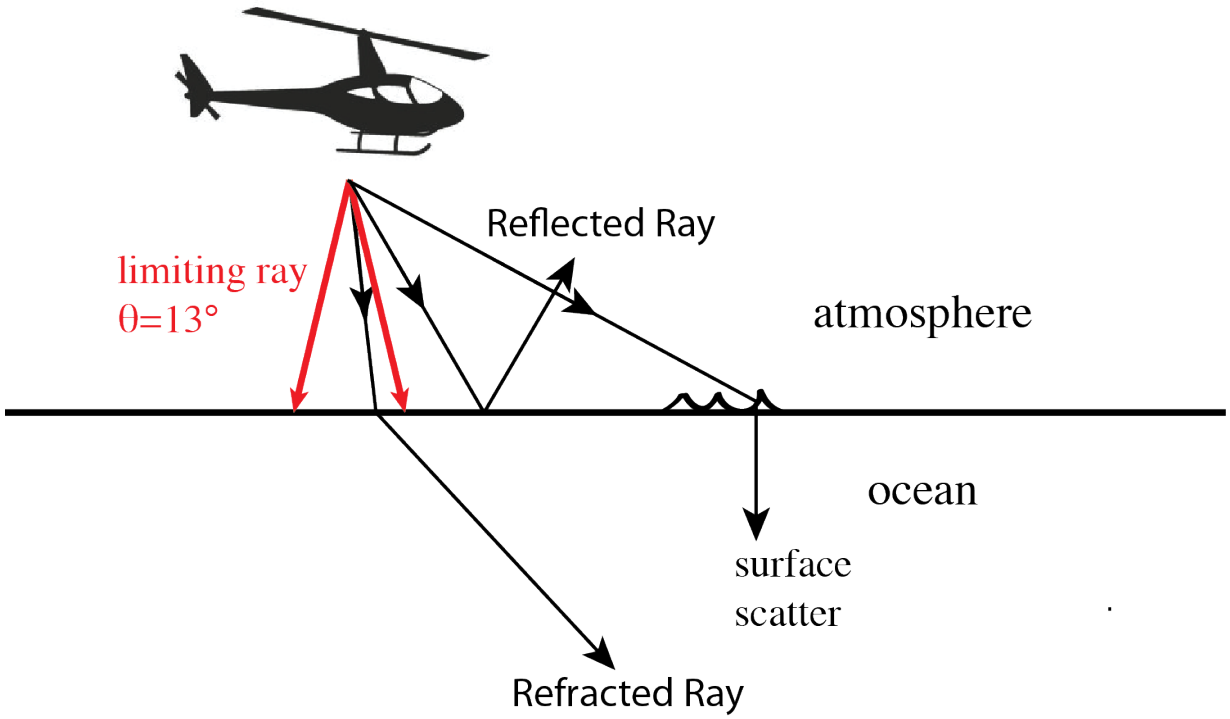

Figure 2.2: The critical angle cone between the atmosphere and ocean illustrated in red, 13° from the vertical, along with ray schematic of a refracted ray propagating into the water column and a completely reflected ray outside the critical angle cone.

The underwater spectra of the in-flight R44 helicopter, captured on a single hydrophone, on an array known as the FlyBy array, is shown in Figure 2.3. The FlyBy array is a small, diver deployable, flexible array consisting of eleven non-uniformly spaced hydrophones connected to a data acquisition (DAQ) unit capable of the simultaneously sampling of sixteen acoustic channels. In addition to the eleven underwater hydrophones, the DAQ also captures the air-borne signature just above the sea surface, as covered in the previous section (2.3). This system, which makes up the sensor station, will be extensively covered in Chapter 4, along with a detailed account of the first experiment.

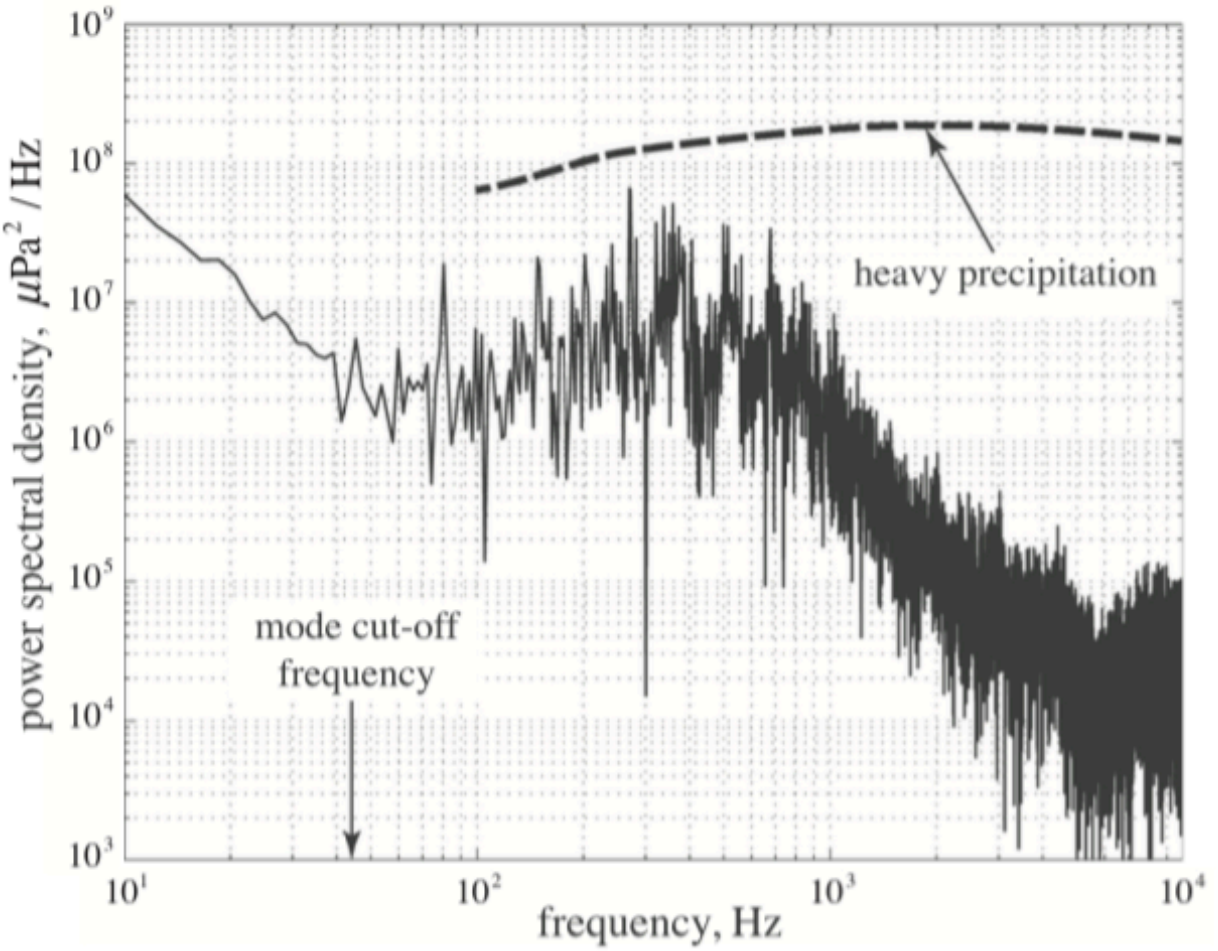

Figure 2.3: Power spectral density of the underwater sound from the R44 helicopter, analysis bandwidth 2.06 Hz averaged over 1.46 s. The first three main rotor harmonics are absent because their frequencies fall below the cut-off frequency of the channel. The spectrum of underwater sound from heavy precipitation is included for comparison.

The shallow-water, 16.5 m, experiment site has a low-frequency modal cut-off of 43 Hz. Due to this cut-off, the first three harmonics, ($13\ Hz, 26\ Hz, and\ 39\ Hz$), of the main rotor are absent in the underwater spectra in Figure 2.3. The higher harmonics of the main rotor do propagate in the channel and are present in the spectra along with the tail rotor fundamental frequency and harmonics. Broadband noise produced by the R44 helicopter is present in the

spectra, but with regard to the overall underwater sound level, it is notable quieter than the underwater noise from heavy precipitation, the latter as reported by Wenz [13].

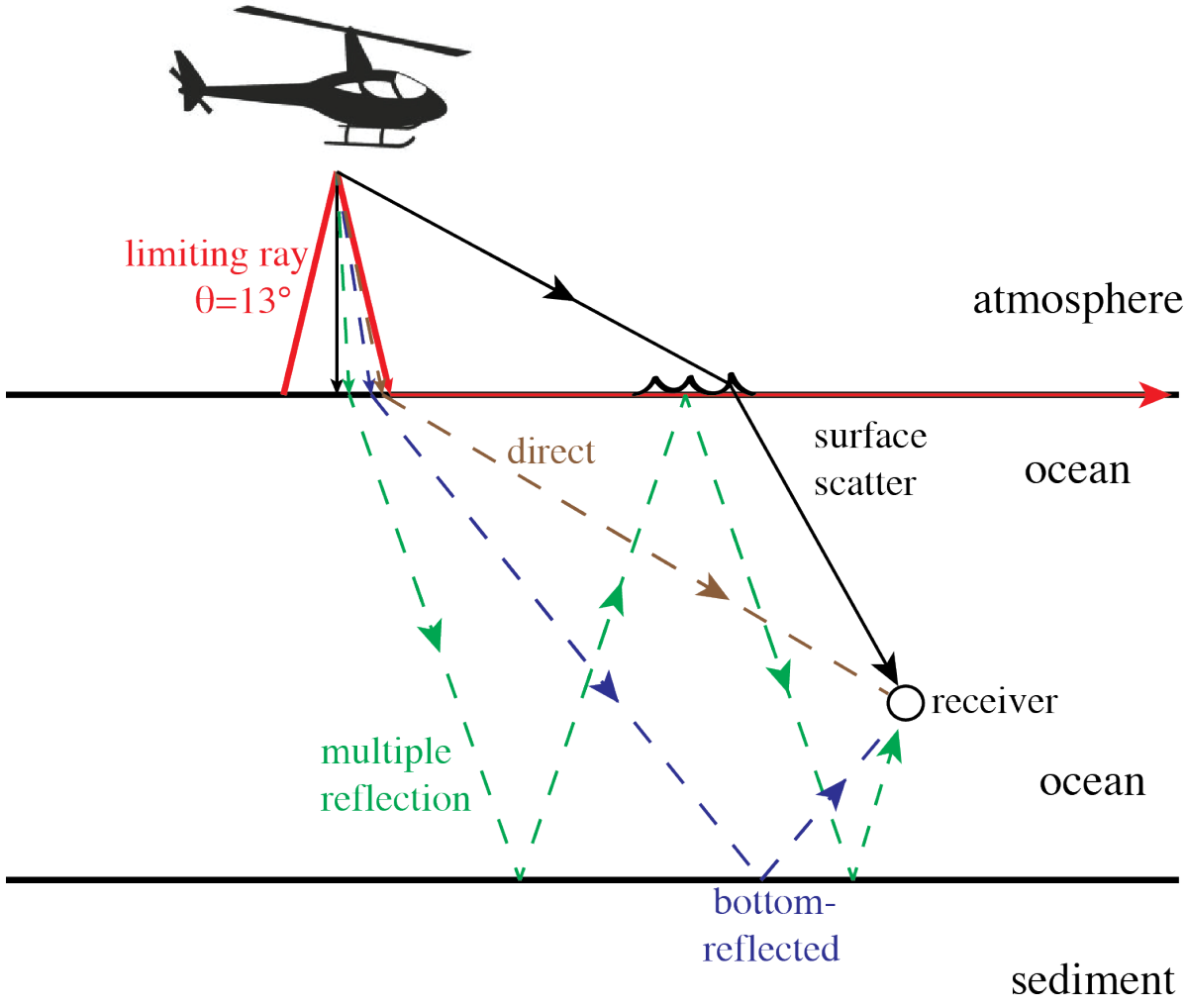

Figure 2.4: Ray schematic of multiple ray paths that produce the propagating normal modes within the underwater waveguide (adapted from *Marine Mammals and Noise* [4]).

Sound traveling from a source in air to a receiver underwater propagates in four ways: (1) via a direct refracted path; (2) via direct refracted paths that are reflected by the bottom; (3) via a "lateral" (surface-traveling) wave; and (4) via scattering from a rough sea surface (Figure 2.4)[14] [4]. These reflections build an acoustic field within the underwater waveguide that consists of the

superposition of the propagating discrete normal modes. While shallow water allows more ray paths for the sound to propagate, modes below the modal cut-off do not propagate. In a Pekeris waveguide the modal cut-off frequency is

$$f_{0m} = \frac{(m-0.5)c_2c_3}{2h\sqrt{c_3^2-c_2^2}}, \qquad m = 1, 2, \ldots \tag{2.3}$$

where h in the water depth, m is the mode number, and c_2 and c_3 is the sound speed in the water and sediment respectively[1]. The underwater acoustic field generated by a helicopter in-flight is not complete without the head wave, otherwise known as a lateral wave[15], which is associated with the seawater-sediment interface.

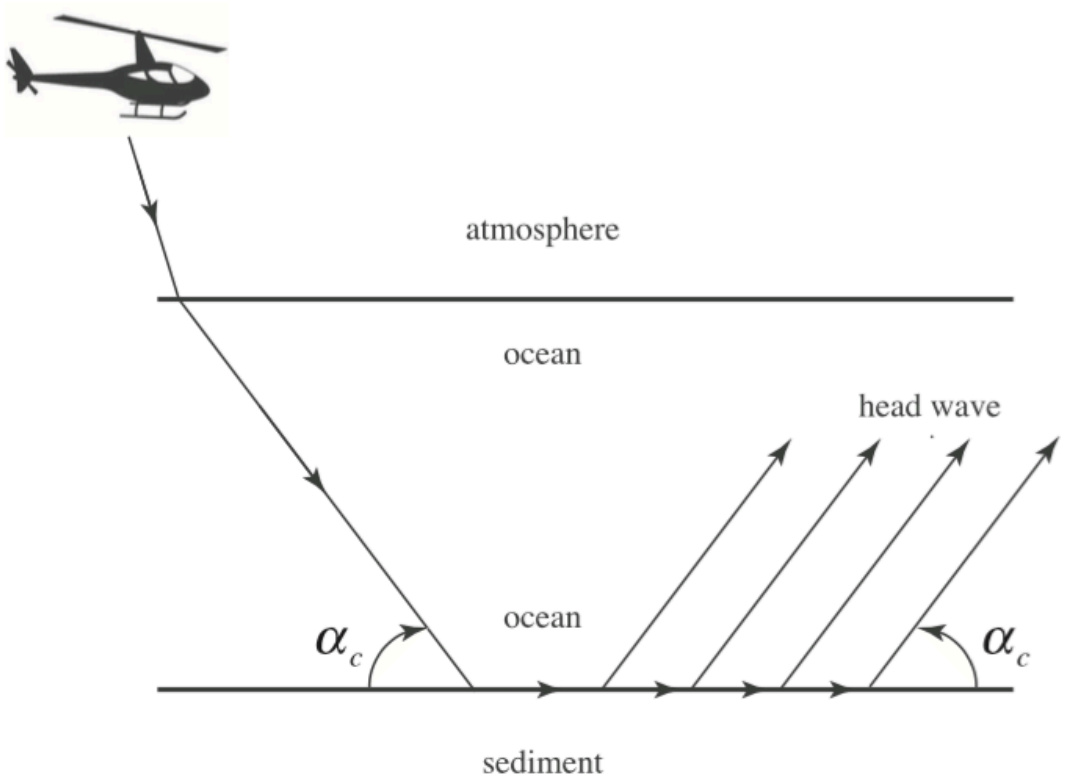

Figure 2.5: Ray schematic of the head wave generated by a hovering helicopter. The ray incident on the seabed at the critical grazing angle, α_c, is refracted at the interface, travels horizontally through the sediment, and, as it progresses, radiates energy back into the water column at the critical grazing angle α_c.

The head wave produced by a hovering helicopter can be described through a straightforward geometrical argument along with Snell's Law (Figure 2.5). A downward-traveling acoustic ray produced by the helicopter is refracted into the water column and is incident on the bottom boundary at the seabed critical angle,

$$\alpha_c = \cos^{-1}\left[\frac{c_2}{c_3}\right]. \tag{2.4}$$

At the sediment interface the ray is refracted along the seabed, propagating horizontally through the sediment. As the ray propagates, it radiates energy back into the water column at the critical angle. This component of the field is what is known as the head wave. Since the head wave propagates within the ocean floor medium at the seawater interface, it propagates at the speed of sound in the seabed. This provides a means of making measurements in the water column to determine the phase speed of the compressional wave in the sediment. To pursue the use of a helicopter as a source for underwater acoustics, a series of experiments was performed. The first experiment involved two flight operations above a sensor station comprised of underwater hydrophones and an in-air microphone, to explore the underwater sound characteristics of a Robinson R44 helicopter. The data collected through the first experiment led to the development of the theory for the head wave produced by an air-borne helicopter, which progressed to a unique, robust inversion method to recover the sound speed in shallow-water marine sediments. The second experiment was designed to test this new theory as well as collect the necessary data to complete the development of the inversion method.

Included in the underwater R44 helicopter signal detected by an underwater hydrophone is the signal corresponding to the head wave, as it radiates back into the water column from the seabed. A horizontal range window exists in which this head wave signal, produced by the R44

helicopter, is detectable at the sensor station. However, if the source is too far away, the signal of the head wave will be too weak, due to its $1/r^2$ geometrical spreading, to be detected over the background of the propagating normal modes. However, the head wave signal will not be received at an underwater receiver if the helicopter range is closer than a minimum range, r_{min} in Figure 2.6. The helicopters altitude along with these two limits dictates the range window in which the head wave can be detected at a receiver within the water column.

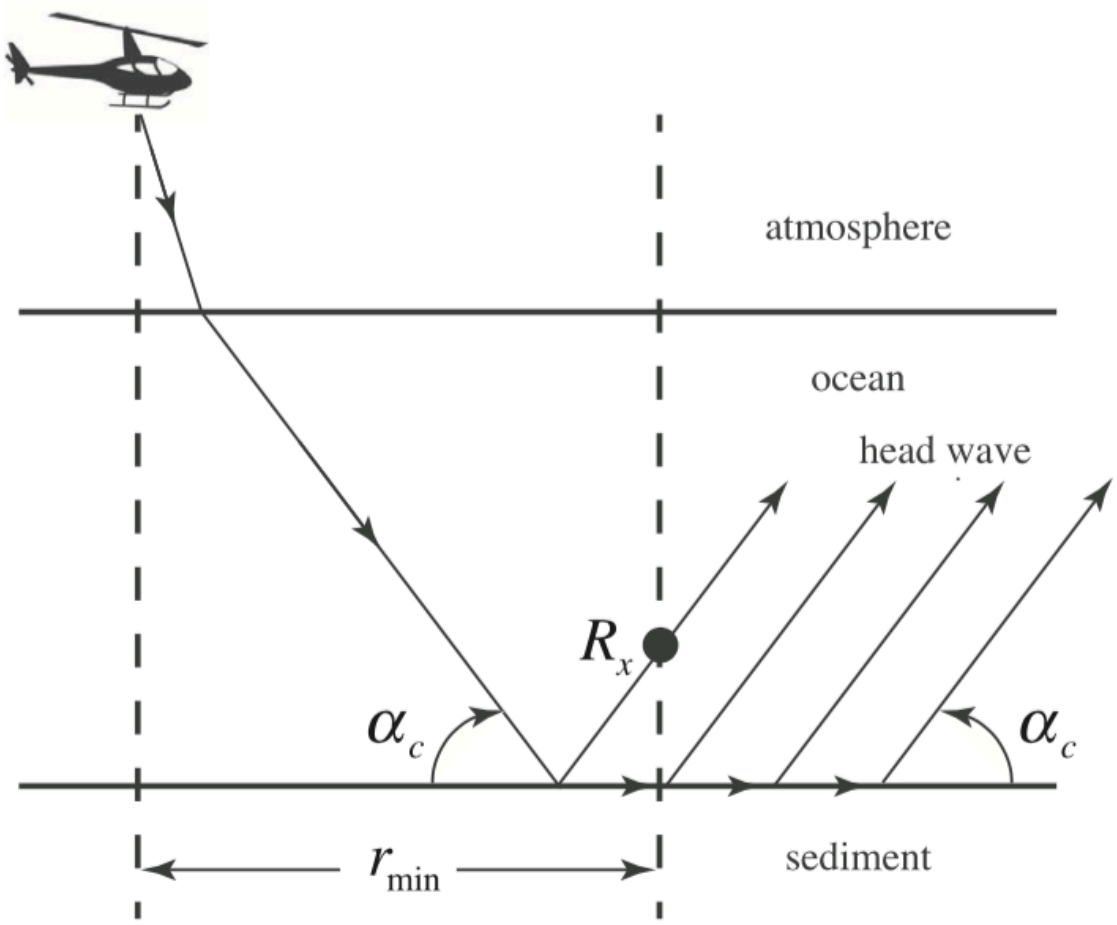

Figure 2.6: Ray geometry illustrating the minimum horizontal range, r_{min}, necessary for the head wave excited by the helicopter to be established at the underwater receiver, R_x.

From the pressure time series recorded on the FlyBy array, the horizontal coherence function was formed between pairs of sensors on the array outside and within this range window. With the R44 helicopter in this range window, the sound speed in the sediment was recovered through the developed inversion process, which is based on the comparison between the data coherence function and theoretical coherence function of the head wave produced by an air-borne source. This produced an estimate of the sediment sound speed of $1682.42 \pm 16.20\ m/s$ at the experiment site. In Chapter 3, the expression for the theoretical coherence function of the head wave is derived, beginning with a three-layer waveguide comprised of atmosphere, ocean, and sediment.

Chapters 2, in part, is a reprint of the material as it appears in the Journal of the Acoustical Society of America: D. A. Bevans, M. J. Buckingham, “Estimating the Sound Speed of a Shallow-water Marine Sediment from the Head Wave Excited by a Low-flying Helicopter”, 142: 2273 (2017). The dissertation author was the primary investigator and author of this manuscript, and Dr. Michael J. Buckingham directed and supervised the research.

References

1. F. B. Jensen, W. A. Kuperman, M. B. Porter, et al., *Computational Ocean Acoustics*. (American Institute of Physics, New York, 1994).

2. *R44 Pilot's Operating Handbook and FAA Approved Rotorcraft Flight Manual*. (Robinson Helicopter Company, Torrance, CA).

3. H. Medwin, R. A. Helbig and J. D. Hagy Jr.,"Spectral characteristics of sound transmission through the rough sea surface", J. Acoust. Soc. Am., **54** (1), 99-109 (1973).

4. W. J. Richardson, C. R. Greene Jr., C. I. Malme, et al., *Marine Mammals and Noise*. (Academic Press, New York, 1995).

5. M. J. Buckingham and E. M. Giddens,"Theory of sound propagation from a moving source in a three-layer Pekeris waveguide", J. Acoust. Soc. Am., **120** (4), 1825-1841 (2006).

6. M. J. Buckingham, E. M. Giddens, J. B. Pompa, et al.,"Sound from a light aircraft for underwater acoustics experiments?", Acta Acustica united with Acustica **88** (5), 752-755 (2002).

7. M. J. Buckingham, E. M. Giddens, F. Simonet, et al.,"Propeller noise from a light aircraft for low-frequency measurements of the speed of sound in a marine sediment", Journal of Computational Acoustics **10** (4), 445-464 (2002).

8. B. G. Ferguson,"A ground-based narrow-band passive acoustic technique for estimating the altitude and speed of a propeller-driven aircraft", J. Acoust. Soc. Am., **92** (3), 1403-1407 (1992).

9. B. G. Ferguson and K. W. Lo,"Transiting aircraft parameter estimation using underwater acoustic sensor data", IEEE J. Ocean. Eng. **24** (4), 424-435 (1999).

10. B. G. Ferguson and G. C. Speechley,"Acoustic detection and localization of a turboprop aircraft by an array of hydrophones towed below the sea surface", IEEE J. Ocean. Eng. **34** (1), 75-82 (2009).

11. H. H. Hubbard, *Aeroacoustics of flight vehicles: Theory and practice. volume 1. noise sources*. (NATIONAL AERONAUTICS AND SPACE ADMIN LANGLEY RESEARCH CENTER HAMPTON VA, 1991).

12. S. C. Lubbard and P. M. Hurdle,"Experimental investigation of acoustic transmission from air into a rough ocean", Journal of the Acoustical Society of America **60** (5), 1048-1052 (1976).

13. G. M. Wenz,"Acoustic ambient noise in the ocean: Spectra and sources", J. Acoust. Soc. Am., **34** (12), 1936-1956 (1962).

14. R. J. Urick,"Noise signature of an aircraft in level flight over a hydrophone in the sea", J. Acoust. Soc. Am., **52** (No. 3, Pt. 2), 993-999 (1972).

15. L. M. Brekhovskikh, *Waves in Layered Media*, second ed. (Academic Press, San Diego, 1980).

Chapter 3

Analytical Solution for the Head Wave in a 3-Layer Atmosphere-Ocean-Sediment Waveguide

3.1 Introduction

In order to analyze the acoustic data from the R44 helicopter experiments a theoretical understanding of the acoustic field is required. In this chapter the analytical solution for the head wave coherence function, within a three-layer waveguide, from an air-borne source (the R44 helicopter in the present case) will be developed. Beginning with three wave equations in a cylindrical coordinate system, one for each layer, the solution for the pressure field within each is presented. The analytical solution for the pressure field in the water column, layer 2, is a complex integral that can be solved numerically. Although, in the complex plane it is possible to separate the integral into its individual components representing different types of waves, including the propagating normal modes and the head wave. The later being the focus of this work. Although this still leaves a complex integral to be evaluated, it is an integral that can be solved through the method of stationary phase. Using these methods the solution for the horizontal coherence function of the head wave within the water column, produced by an air-borne source, will be presented.

3.2 Analytical Solution for the Pressure Field within a Three-Layer Waveguide

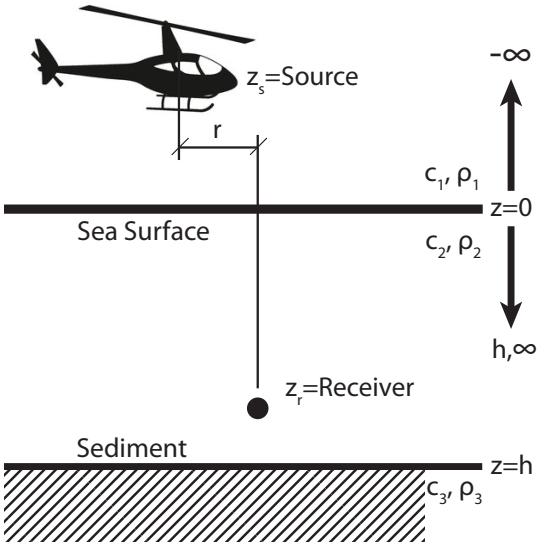

Cylindrical Coordinates
Symmetric about azimuthal coordinate

r = radial coordinate (m)
z = vertical coordinate (m)
t = time coordinate (s)
c = sound speed (m/s)
ρ = density (kg/m^3)
z_s = source altitude (m)
z_f = receiver depth (m)
g = velocity potential (m^2/s)
S = source strength (m^3)

Figure 3.1: Diagram of the setup for the three-layer analytical model being solved with the source directly above the receiver, r=0. Subscripts 1, 2, and 3 are the variable number for each layer, which represents air, ocean, and sediment.

Starting with the cylindrical coordinates wave equation with source in air, $r = 0$:

$$\frac{1}{r}\frac{\partial}{\partial r}\left\{r\frac{\partial g_1}{\partial r}\right\} + \frac{\partial^2 g_1}{\partial z^2} - \frac{1}{c_1^2}\frac{\partial^2 g_1}{\partial t^2} = S\frac{1}{\pi r}\delta(r)\delta(t)\delta(z - z_s), \quad z < 0 \tag{3.1a}$$

$$\frac{1}{r}\frac{\partial}{\partial r}\left\{r\frac{\partial g_2}{\partial r}\right\} + \frac{\partial^2 g_2}{\partial z^2} - \frac{1}{c_2^2}\frac{\partial^2 g_2}{\partial t^2} = 0, \quad 0 \le z \le h \tag{3.1b}$$

$$\frac{1}{r}\frac{\partial}{\partial r}\left\{r\frac{\partial g_3}{\partial r}\right\} + \frac{\partial^2 g_3}{\partial z^2} - \frac{1}{c_3^2}\frac{\partial^2 g_3}{\partial t^2} = 0, \quad z < h \tag{3.1c}$$

Reducing these wave equations by transform method first through a Fourier transform with respect to time, t, converts them into Helmholtz equations,

$$\frac{1}{r}\frac{\partial}{\partial r}\left\{r\frac{\partial G_1}{\partial r}\right\} + \frac{\partial^2 G_1}{\partial z^2} + k_1^2 G_1 = S\frac{1}{\pi r}\delta(r)\,\delta(z - z_s), \quad z < 0 \tag{3.2a}$$

$$\frac{1}{r}\frac{\partial}{\partial r}\left\{r\frac{\partial G_2}{\partial r}\right\}+\frac{\partial^2 G_2}{\partial z^2}+k_2^2 G_2=0,\quad 0\le z\le h \tag{3.2b}$$

$$\frac{1}{r}\frac{\partial}{\partial r}\left\{r\frac{\partial G_3}{\partial r}\right\}+\frac{\partial^2 G_3}{\partial z^2}+k_3^2 G_3=0,\quad z>h \tag{3.2c}$$

where k is the acoustic wavenumber in each layer, denoted by j, defined by Equation 3.3 in which ω is the angular frequency.

$$k_j=\frac{\omega}{c_j} \tag{3.3}$$

The Fourier transform of the velocity potential, $G_j=G_j(r,z;\omega)$, is given by

$$G_j=\int_{-\infty}^{\infty} g_j exp(-i\omega t)dt \tag{3.4a}$$

the inverse of which is

$$g_j=\frac{1}{2\pi}\int_{-\infty}^{\infty} G_j exp(i\omega t)d\omega \tag{3.4b}$$

The Helmoholtz equations can be reduced through the application of the Hankel transform with respect to the range variable, r,

$$G_{jp}=\int_0^{\infty} rG_j J_0(pr)dr \tag{3.5a}$$

the inverse of which is

$$G_j=\int_0^{\infty} pG_{jp}J_0(pr)dp \tag{3.5b}$$

where $J_0(pr)$ is the Bessel function of the first kind and the order zero. The transform variable, p, is used as a subscript to prevent confusion as multiple transforms are being utilized. With the application of the Hankel transformation the Helmholtz equations become

$$\frac{\partial^2 G_{1p}}{\partial z^2}+(k_1^2-p^2)G_{1p}=S\frac{1}{\pi}\,\delta(z-z_s),\quad z<0 \tag{3.6a}$$

$$\frac{\partial^2 G_{2p}}{\partial z^2}+(k_2^2-p^2)G_{2p}=0,\quad 0\le z\le h \tag{3.6b}$$

$$\frac{\partial^2 G_{2p}}{\partial z^2}+(k_3^2-p^2)G_{2p}=0,\quad z>h \tag{3.6c}$$

which can be solved with the boundary conditions, the continuity of pressure,

$$\rho_1 G(0)_{1p} = \rho_2 G(0)_{2p} \tag{3.7a}$$

$$\rho_2 G(h)_{2p} = \rho_3 G(h)_{3p}, \tag{3.7b}$$

and the continuity of the normal component of velocity potential at the air-ocean and ocean-sediment interface,

$$G(h)'_{1p} = G(h)'_{2p} \tag{3.8a}$$

$$G(h)'_{2p} = G(h)'_{3p} \tag{3.8b}$$

where the prime denotes the derivative with respect to z. Before applying the boundary conditions, the equations of 3.6 needs to be reduced to a form of variables and unknown constants. The ordinary differential, homogeneous Equations 3.6b & 3.6c have commonly known solutions with constants of the form

$$G_{2p}(z) = Ae^{-i\eta_2 z} + Be^{i\eta_2 z}, \quad 0 \le z \le h \tag{3.9a}$$

$$G_{3p}(z) = Ce^{-i\eta_3 (z-h)}, \quad z > h \tag{3.9b}$$

where

$$\eta_j = \sqrt{k_j^2 - p^2}, \quad \Im(\eta_2) < 0 \tag{3.10}$$

and A, B, and C are constants of integration and will be determined by the boundary conditions. The convention of the imaginary part of the radical to be negative has been chosen and will be maintained throughout the analysis, ensuring the decay of the wave as depth, z, goes to infinity.

Continuing with Equation 3.6a, the atmosphere layer, it is reduced a third time through a Fourier transform, with a transform variable of v, with respect to z gives

$$\int_{-\infty}^{0} \frac{\partial^2 G_{p1}}{\partial z^2} e^{-ivz} dz + \eta_1 G_{1pv} = S \frac{1}{\pi} e^{-ivz_s}. \tag{3.11}$$

The double derivative with respect to z is solved through the common method of integration by parts gives a solution of

$$\int_{-\infty}^{0} \frac{\partial^2 G_{1p}}{\partial z^2} e^{-ivz} dz = G'_{1p} e^{-ivz}|_{-\infty}^{0} + iv \int_{-\infty}^{0} G'_{1p}\, e^{-ivz} dz = G(0)'_{1p} + ivG(0)_{1p} + v^2 \phi_{1pv}. \quad (3.12)$$

Substituting this back into Equation 3.11 gives

$$G_{1pv}(z) = \frac{S}{\pi} e^{-ivz_s} \frac{1}{(v^2 - \eta_1^2)} + G(0)'_{1p} \frac{1}{v^2 - \eta_1^2} + ivG(0)_{1p} \frac{1}{v^2 - \eta_1^2}, \quad (3.13)$$

which is now in a form that can be inverse Fourier transformed over the limits of $(0, \infty)$ with respect to v giving

$$G_{1p}(z) = \frac{1}{2} \left\{ \frac{iS}{\pi \eta_1} e^{-i\eta_1 |z - z_s|} - \frac{i}{\eta_1} G(0)'_{1p} e^{-i\eta_1 |z|} + G(0)_{1p} e^{-i\eta_1 |z|} \right\}. \quad (3.14)$$

The terms $G(0)_{1p}$ and $G(0)'_{1p}$, which are constants of integration from the Fourier transform of the second derivative shown in Equation 3.12, can be determined through evaluating the boundary conditions, given in Equation 3.7, at $z = 0$.

$$G_{1p}(0) = b_{21}[A + B] \quad (3.15a)$$

$$G_{1p}{}'(0) = -i\eta_2 [A - B] \quad (3.15b)$$

where

$$b_{jl} = \frac{\rho_j}{\rho_l} \quad (3.16)$$

is the density ratio between layers j and layer l.

The constants $A, B, and\ C$ can now be solved through the boundary equations at $z = 0$ and $z = h$, given by equations 3.7 and 3.8.

$$A = \frac{1}{2} C e^{-ih(\eta_3 - \eta_2)} \left[b_{32} + \frac{\eta_3}{\eta_2} \right] \quad (3.17a)$$

$$B = \frac{1}{2} C e^{-ih(\eta_3 + \eta_2)} \left[b_{32} - \frac{\eta_3}{\eta_2} \right] \quad (3.17b)$$

$$C = \frac{S e^{-i\eta_1 |z_s|} e^{i\eta_3 h}}{\pi \left[(\eta_2^2 + b_{21} b_{23} \eta_1 \eta_3) \sin(\eta_2 h) - i\eta_2 (b_{21} \eta_1 + b_{23} \eta_3) \cos(\eta_2 h) \right]} \quad (3.17c)$$

With the known constants the Equations 3.9 the transformed fields in the air, water, and sediment can now be expressed as,

$$G_{1p}(z) = \frac{1}{2}\left\{\frac{iS}{\pi\eta_1}e^{-i\eta_1|z-z_s|} - \frac{\eta_2}{\eta_1}(A-B)e^{-i\eta_1|z|} + b_{21}(A+B)e^{-i\eta_1|z|}\right\} \quad (3.18a)$$

$$G_{2p}(z) = \frac{Se^{-i\eta_1|z_s|}}{\pi}\left\{\frac{\eta_2\cos[\eta_2(h-z)] + i\,b_{23}\eta_3\sin[\eta_2(h-z)]}{(\eta_2^2 + b_{21}b_{23}\eta_1\eta_3)\sin(\eta_2 h) - i\eta_2(b_{21}\eta_1 + b_{23}\eta_3)\cos(\eta_2 h)}\right\} \quad (3.18b)$$

$$G_{3p}(z) = \frac{Se^{-i\eta_1|z_s|}}{\pi}\left\{\frac{e^{i\eta_3(h-z)}}{(\eta_2^2 + b_{21}b_{23}\eta_1\eta_3)\sin(\eta_2 h) - i\eta_2(b_{21}\eta_1 + b_{23}\eta_3)\cos(\eta_2 h)}\right\}. \quad (3.18c)$$

The frequency-dependent field in each layer is obtained through the application of the inverse Hankel transform, expressed in Equation 3.5b, to both sides of the equations of 3.18.

$$G_1(r,z;\omega) = \frac{iS}{2\pi}\int_0^\infty pJ_0(pr)\left\{\frac{1}{\eta_1}e^{-i\eta_1|z-z_s|} - \frac{\eta_2}{\eta_1}(A-B)e^{-i\eta_1|z|} + b_{21}(A+B)e^{-i\eta_1|z|}\right\}dp \quad (3.19a)$$

$$G_2(r,z;\omega) = \frac{S}{\pi}\int_0^\infty pJ_0(pr)e^{-i\eta_1|z_s|}\left\{\frac{\eta_2\cos[\eta_2(h-z)] + i\,b_{23}\eta_3\sin[\eta_2(h-z)]}{(\eta_2^2 + b_{21}b_{23}\eta_1\eta_3)\sin(\eta_2 h) - i\eta_2(b_{21}\eta_1 + b_{23}\eta_3)\cos(\eta_2 h)}\right\}dp \quad (3.19b)$$

$$G_3(r,z;\omega) = \frac{S}{\pi}\int_0^\infty pJ_0(pr)e^{-i\eta_1|z_s|}\left\{\frac{e^{i\eta_3(h-z)}}{(\eta_2^2 + b_{21}b_{23}\eta_1\eta_3)\sin(\eta_2 h) - i\eta_2(b_{21}\eta_1 + b_{23}\eta_3)\cos(\eta_2 h)}\right\}dp. \quad (3.19c)$$

The equations of 3.19 cannot be solved explicitly, and the remainder of the chapter will cover the development, starting with Equation 3.19b, for an explicit solution for the head wave within the water column. Numerical solutions for the equations of 3.19 can be calculated through various numerical methods, one of which is the Simpson method of numerical integration. The transmission loss for the analytical three layer waveguide is calculated, shown in Figure 3.2, for an arbitrary source level, $S = 1\ m^3$, and source altitude of $z_s = -9\ m$.

For comparison with the equations of 3.19 (analytical model solutions) an equivalent computer model SCOOTER was used to calculate the 3-layer pressure field, and is shown in Figure 3.3. SCOOTER is a fast field program (FFP), based on a wavenumber integral, that computes the (complex) acoustic pressure field in a horizontally stratified, multi-layer

waveguide. This computer model will also be used for comparison with the horizontal coherence function of collected data from the head wave experiment detailed in Chapter 5.

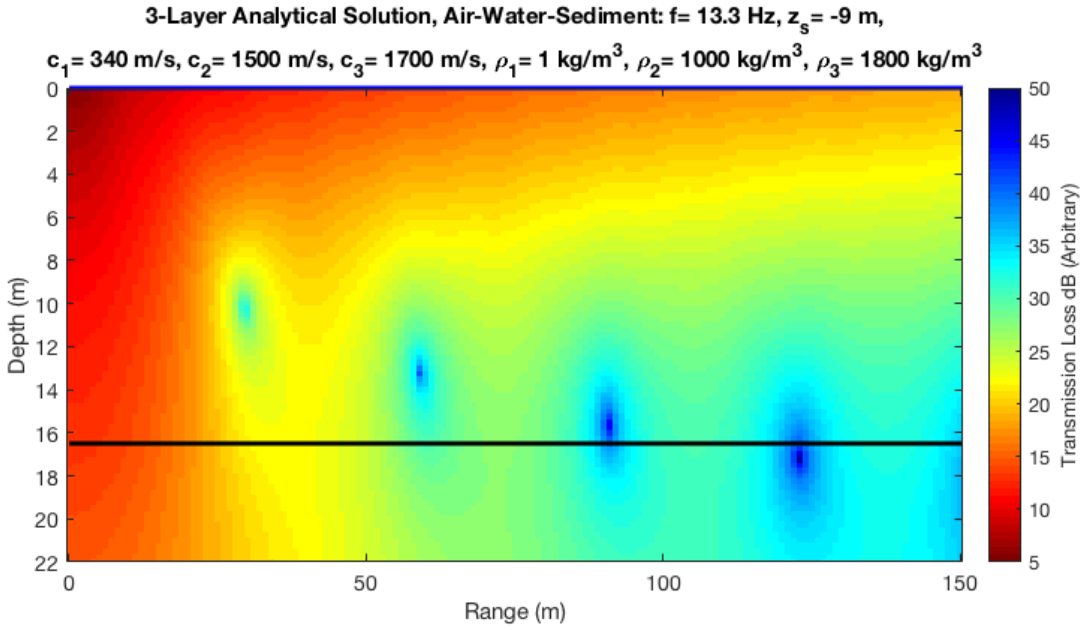

Figure 3.2: Analytical Solution from the three equations of 3.19 with the given variable values presented as a complete three-layer system. The dB levels are arbitrary for the source level, *S*.

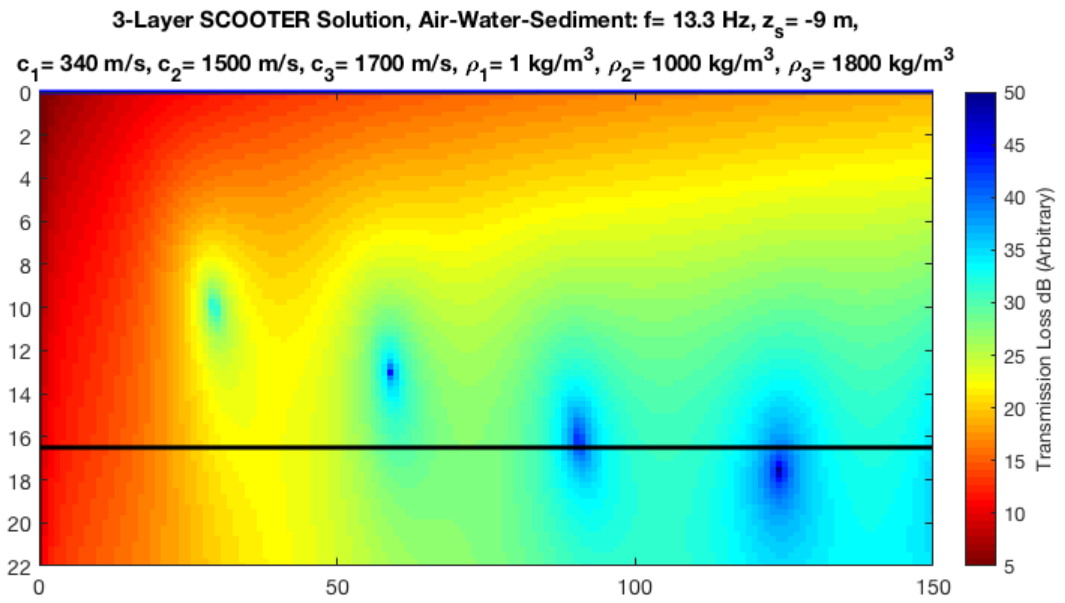

Figure 3.3: Transmission loss plot produced using the FTP model SCOOTER for comparison to the analytical solution presented by the three equations of 3.19. The same values are used for the variable of the three-layer system.

3.3 Contour Integration in the Complex p-plane

The Bessel function in the integrand of Equation 3.19b can be expressed as a sum of the first kind and second kind of Hankel functions[1],

$$J_0(pr) = \frac{1}{2}\left[H_0^{(1)}(pr) + H_0^{(2)}(pr)\right], \tag{3.20}$$

producing,

$$G_2(r,z;\omega) =$$

$$\frac{S}{2\pi}\int_0^\infty p e^{-i\eta_1|z_s|}\left[H_0^{(1)}(pr) + H_0^{(2)}(pr)\right]\left\{\frac{\eta_2\cos[\eta_2(h-z)] + i\,b_{23}\eta_3\sin[\eta_2(h-z)]}{(\eta_2^2+b_{21}b_{23}\eta_1\eta_3)\sin(\eta_2 h) - i\eta_2(b_{21}\eta_1+b_{23}\eta_3)\cos(\eta_2 h)}\right\}dp. \tag{3.21}$$

Using contour integration in the complex p-plane, the integral in Equation 3.21 can be written as a sum of normal modes plus three branch line integrals. One of these branch line integrals, associated with the branch point where $p = k_3$, represents the head wave.

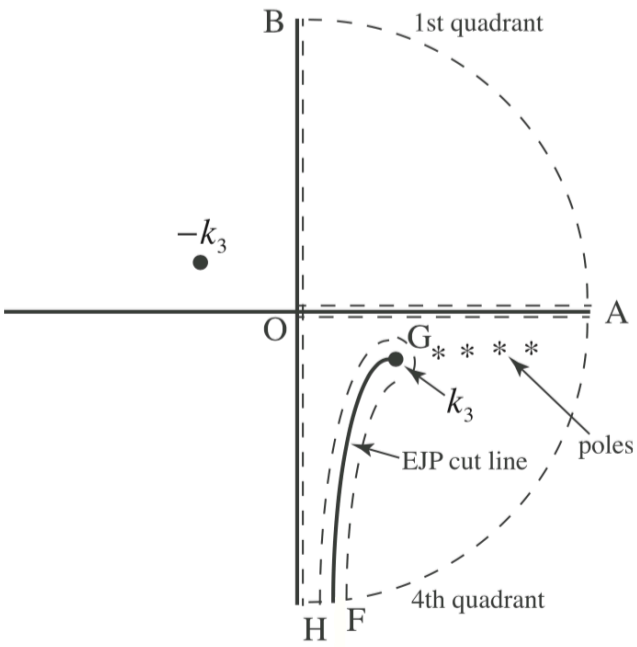

Figure 3.4: Integration contours, depicted by dashed lines, around the first and fourth quadrants of the complex p-plane. No singularities are present in the first quadrant. In the fourth quadrant, in addition to the poles giving rise to the normal modes, the branch point at $p = k_3$ is shown, along with the associated EJP cut line. The integral around the EJP branch cut returns the head wave.

The normal modes can be derived from the zeros in the denominator of Equation 3.21 which correspond to the poles in the 4th quadrant of the complex p-plane, shown in Figure 3.4. These zeros can be obtained through the transcendental characteristic equation,

$$\tan(\eta_2 h) = i\frac{\eta_2(b_{23}\eta_3 + b_{21}\eta_1)}{\eta_2^2 + b_{21}b_{23}\eta_1\eta_3}, \tag{3.22}$$

originally derived in connection to previous work with fixed wing aircraft used as a moving source in a three-layer waveguide.[2] This equation can be reduced to the Pekeris transcendental characteristic equation[3], Equation 3.23, for a two-layer waveguide by taking the density of the air layer to zero the ratio of the density of water to air goes to infinity, $b_{21} = \rho_2/\rho_1 \to \infty$.

$$\tan(\eta_2 h) = i\frac{\eta_2}{b_{23}\eta_3}. \tag{3.23}$$

As the density of the atmosphere goes to zero it becomes a vacuum creating a pressure release surface at the water-air boundary, reducing the system of equations of three to two for a fluid-fluid waveguide consisting of the water and sediment.

The three branch cuts, one for each layer, within the complex p-plane are associated with the radical η_j, where $j = 1, 2, or\ 3$ for a given layer. Defined by Equation 3.10, each η_j has a branch point around its associated wavenumber, $p = \pm k_j$. Also defined in Equation 3.10, is that the imaginary parts of η_j are negative, restricting the branch points to the second and fourth quadrants. The contour integral around the branch cut associated with η_1 is non-zero and associated with the surface-boundary wave and although a head wave, is evanescent within the water column. In addition, the contour integral around the branch cut associated with η_2 can be readily shown to be equal to zero. Leaving the third contour integral around the branch cut associated with η_3, which is non-zero and represents the bottom-boundary wave. This bottom-boundary wave is the propagating head wave within the water column and is the focus of the continued analysis.

3.4 The Branch Line Integral for the Head Wave

The next step in obtaining an expression for the bottom-boundary head wave is to construct a branch cut associated with the radical η_3. This branch cut is in the fourth quadrant of the complex p-plane and must satisfy the requirement in equation 3.10 that the imaginary part of η_3 be less than zero. In order to satisfy this condition the branch cut is taken at η_3 such that $Im(\eta_3) = 0$, this cut, shown in figure 3.4, is known as a EJP cut named after Ewing *et al.*[4] and was introduced during their work on elastic wave propagation in layered media.

Before focusing on the branch cut in quadrant four of the complex p-plane, the first quadrant can readily be shown to have no singularities. By this and through Cauchy's Integral theorem and Jordan's lemma the Hankel function of the first kind in equation 3.21 contribution to the line integral over the real positive axis is equal to the identical line integral along the positive imaginary axis. A similar analysis of the Hankel function of the second kind from equation 3.21 can be performed in the fourth quadrant. One contribution is the integral along the negative imaginary axis, which can be readily demonstrated, to be equal and opposite the integral alone the positive imaginary axis, canceling out one another. The other contributions from the Hankel function of the second kind (Equation 3.21), do not cancel out and are the only non-zero solution from the line integral. These are exclusively in the fourth quadrant and are the residues of the integrand at the poles, which represent the normal modes of the wave-guide, and the branch line integrals around the EJP cuts, which represents the head waves at the surface and sediment boundaries. As stated before, the surface-boundary head wave is evanescent in the water column, which leaves only the EJP cut associated with the bottom-boundary. This EJP branch cut gives rise to the propagating head wave in the water column.

The EJP branch line integral of the bottom-boundary head wave can now be written as

$$I = \oint_{EJP} pH_0^{(2)}(pr)F(\eta_1, \eta_2, \eta_3)dp \tag{3.24}$$

where

$$F(\eta_1, \eta_2, \eta_3) = e^{-i\eta_1|z_s|}\left\{\frac{\eta_2 \cos[\eta_2(h-z)] + i\, b_{23}\eta_3 \sin[\eta_2(h-z)]}{(\eta_2^2 + b_{21}b_{23}\eta_1\eta_3)\sin(\eta_2 h) - i\eta_2(b_{21}\eta_1 + b_{23}\eta_3)\cos(\eta_2 h)}\right\} \tag{3.25}$$

Through a change of variables, p to η_3, the line integral of Equation 3.24 can be expressed as

$$I = -\int_{-\infty}^{\infty} \eta_3 H_0^{(2)}\left(\sqrt{k_3^2 - \eta_3^2}\, r\right) F(\eta_1, \eta_2, \eta_3)d\eta_3 \tag{3.26}$$

where the infinite limits follow from the fact that, around the EJP branch cut, η_3 is by definition real, taking values in the interval $(-\infty, \infty)$.

Although the integral in Equation 3.26 cannot be expressed explicitly, it can be approximated using a modified version of the method of stationary phase. To begin, the Hankel function in the integrand is replaced by its asymptotic expansion, valid for large argument, taking the form

$$H_0^{(2)}\left(\sqrt{k_3^2-\eta_3^2}r\right) \approx \sqrt{\frac{2}{\pi r}}(k_3^2-\eta_3^2)^{-1/4}e^{-i\left[\sqrt{k_3^2-\eta_3^2}r-\pi/4\right]} \tag{3.27}$$

The function in Equation 3.25 can be expressed in exponential terms,

$$F(\eta_1,\eta_2,\eta_3) = Pe^{i[\eta_2(h-z)-\eta_1|z'|]} + Qe^{-i[\eta_2(h-z)-\eta_1|z'|]}, \tag{3.28}$$

where

$$P = P(\eta_3) = \frac{(\eta_2+b_{23}\eta_3)}{2D}, \tag{3.29}$$

$$Q = Q(\eta_3) = \frac{(\eta_2-b_{23}\eta_3)}{2D}, \tag{3.30}$$

and,

$$D = D(\eta_3) = (\eta_2^2 + b_{21}b_{23}\eta_1\eta_3)\sin(\eta_2 h) - i\eta_2(b_{23}\eta_3 + b_{21}\eta_2)\cos(\eta_2 h). \tag{3.31}$$

At this stage, the bilateral integral in Equation 3.26 is converted to the unilateral form

$$I = -\sqrt{\frac{2}{\pi r}}e^{i(\pi/4)}\int_0^\infty \frac{\eta_2\eta_3^2}{(k_3^2-\eta_3^2)^{1/4}}e^{-i\sqrt{k_3^2-\eta_3^2}r}\times$$

$$\left\{[P(\eta_3)-P(-\eta_3)]e^{i[\eta_2(h-z)-\eta_1|z'|]} + [Q(\eta_3)-Q(-\eta_3)]e^{-i[\eta_2(h-z)-\eta_1|z'|]}\right\}d\eta_3, \tag{3.32a}$$

which reduces to

$$I = -b_{23}\sqrt{\frac{2}{\pi r}}e^{i(3\pi/4)}\int_0^\infty \frac{\eta_2\eta_3^2}{(k_3^2-\eta_3^2)^{1/4}D(\eta_3)D(-\eta_3)}\times$$

$$\left\{(\eta_2 - b_{21}\eta_1)e^{-i\left[\sqrt{k_3^2-\eta_3^2}r+\eta_2 z+\eta_1|z'|\right]} + (\eta_2 + b_{21}\eta_1)e^{-i\left[\sqrt{k_3^2-\eta_3^2}r-\eta_2 z+\eta_1|z'|\right]}\right\}d\eta_3. \quad (3.32b)$$

This expression contains two integrals that differ only by two sign changes given by,

$$Int_{\pm} = \int_0^{\infty} \frac{\eta_2\eta_3^2}{(k_3^2-\eta_3^2)^{1/4}D(\eta_3)D(-\eta_3)}(\eta_2 \pm b_{21}\eta_1)e^{-i\left[\sqrt{k_3^2-\eta_3^2}r\pm\eta_2 z+\eta_1|z'|\right]}d\eta_3. \quad (3.33)$$

3.6 Stationary Phase

The integrals in Equation 3.33 are of a form that is suitable for evaluation by the method of stationary phase, given by

$$\mathfrak{M} = \int_0^{\infty} h(x)e^{-iK\varphi(x)}dx. \quad (3.34)$$

The integration variable x is dimensionless and the integral $\mathfrak{M}$ is to be evaluated as the coefficient in the exponential, K, goes to infinity, causing the exponential of the integral to become a rapidly varying function of x. The major contribution to the integral comes from the vicinity of when x equals the stationary point. The phase function, $\varphi(x)$, for the integrals in Equation 3.33 originates from the argument of the exponentials,

$$\varphi_{\pm}(\eta_3) = \left[\sqrt{k_3^2-\eta_3^2}r \pm \eta_2 z + \eta_1|z'|\right]. \quad (3.35)$$

The stationary point, also known as the turning point, can be determined from Equation 3.35, beginning with rewriting the variables η_1 and η_2 from the relationship given in Equation 3.10

$$\varphi_{\pm}(\eta_3) = \left[\sqrt{k_3^2-\eta_3^2}r \pm \sqrt{k_2^2-p^2}z + \sqrt{k_1^2-p^2}|z'|\right], \quad (3.36)$$

and pulling out k_3 from the terms of the functions,

$$\varphi_{\pm}(\eta_3) = k_3\left[\sqrt{1-\frac{\eta_3^2}{k_3^2}}r \pm \sqrt{\frac{\eta_3^2}{k_3^2}+\frac{k_2^2}{k_3^2}-1}z + \sqrt{\frac{\eta_3^2}{k_3^2}+\frac{k_1^2}{k_3^2}-1}|z'|\right]. \quad (3.37)$$

Using the relationship between the wavenumber and sound speed,

$$\frac{k_i}{k_j} = \frac{c_j}{c_i}, \tag{3.38}$$

within the layers of the atmosphere-ocean-sediment model and substituting in

$$\frac{k_1^2}{k_3^2} - 1 = \frac{1}{cos^2(\beta_c)} - 1 = \frac{1-cos^2(\beta_c)}{cos^2(\beta_c)} = \frac{sin^2(\beta_c)}{cos^2(\beta_c)} = tan^2(\beta_c) \tag{3.39a}$$

and

$$\frac{k_2^2}{k_3^2} - 1 = \frac{1}{cos^2(\alpha_c)} - 1 = \frac{1-cos^2(\alpha_c)}{cos^2(\alpha_c)} = \frac{sin^2(\alpha_c)}{cos^2(\alpha_c)} = tan^2(\alpha_c), \tag{3.39b}$$

where

$$\alpha_c = \cos^{-1}\left(\frac{c_2}{c_3}\right) \quad and \quad \beta_c = \cos^{-1}\left(\frac{c_1}{c_3}\right), \tag{3.39c}$$

results in the final form of

$$\varphi_{\pm}(\eta_3) = k_3\left[\sqrt{1-\frac{\eta_3^2}{k_3^2}}r \pm \sqrt{\frac{\eta_3^2}{k_3^2} + tan^2\alpha_c}z + \sqrt{\frac{\eta_3^2}{k_3^2} + tan^2\beta_c}|z'|\right]. \tag{3.40}$$

The function $\varphi_{\pm}(\eta_3)$ is now in a form where we can define x as

$$x = \frac{\eta_3}{k_3}, \tag{3.41}$$

resulting in the phase function for the method of stationary phase,

$$\varphi_{\pm}(x) = k_3\left[\sqrt{1-x^2}r \pm \sqrt{x^2 + tan^2\alpha_c}z + \sqrt{x^2 + tan^2\beta_c}|z'|\right]. \tag{3.42}$$

Differentiating Equation 3.42 with respect to x, and setting the result equal to zero,

$$\varphi'_{\pm}(x) = 0 = xk_3\left[(1-x^2)^{-1/2}r \pm (x^2 + tan^2\alpha_c)^{-1/2}z + (x^2 + tan^2\beta_c)^{-1/2}|z'|\right], \tag{3.43}$$

readily shows the stationary point to be $x = 0$. Now that x has been defined we can define $d\eta_3$ from Equation 3.33 in terms of the integration variable x as

$$d\eta_3 = k_3 dx. \tag{3.44}$$

The variable k_3 in this expression can be placed outside the integrals in future expressions of equation *I*, Equation 3.32b.

The function $h(x)$, in Equation 3.34, by comparison is a slowly varying function and is determined from the non-exponential terms in Equation 3.33 by the same process as $\varphi_{\pm}(x)$ resulting in

$$h_{\pm}(x) = x^2 \frac{k_3^3\sqrt{x^2+tan^2\alpha_c}}{\left(k_3^2[1-x^2]\right)^{1/4} D_+(x)D_-(x)} \left(k_3\sqrt{x^2+tan^2\alpha_c} \pm b_{21}k_3\sqrt{x^2+tan^2\beta_c}\right), \tag{3.45}$$

where $D_{\pm}(x)$ is given by

$$D_{\pm}(x) = k_3^2 \left(x^2 + tan^2\alpha_c \pm xb_{21}b_{23}\sqrt{x^2+tan^2\beta_c}\right) \sin\left(k_3\sqrt{x^2+tan^2\alpha_c}h\right) -$$

$$ik_3^2\sqrt{x^2+tan^2\alpha_c}\left(b_{21}\sqrt{x^2+tan^2\beta_c} \pm xb_{23}\right) \cos\left(k_3\sqrt{x^2+tan^2\alpha_c}h\right). \tag{3.46}$$

The x^2 term in Equation 3.45 comes from the η_3^2 term in Equation 3.33 by the relation

$$\eta_3^2 = \frac{\eta_3^2}{k_3^2}k_3^2 = x^2k_3^2. \tag{3.47}$$

Equation 3.45 can be rewritten as

$$h_{\pm}(x) = x^2 f_{\pm}(x), \tag{3.48}$$

where

$$f_{\pm}(x) = \frac{k_3^3\sqrt{x^2+tan^2\alpha_c}}{\left(k_3^2[1-x^2]\right)^{1/4} D_+(x)D_-(x)} \left(k_3\sqrt{x^2+tan^2\alpha_c} \pm b_{21}k_3\sqrt{x^2+tan^2\beta_c}\right). \tag{3.49}$$

If the standard stationary phase technique were applied to the integral in Equation 3.34, the product $h(x) = x^2f(x)$ would be treated as the slowly varying function, whose value at the stationary point is $h(0) = 0$, due to the presence of the factor x^2 in $h(x)$. It follows that, since it scales with $h(0)$, the standard stationary phase expression returns a value of zero for the integral when Equation 3.48 is substituted into Equation 3.34,

$$\mathfrak{M} = \int_0^{\infty} x^2 f(x) e^{-iK\varphi(x)} dx. \tag{3.50}$$

In general the integral is non-zero indicating that a modification to the standard stationary phase technique is required in order to accommodate the presence of the factor x^2 in the integrand of Equation 3.50.

3.6 Modified Stationary Phase

In order to develop a modified version of the stationary phase technic the standard stationary phase procedure is initially followed, whereby the phase function is expressed as a Taylor expansion to second-order in x about the stationary point at $x = 0$:

$$\varphi(x) = \varphi(0) + x\varphi'(0) + \frac{x^2}{2!}\varphi''(0) + \cdots, \tag{3.51}$$

where a prime denotes a derivative with respect to the argument. The two non-zero components of Equation 3.51 are the first term of the expansion and the second derivative. The contribution to the integral $\mathfrak{M}$ from around the stationary point may be approximated as

$$\mathfrak{M} \approx f(0)e^{-iK\varphi(0)} \int_0^{\epsilon} x^2 e^{-i(x^2/2)K\varphi''(x)} dx, \tag{3.52}$$

where ϵ is a positive constant. As shown the function $f(x)$ evaluated at the stationary point, $x = 0$, has moved outside the integral but now, in contrast with the standard stationary phase analysis, the term x^2 remains as a factor in the integrand. By making the substitution

$$y = \frac{x^2}{2} K|\varphi''(0)|, \qquad dy = xK|\varphi''(0)|dx, \tag{3.53}$$

and allowing the parameter K to become indefinitely large, the integral in Equation 3.52 can be expressed as

$$\mathfrak{M} \approx \frac{\sqrt{2}f(0)}{(K|\varphi''(0)|)^{3/2}} e^{-iK\varphi(0)} \int_0^{\infty} y^{1/2} e^{-iy} dy$$

$$= \frac{f(0)}{\sqrt{2}(K|\varphi''(0)|)^{3/2}} e^{-iK\varphi(0)} \times \int_{-\infty}^{\infty} [1 + sgn(y)]|y|^{1/2} e^{-iy} dy, \tag{3.54}$$

where $sgn(y)$ is the signum function, taking a value of -1 for $y < 0$ and $+1$ for $y > 0$.

The second integral in Equation 3.54 is an example of a Fourier transform of a generalized function, actually two generalized functions, $|y|^{1/2}$ and $sgn(y)|y|^{1/2}$.

Table 3.1: Fourier transforms of the generalized function used in the text. (After Lighthill[5], Table I, p. 43.)

	1	$sgn(y)$
$\|y\|^n$	$\{2\cos\pi(\mu+1)/2\}\mu!\,\|x\|^{-\mu-1}$	$\{-2i\sin\pi(\mu+1)/2\}\mu!\,\|x\|^{-\mu-1}sgn(x)$
y^n	$(2\pi i)^n\delta^{(n)}(x)$	$2(n!)(ix)^{-n-1}$
y^{-m}	$-\pi i\frac{(-ix)^{m-1}}{(m-1)!}sgn(y)$	$-2\frac{(-ix)^{m-1}}{(m-1)!}\{\ln\|x\|+C\}$
$y^n\ln\|y\|$	$-\pi i\frac{n!}{(ix)^{n+1}}sgn(y)$	$-2\frac{n!}{(ix)^{n+1}}\{\ln\|x\|-\psi(n)\}$

These Fourier transforms, which may be found in Table I of Lighthill,[5] lead to the final modified stationary phase expression for the integral $\mathfrak{M}$,

$$\mathfrak{M} \approx \sqrt{\frac{\pi}{2}}\frac{f(0)}{(K|\varphi''(0)|)^{3/2}}e^{-iK\varphi(0)}e^{-i(3\pi/4)}. \tag{3.55}$$

With Equation 3.55 we can now solve for the integrals given in Equation 3.33, and as a result also solve for the expression *I* of Equation 3.32b. From Equation 3.42 the phase function at the stationary point, $x = 0$, is

$$\varphi_{\pm}(0) = k_3[r \pm z\tan\alpha_c + |z'|\tan\beta_c], \tag{3.56}$$

from the second derivative we obtain the phase term in the denominator as

$$\varphi''_{\pm}(0) = k_3[r \pm z\cot\alpha_c + |z'|\cot\beta_c], \tag{3.57}$$

and Equation 3.49, at $x = 0$, gives

$$f_{\pm}(0) = \frac{k_3^3 \tan\alpha_c (k_3 \tan\alpha_c \pm b_{21} k_3 \tan\beta_c)}{(k_3^2)^{1/4} D_+(x) D_-(x)} \quad , \tag{3.58}$$

where

$$D_{\pm}(0) = k_3^2 tan^2\alpha_c \sin(k_3 h \tan\alpha_c) - i k_3^2 b_{21} \tan\alpha_c \tan\beta_c \cos(k_3 h \tan\alpha_c). \tag{3.59}$$

With Equations 3.44, 3.55-3.59, Equation 3.32b becomes

$$I = \frac{b_{23} k_3}{\sqrt{r}} e^{-iK k_3 [r + |z'| \tan\beta_c]} \times$$

$$\left[\frac{k_3^3 \tan\alpha_c \, (k_3 \tan\alpha_c + b_{21} k_3 \tan\beta_c) e^{-iK k_3 z \tan\alpha_c}}{(k_3^2)^{1/4} D_+(0) D_-(0) (K|k_3[r + z\cot\alpha_c + |z'|\cot\beta_c]|)^{3/2}} + \right.$$

$$\left. \frac{k_3^3 \tan\alpha_c \, (k_3 \tan\alpha_c - b_{21} k_3 \tan\beta_c) e^{iK k_3 \tan\alpha_c z}}{(k_3^2)^{1/4} D_+(0) D_-(0) (K|k_3[r - z\cot\alpha_c + |z'|\cot\beta_c]|)^{3/2}} \right] . \tag{3.60}$$

With an expression for the modified stationary phase, Equation 3.60, the analysis of the head wave may be resumed.

3.7 The Head Wave

The modified stationary phase expression of Equation 3.60 can be reduced through the identities

$$\tan\beta_c = \frac{k_1}{k_3} \sin\beta_c \qquad \text{and} \qquad \tan\alpha_c = \frac{k_2}{k_3} \sin\alpha_c, \tag{3.61}$$

and evaluated under the condition $K \to \infty$ results in the following expression for the head wave:

$$I = \frac{b_{23} k_3}{\sqrt{r}} e^{[k_3 r + k_1 |z'| \sin(\beta_c)]} \times$$

$$\left\{ \frac{f_+ e^{i[k_2 z \sin\alpha_c]}}{|r - z\cot(\alpha_c) + |z'|\cot(\beta_c)|^{3/2}} + \frac{f_- e^{-i[k_2 z \sin\alpha_c]}}{|r + z\cot(\alpha_c) + |z'|\cot(\beta_c)|^{3/2}} \right\}$$

, (3.62)

where

$$f_{\pm} = \frac{k_2 \sin(\alpha_c)}{L^2}\left[k_2 \sin(\alpha_c) \pm b_{21} k_1 \sin(\beta_c)\right] \quad (3.63)$$

and

$$L = k_2 \sin(\alpha_c)\left\{k_2 \sin(\alpha_c) \sin[k_2 h \sin(\alpha_c)] - i b_{21} k_1 \sin(\beta_c) \cos[k_2 h \sin(\alpha_c)]\right\}. \quad (3.64)$$

Since, under the stationary phase condition, the horizontal range, r, is very much greater than both the hydrophone depth, z, and the source elevation, $|z'|$. Under these conditions the denominators, within the parentheses, of Equation 3.62 can be approximated to $r^{3/2}$, in which case the expression for the head wave reduces to

$$I \approx \frac{b_{23} k_3}{r^2} e^{-i\left[k_3 r + k_1 |z'| \sin(\beta_c)\right]}\left\{f_+ e^{i[k_2 z \sin(\alpha_c)]} + f_- e^{-i[k_2 z \sin(\alpha_c)]}\right\}. \quad (3.65)$$

Equation 3.65 has the classic form of the pressure of a propagating head wave. Since the term in parentheses is independent of r, the *pressure* field decays as $1/r^2$ resulting in the intensity of the head wave to decay as $1/r^4$. Despite this rapid geometrical spreading, the head wave, usually generated by impulsive sources, has found application as the basis of inversion schemes for recovering geophysical parameters in seismology[6] and underwater acoustics[7].

Equation 3.65 is the pressure field, from a source at a given altitude, for a head wave associated with the seabed boundary at a given point in a cylindrical coordinate system for a three-layer, atmosphere, ocean, and seabed, waveguide. With the pressure at given points in the waveguide analytical simulations can be performed for comparison with different physical hydrophones locations in the real world environment. One such analytical solution, which will be the focus of the next section, is the horizontal coherence between to hydrophone locations of the

same depth but at different ranges from the source. The theoretical expression for the horizontal coherence provides a simple inversion procedure for recovering the sound speed in shallow-water environments. As shown in Equation 3.65 the dependence on r is limited to two terms: the spreading term, $1/r^2$, already discussed and the exponential term, $e^{-ik_3 r}$. As the acoustic wavenumber in the sediment, k_3, appears in the term along with the horizontal range, r, this provides a direction to the recovery of the sound speed in the sediment, c_3, through the relationship $k_3 = \omega/c_3$.

3.8 The Head Wave Horizontal Coherence Function

To form the coherence function from the pressure of the head wave, suppose that two sensors are positioned in the water column, horizontally aligned at ranges r_1 and r_2 from the airborne source. The pressure signatures of the head wave at the two receivers is given by,

$$I(r_1) = I(r_1, z, |z'|; \omega) \tag{3.66}$$

and

$$I(r_2) = I(r_2, z, |z'|; \omega) \tag{3.67}$$

respectively. The coherence function of the received signals is, by definition,

$$\Gamma_{12} = \frac{\overline{I(r_1)I^*(r_2)}}{\sqrt{\overline{|I(r_1)|^2}\,\overline{|I(r_2)|^2}}}, \tag{3.68}$$

where the asterisk denotes a complex conjugate and the overbar represents and ensemble average. When Equation 3.64 for the complex pressure of the head wave is substituted into Equation 3.68 the expression simplifies down to the remarkably simple form

$$\Gamma_{12} \approx exp[-ik_3(r_1 - r_2)], \tag{3.69}$$

which is shown for the 3-layer model in Figure 3.5. The range dependent term, $e^{-ik_3 r}$, is all that remains as all the other terms cancel, including attenuation in the sediment if it had been explicitly included in this analysis. If attenuation in the sediment were included, Equation 3.69 would still hold, but with k_3 interpreted as the real part of the complex wavenumber in the sediment. Equation 3.69 is dependent on only two terms: the separation of the two sensors, $\Delta r = (r_1 - r_2)$, and the sound speed in the sediment, $k_3 = \omega / c_3$.

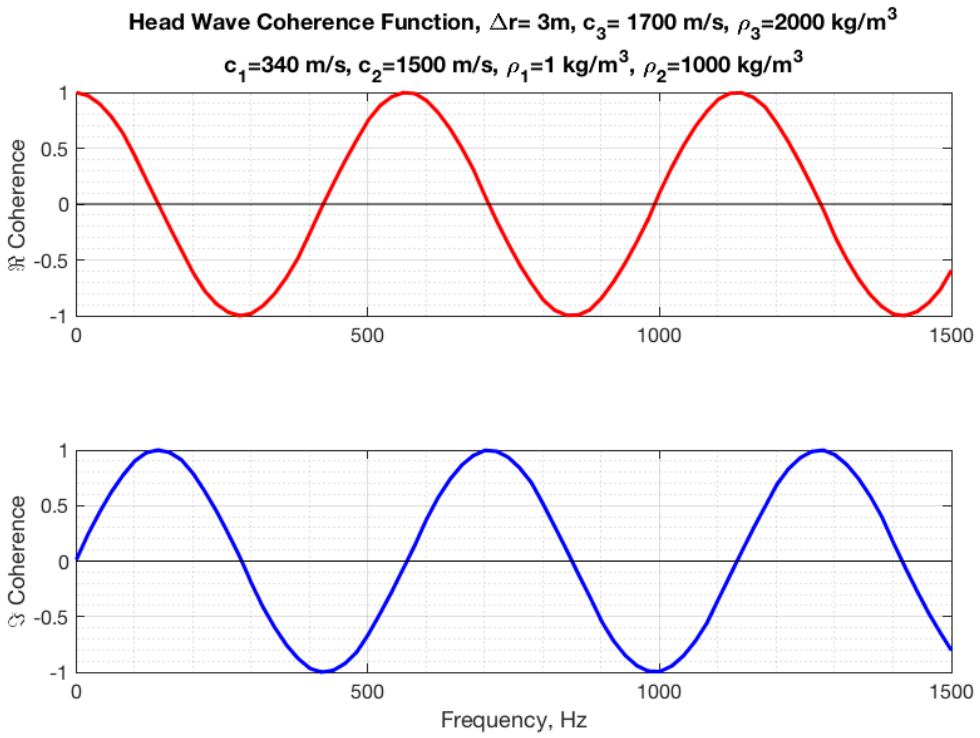

Figure 3.5: The head wave coherence function real and imaginary parts for the three-layer waveguide will the given values for the variables for each layer.

The complex coherence function for the head wave in Equation 3.69 consists of real and imaginary parts, which are cosine and sine functions respectively. This is apparent in Figure 3.5 for a sediment sound speed of 1700 m/s and a fixed sensor separation of 3 m. Both the real and imaginary parts of the coherence function fluctuate between 1 and -1 as frequency increases,

crossing the zero line several times in the displayed bandwidth. These zero crossings are the driving factor in the inversion method developed and presented throughout this work, as they are directly correlated to the sediment sound speed with a known underwater sensor separation. These zero crossings in frequency are related to the sediment sound speed through the equation:

$$c_3 = \frac{4f(n)\Delta r}{n}, \tag{3.70}$$

where n is the nth zero crossing, $f(n)$ is the frequency at that zero crossing, and Δr is the sensor separation. This dependence on sediment sound speed is visualized in Figure 3.6 for four different sediment sound speeds. The zero crossings move to higher values as the sediment sound speed increases.

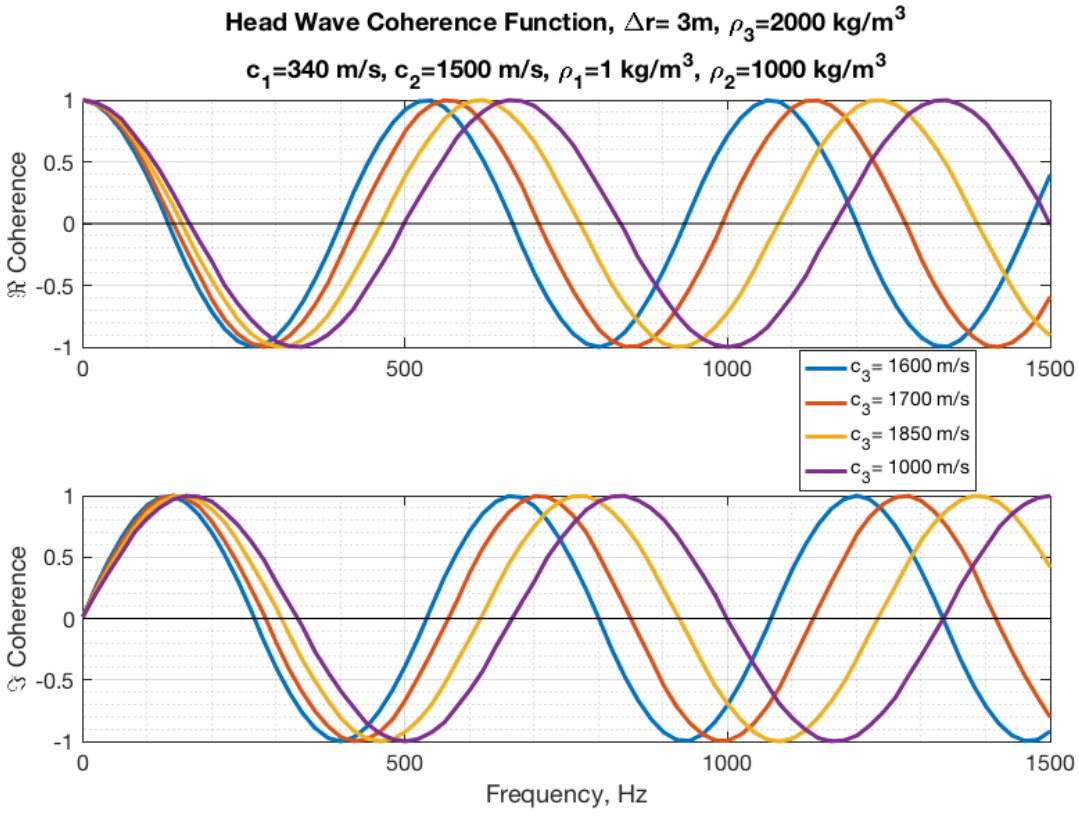

Figure 3.6: Theoretical head wave coherence function for four different sediment sound speeds.

In Equation 3.69, the sediment sound speed at a given frequency, or bandwidth of frequencies, can be determined through the horizontal coherence function for a given sensor separation. The sensor separation also dictates at which frequencies the zero crossing occur. To recover the sediment sound speed at lower frequencies the sensor separation must be increased. For a fixed sediment sound speed of 1700 m/s, within a frequency bandwidth $0 - 500$ hz, two sensor separations of 3 m (red) and 12 m (blue) are shown in Figure 3.7.

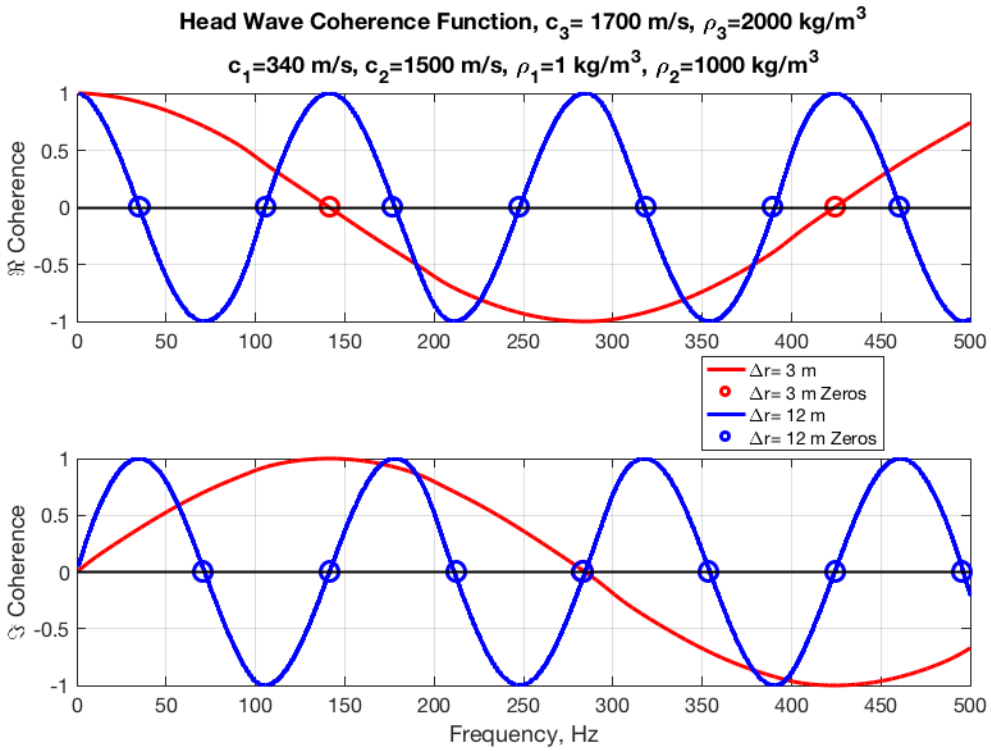

Figure 3.7: The head wave horizontal coherence function at a sediment sound speed of 1700 m/s with a sensor separation of 3 meters (red) and 12 meters (blue).

With the greater sensor separation the density of zero crossings increases. The zero crossings from this analytical solution of the head wave coherence form the bases of the inversion technic presented in Chapter 5.

Chapters 3, in part, is a reprint of the material as it appears in the Journal of the Acoustical Society of America: D. A. Bevans, M. J. Buckingham, “Estimating the Sound Speed of a Shallow-water Marine Sediment from the Head Wave Excited by a Low-flying Helicopter”, 142: 2273 (2017). The dissertation author was the primary investigator and author of this manuscript, and Dr. Michael J. Buckingham directed and supervised the research.

References

1. M. Abramowitz and I. A. Stegun, *Handbook of Mathematical Functions*. (Dover, New York, 1965).

2. M. J. Buckingham and E. M. Giddens,"Theory of sound propagation from a moving source in a three-layer Pekeris waveguide", J. Acoust. Soc. Am., **120** (4), 1825-1841 (2006).

3. C. L. Pekeris, in *Geological Society of America Memoir 27 Propagation of Sound in the Ocean* (Geological Society of America, New York, 1948), Vol. **27**, pp. 1-117.

4. W. M. Ewing, W. S. Jardetzky and F. Press, *Elastic Waves in Layered Media*. (McGraw-Hill, New York, 1957).

5. M. J. S. Lighthill, *Introduction to Fourier Analysis and Generalised Functions*. (Cambridge University Press, Cambridge, 1958).

6. K. Aki and P. G. Richards, *Quantitative Seismology*. (University Science Books, 2002).

7. M. V. Hall,"Measurement of seabed sound speeds from head waves in shallow water", IEEE J. Ocean. Eng. **21** (4), 413-422 (1996).

Chapter 4

Initial Experiment to Investigate the Underwater Sound Field Generated by a Robinson R44 Helicopter

4.1 Introduction

A series of experiments using a Robinson R44 helicopter has been performed off the coast of Southern California, roughly 2 km North of Scripps Pier (32^{o} 53.859' N 117^{o} 15.808' W) at the Scripps Institution of Oceanography. The purpose of the experiments was to investigate the underwater sound field produced by the helicopter and its potential use in underwater acoustics experiments. The experiments was performed in shallow water, 16.5 m depth, using a hydrophone line array, known as the FlyBy array, aligned horizontal 0.5 m above the seabed. In this chapter, the first of the experiments performed on the 6th of April 2015 will be discussed in detail, including the experiment setup, equipment, and data collected by a microphone above the sea surface and hydrophones below.

The Robinson R44 helicopter performed two flight operations over the sensor station. Over-flights on north and south bound headings at cruising speed; and stationary flight (hovers) above the sensors to investigate the effect of altitude on the intensity of the underwater. Using the knowledge and experience gained through this first experiment, an additional helicopter experiment was designed and performed on the 14th of December 2017, with the objective of investigating the head wave produced at various ranges by the R44 Helicopter in hover mode, at end-fire to the FlyBy array. Through this approach, and with the theoretical understanding of the

head wave horizontal coherence function from the previous chapter, these experiments led to a method for recovering the sound speed of the sediment.

4.2 Sensor Station Equipment

On the 6th of April 2015, in order to investigate the underwater properties of an airborne helicopter, an experiment was conducted in shallow water, 16.5 m depth, about 2 km off the coast of southern California, in which the sound from a Robinson R44 Helicopter hovering at various altitudes was collected on a sensor station. This sensor station consisted of the underwater FlyBy hydrophone array that was connected to a data acquisition (DAQ) system, which was housed in a floating surface unit. This DAQ unit digitized and stored the acoustic pressure data measured by the sensors and the surface microphone, which was mounted to this unit. A Sea-Bird temperature-depth probe was deployed several times during the course of the experiment to compute the sound speed profile within the waveguide. From an earlier Vibracore survey of the area by Scripps scientists[1], the sea-bed at the experiment site is known to consist of a layer, about 10 m thick, of fine-grained to very-fine-grained homogeneous sand, and that the ocean floor is flat and uniform. This experiment site has previously been used in underwater sound experiments involving fixed-wing aircraft[2].

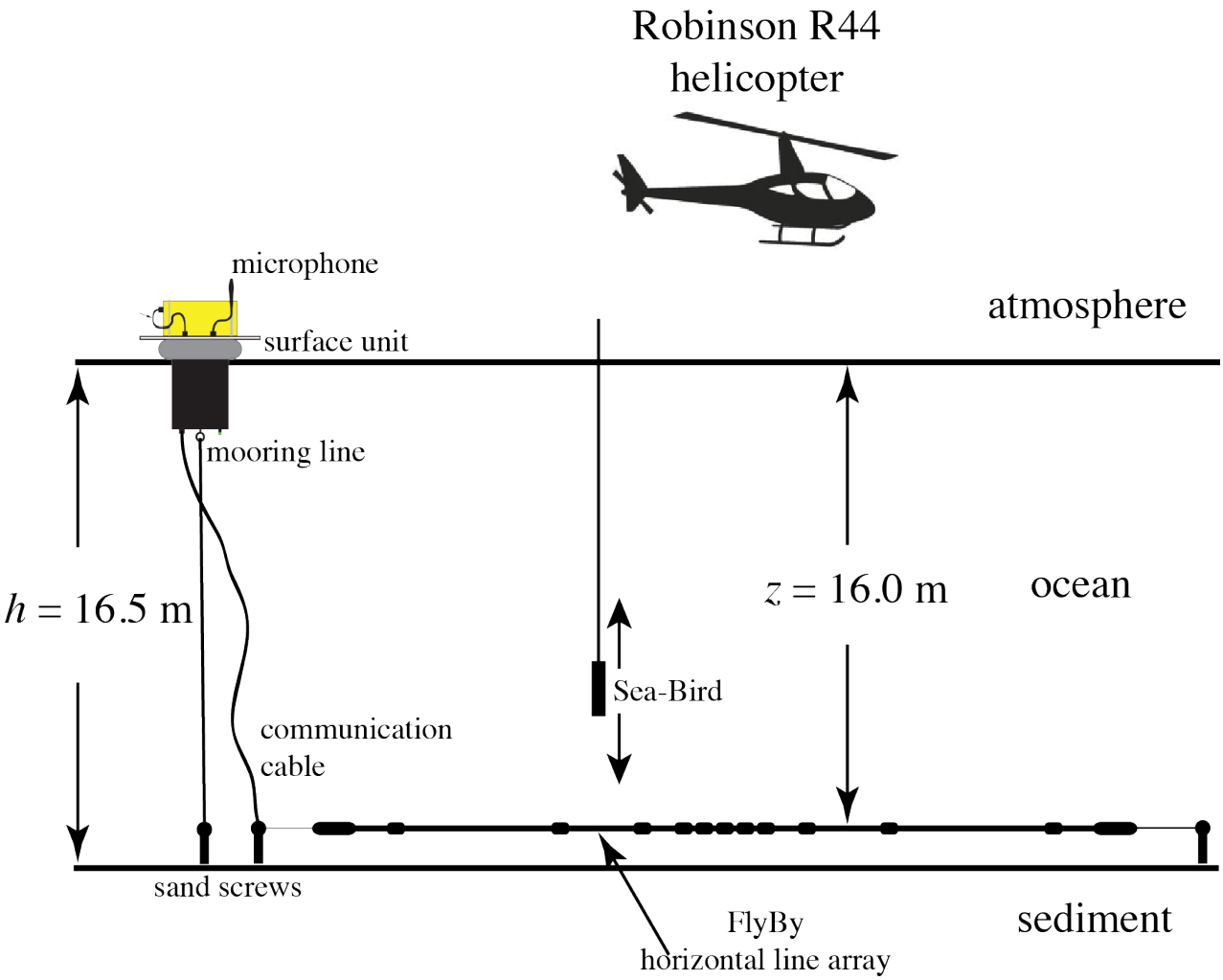

Figure 4.1: Schematic (not to scale) of the shallow-water underwater acoustic properties experiment in which an R44 helicopter acted as the air-borne acoustic source in flight operations above the 11-element FlyBy horizontal array.

The FlyBy hydrophone array is a non-uniformly spaced flexible array, with eleven calibrated ($1.4 \times 10^{-8}\,\mu Pa/V \;or\; -157\,dB\,re\,1\,V/Hz$) ITC 6050C hydrophones. The array consists of four nested sub-arrays, with corresponding inter-element separations of 0.325, 0.75, 1.5 and 3.0 m, for beamforming at half wavelength of the frequencies 250 Hz, 500 Hz, 1 kHz, and 2 kHz, respectively. The hydrophones have an omnidirectional response (Figure 4.2) and flat frequency response (Figure 4.3) from 3 Hz to 20 kHz with built-in low noise 20 dB pre-amps.

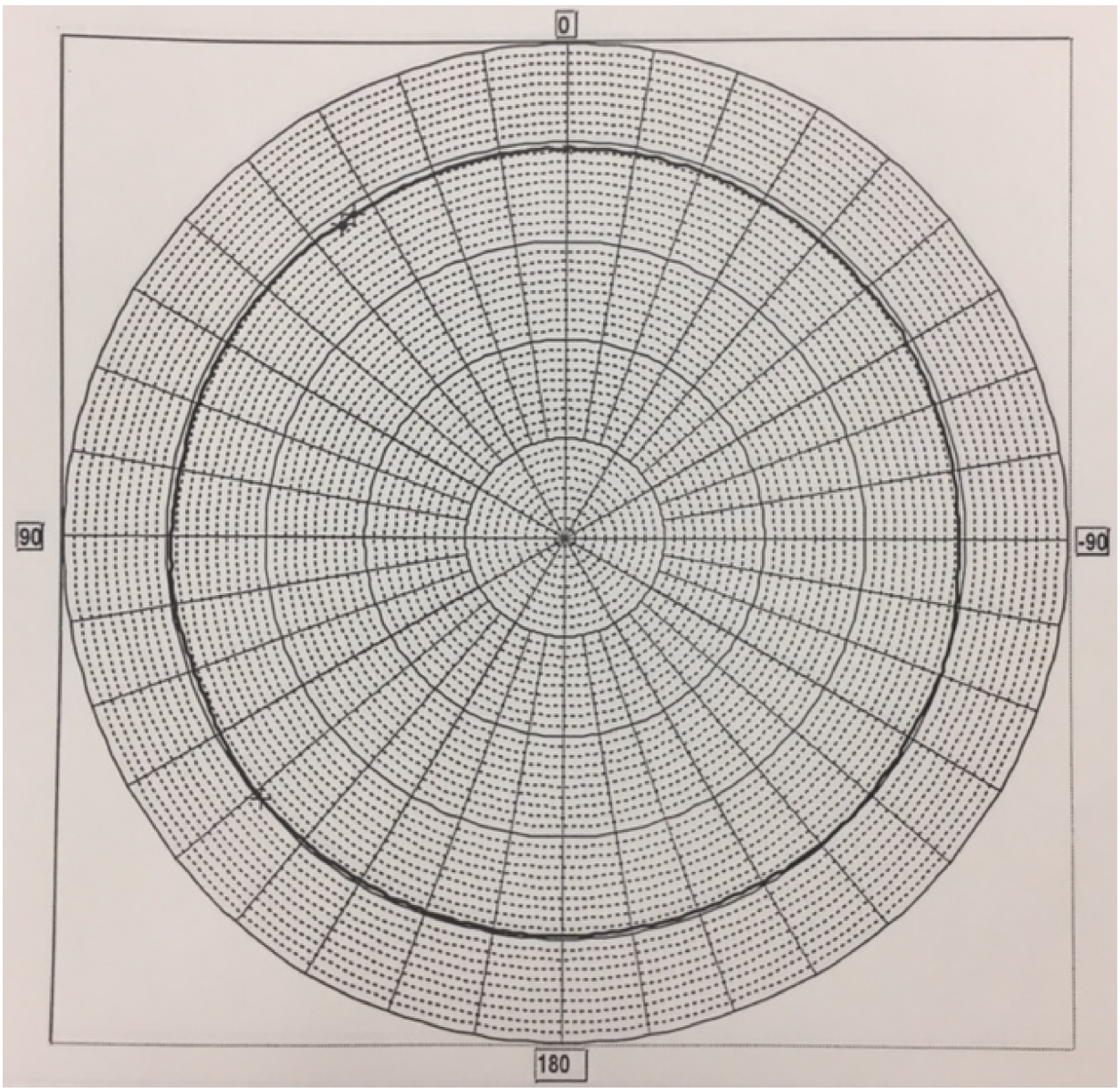

Figure 4.2: Omnidirectional response of one of the ITC-6050C sensors at 25 kHz.

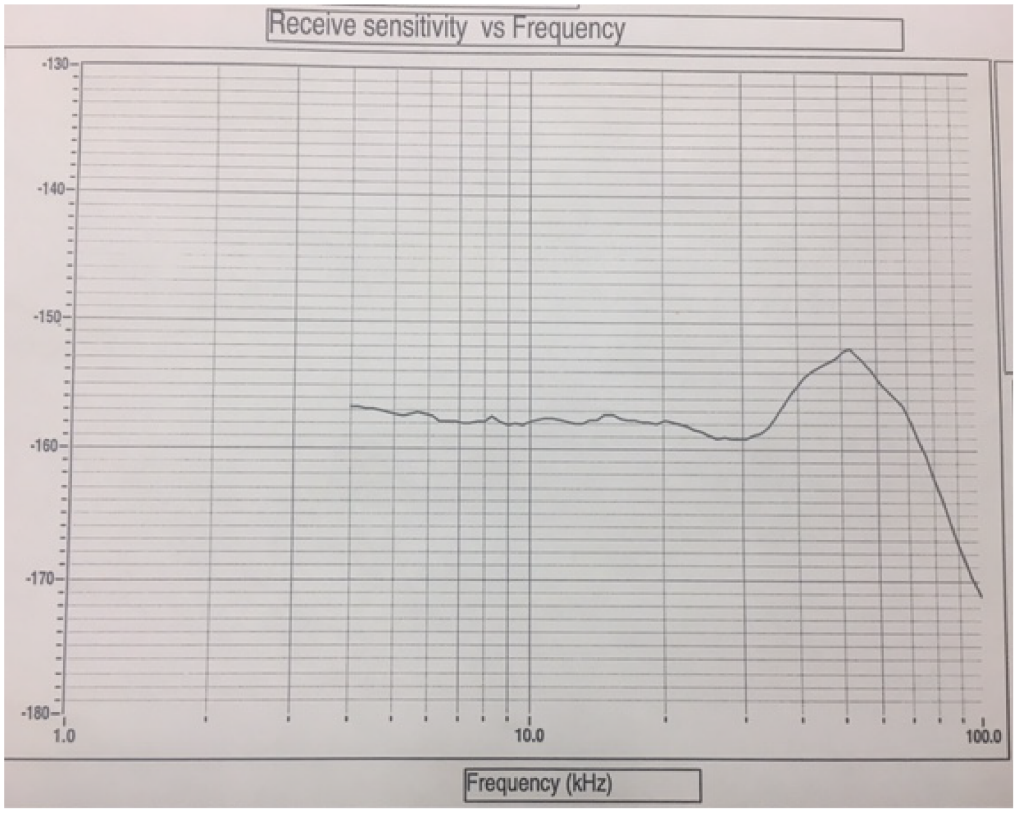

Figure 4.3: Receiver sensitivity, $dB/V/\mu Pa$, versus frequency response for one of the ITC-6050C sensors.

The hydrophones and microphone were sampled at a rate of 102.4 kHz by the DAQ system, which was attached by an underwater communication cable as shown in Figure 4.2. The FlyBy array and surface unit comprised the sensor station.

The floating surface unit, Figure 4.4, consisted of two watertight pressure housings, one containing the battery system and the other containing the National Instruments eXtensions for Instrumentation (PXI) computer system. The two housings attached to each other by stainless steel bands fastened with clips, which allowed for the plastic battery housing to be quickly exchanged for a second one containing freshly charged batteries.

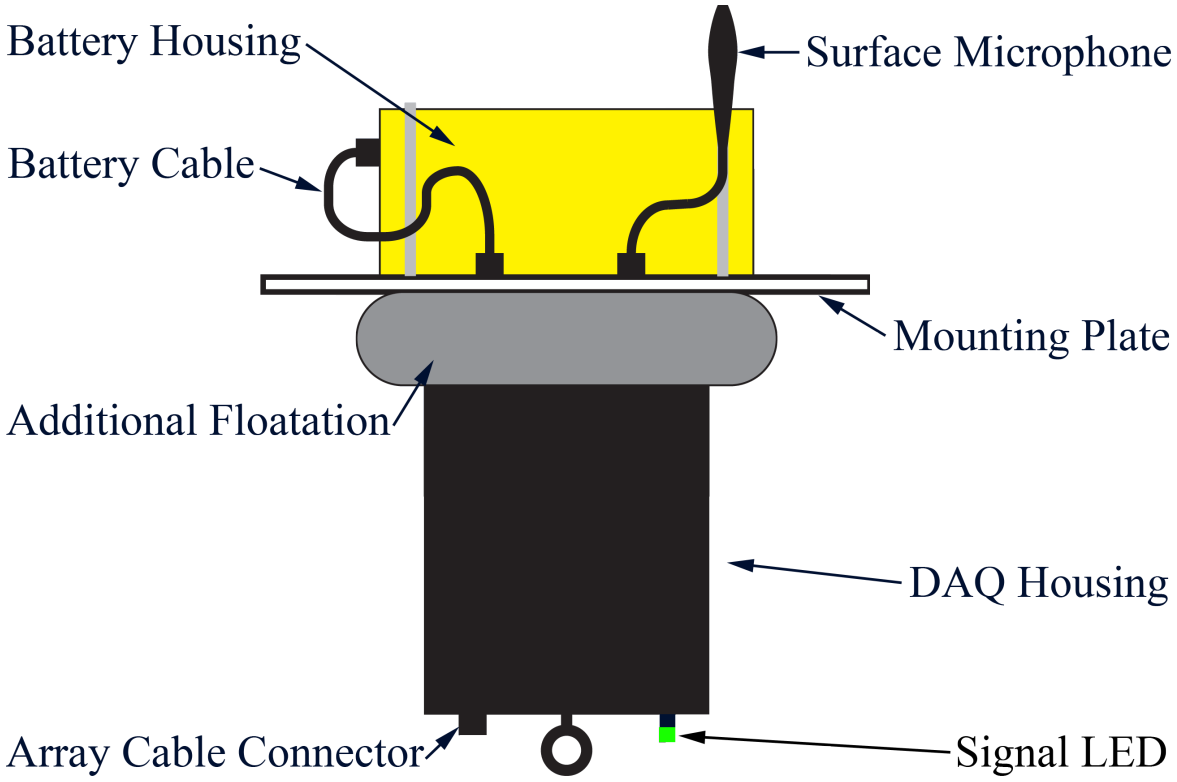

Figure 4.4: The surface floating DAQ (bottom black) and battery (top yellow) housings. The buoyancy is such that the water level is approximately at the mounting plate. This ensures the microphone mounted to the battery housing is approximately $1.0\ m$ above the water line.

The battery system consisted of eight lithium ion, $14.8\,V\ DC$, rechargeable battery packs consisting of four battery pairs connected in series, with the four pairs wired in parallel, thus delivering $29.6\,V\ DC$. This Supplied the minimum $18\,V\ DC$ required by the National Instrument PXI DAQ system contained within the second housing. Attached to the battery housing, which remained above the surface of the water was a microphone, an ITC 6050C receiver, at a height approximate distance of 1.0 m above the surface. The microphone was calibrated in air to the absolute units of pressure, Pascal's $(5.3 \times 10^{-8}\ \mu Pa/V)$. The DAQ collected the microphone and hydrophone data with all the channels time synchronized.

The DAQ electronics consisted of a National Instruments compact form factor PC with a PXI-8176 embedded controller. The sensors output was digitized by two PXI-4472 DAQ cards

capable of simultaneously sampling 8-channels each at 102 kHz with a dynamic range of 24-bit. When connected to power, the embedded computer ran Windows XP with a LabVIEW startup program, which triggered the DAQ boards to collect the raw data from the hydrophones and microphone. These data were stored on an internal hard drive. An Arduino UNO microcontroller controlled a pair of relays that supplied power to the DAQ system, thus ensuring a smooth distribution of power when the battery system was connected. This also allowed for custom programing of a duty cycle, if desired, although for this experiment it was programmed for continuous data collection.

A pair of divers, with a third diver for backup and safety, deployed the various sensors from a Boston whaler, the R/V Honey Badger, which was launched from Scripps Pier with the three divers on board. To facilitate the installation of the FlyBy on the day of the experiment, three sand screws and a mooring line had been installed during a previous dive operation. The divers deployed the FlyBy array arranged as a horizontal line array (HLA) at a depth of 16 m (i.e., 0.5 m above the seabed). The HLA was fastened tightly by a ratchet strap between two of the sand screws that were aligned on a bearing of 250^{O}, roughly perpendicular to shore. The most eastern end of the array was located at 32^{o} 53.859' N 117^{o} 15.808' W. The third sand screw was installed in the seabed just east of this position as the mooring point for the surface-floating DAQ and battery housings. The mooring line was a $1/2\ in$ braided line that was shorter than the underwater communication cable connecting the DAQ housing to the FlyBy array. This mooring line was taut pulling against the buoyancy of the upper unit thus preventing the motion of the sea surface from being transmitted to the HLA array.

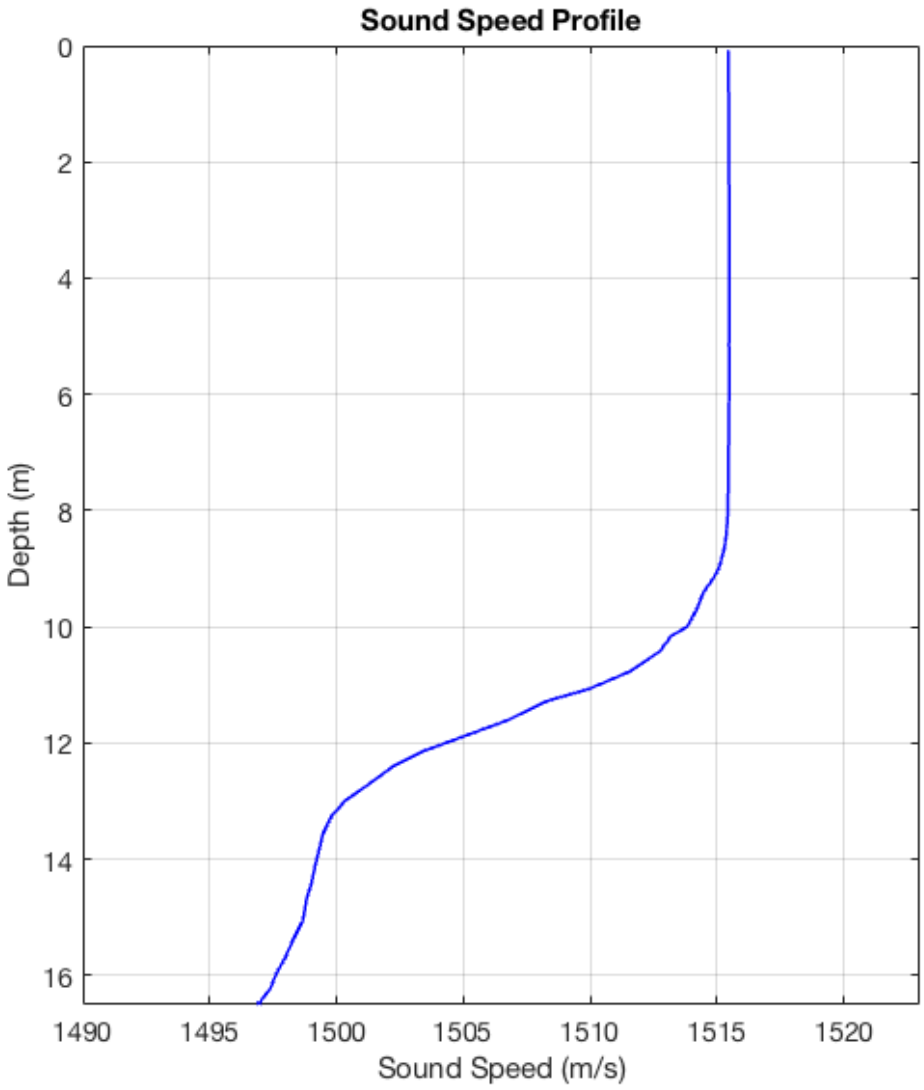

Figure 4.5: The sound speed profile of the channel during the initial helicopter experiment, as derived from the Sea-Bird temperature-pressure sensor data.

Once the FlyBy array was secured between the sand screws, the divers returned to the operations boat, which still carried the surface unit, and started up the system by connected the battery cable to the DAQ housing. The system was visually confirmed to be recording data from the underwater sensors and microphone by a unique blink signature on the external LED (Figure

4.5). The surface unit was affixed to the mooring line at the ocean surface and released. The Boston whaler was moved a distance away from the sensor station to 32^{o} 53.708' N 117^{o} 15.795' W, where it was anchored and all sound producing equipment was shutdown in preparation for the approach of the Robinson R44 helicopter. The Sea-Bird temperature-pressure probe was deployed from the whaler twice during the helicopter flight. The sound speed profile in the channel is shown in Figure 4.5, which was computed using the Chen and Millero[3] algorithm with the Sea-Bird temperature-depth data and an assumed salinity of 34 ‰.

4.3 Robinson R44 Helicopter Flight Operations

Figure 4.6: Photograph of the Robinson R44 helicopter during flight operations for the underwater acoustics experiment performed on the 6th of April 2015.

The Robinson R44 helicopter (Figure 4.6) used in this experiment was operated out of Montgomery-Gibbs Executive Airport in San Diego, CA, and performed a series of low-altitude

maneuvers at the experiment site. To track the flight path of the helicopter, a GPS unit with a built–in, calibrated, barometric altimeter was mounted in the cockpit of the R44.

Montgomery-Gibbs airfield is located south of the sensor station and roughly $24\ km$ inland from the coast, relative to the sensor station location. After lifting off from the airfield the R44 helicopter flew northwest towards the coast of La Jolla to began its flight operations. The entire flight operations above the sensor station of the R44 helicopter from the GPS unit is shown in Figure 4.7.

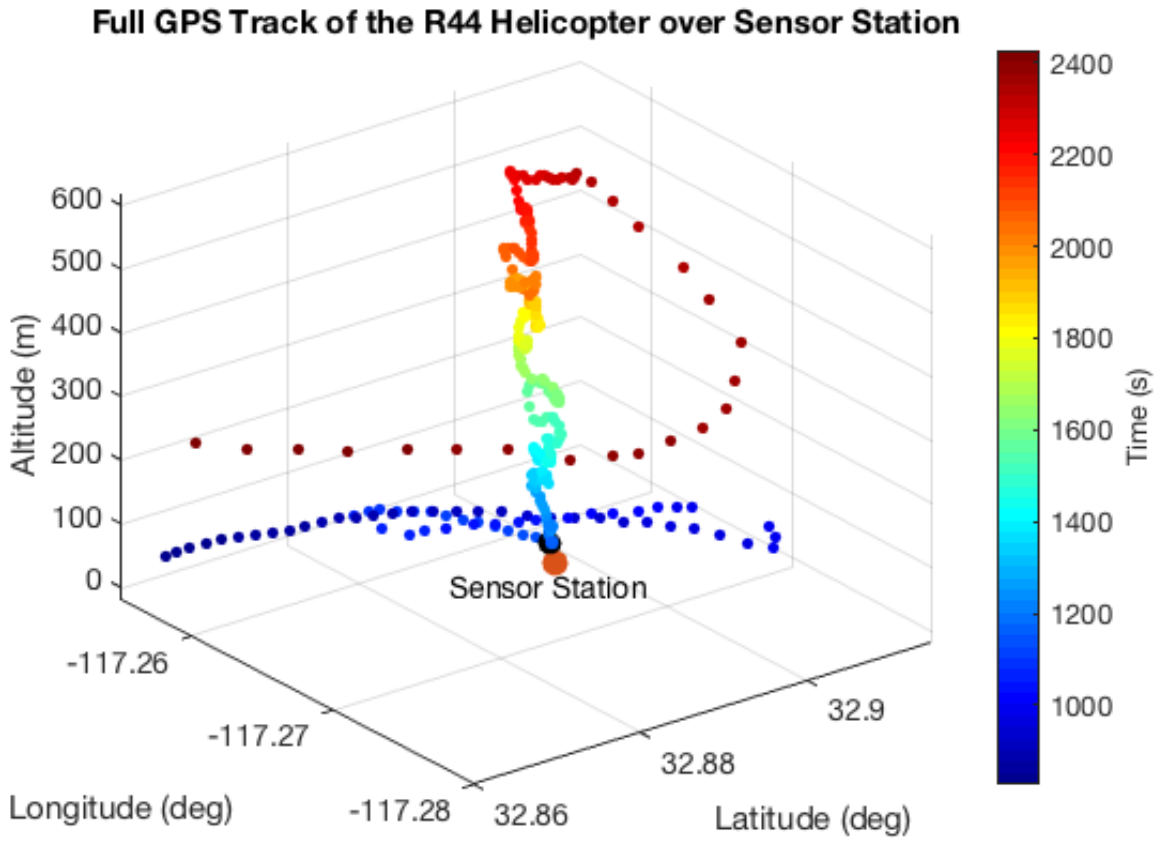

Figure 4.7: The GPS track is shown for the helicopter flight operations above the sensor station during the shallow-water underwater helicopter acoustic properties experiment.

Once at the coastline, the R44 helicopter approached the sensor station location on a northbound heading to over fly the sensor station broad-fire to the array and parallel to the coastline at cruise speed, approximately 90 $knots$. Once past the sensor station, the R44 helicopter operated a 180° turn and performed another over-flight from north to south. Following these two over-flights, the helicopter came to a hover 30.5 m over the sensor station.

The hover part of the helicopter operations now began with a direct line of sight between the pilot and the surface unit. The helicopter held altitude and position above the sensor station for approximately 30 seconds before increasing its altitude by 30.5 m. This pattern was repeated at 20 altitudes to a maximum altitude of 610 m. The total flight time, from take off to touch down, was approximately 45 minutes, of which 30 minutes were used for flight operations at the sensor station.

4.3.1 Robinson R44 Helicopter Over-Flights

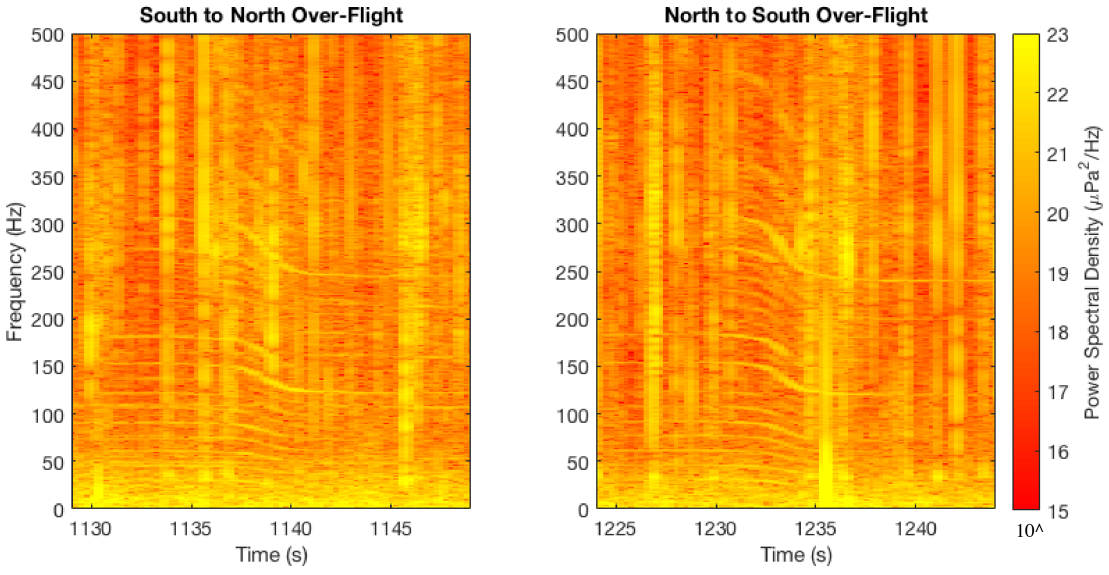

Figure 4.8: Spectrograms from the surface microphone of the two fly-bys flight operations by the R44 helicopter displaying a strong Doppler shift as the helicopter shifts from an approach to a departure heading

relative to the sensor station. The x-axis is the time in seconds from the beginning of the experiment. The point the helicopter was as the closed point of approach as at approximately 1139 seconds for the first fly-by, south to north, and 1234 seconds for the north to south fly-by.

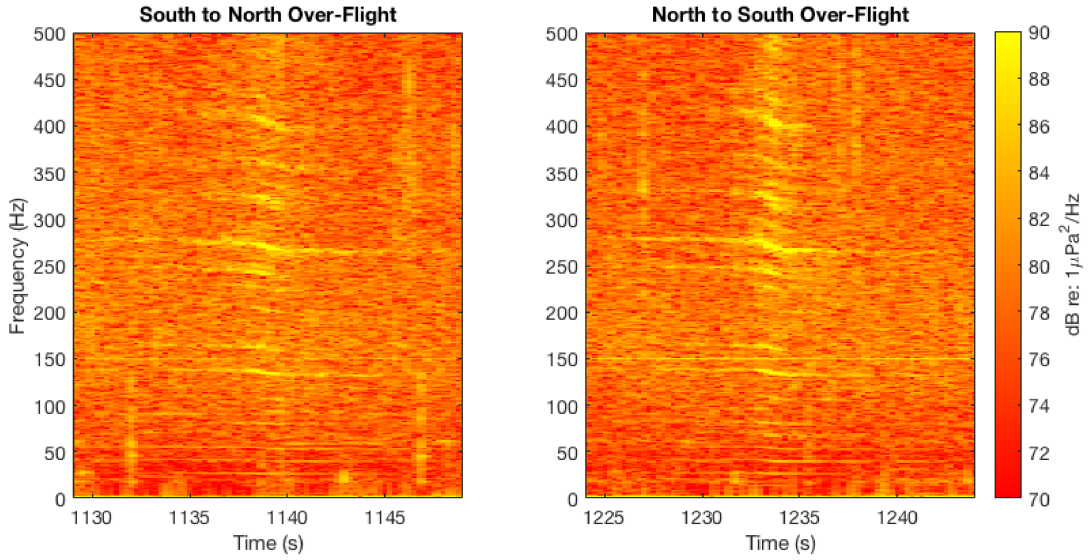

Figure 4.9: Spectrograms from an underwater sensor of the two fly-bys flight operations by the R44 helicopter displaying a strong Doppler shift as the helicopter shifts from an approach to a departure heading relative to the sensor station. The x-axis is the time in seconds from the beginning of the experiment. The point the helicopter was as the closed point of approach as at approximately 1139 seconds for the first fly-by, south to north, and 1234 seconds for the north to south fly-by.

The two over-flights were performed at an altitude of approximately 30 m and broad-fire (perpendicular) to the HLA, with the first flight on a northbound heading and the second on a southbound heading. As illustrated in Figures 2.1 and 2.3 the helicopter produced strong spectral lines corresponding to the harmonics of the main rotor and tail rotor, as well as the engine. Above and below the surface these spectral lines show a strong Doppler shift as the helicopter passed over the sensor station as shown in Figure 4.8 and 4.9.

The Doppler shift displays a downward frequency shift as the helicopter changes from an approach to a departure heading, relative to the sensor station. The Doppler shift produced by fixed-wing aircraft has been successfully used in the past for inversion techniques to recover the sound speed of the sediment[4].

4.3.2 Underwater Intensity from a Robinson R44 Helicopter with Increasing Altitude

After the two over-flights, the Robinson R44 helicopter came to a hover $30.5\ m$ over the sensor station, with the pilot using line of sight between the helicopter and the floating surface unit. The helicopter pilot then proceeded to hover for $30\ s$ before increasing altitude by $30.5\ m$, this process was repeated to an altitude of $610.0\ m$. The range and altitude data of the helicopter during the hover portion of the flight operations is shown in Figure 4.10.

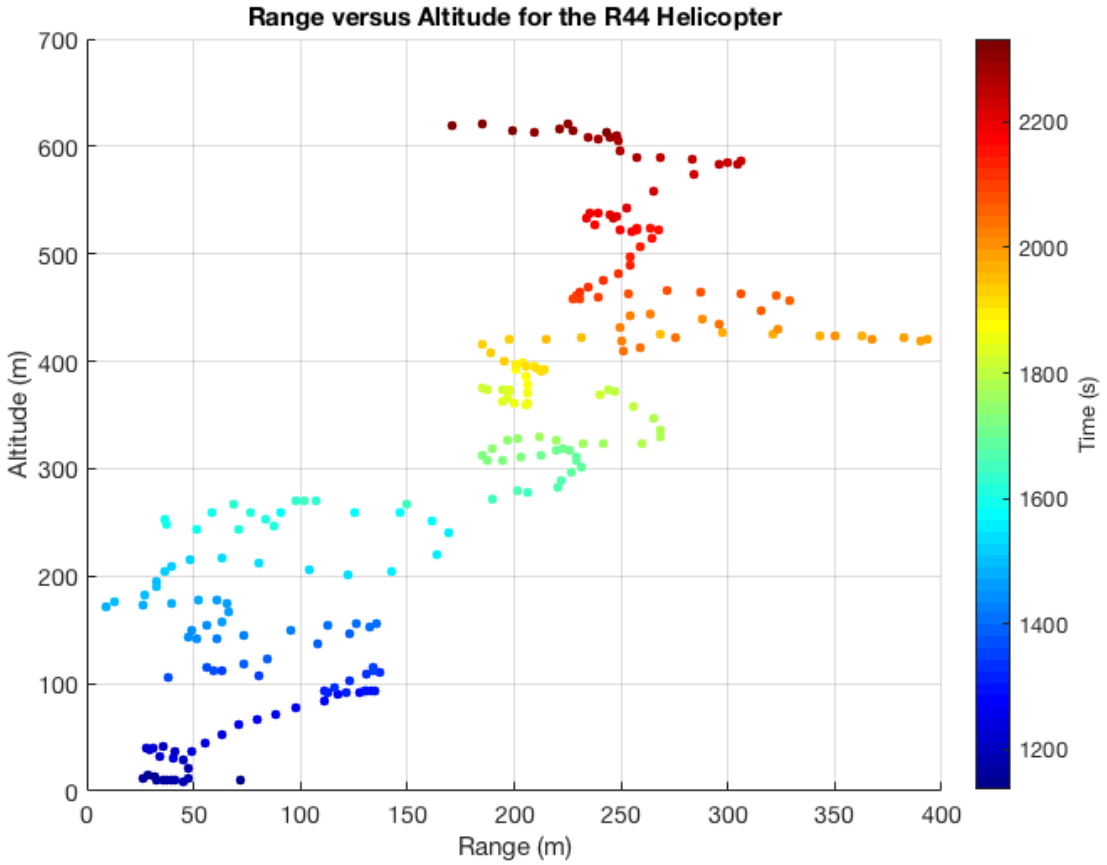

Figure 4.10: GPS track of the helicopter for the hover flight maneuvers above the sensor station with horizontal range from the Eastern point of the horizontal array. The pilot held each using line of sight with the surface-floating unit; this caused the range to increase with altitude.

The horizontal range between the helicopter and sensor station increases with altitude due to the pilot maintaining line-of-sight with the surface unit. The data from the individual 30 s hovers was used to determine the power spectrum of the underwater acoustic signal produced by the R44 helicopter.

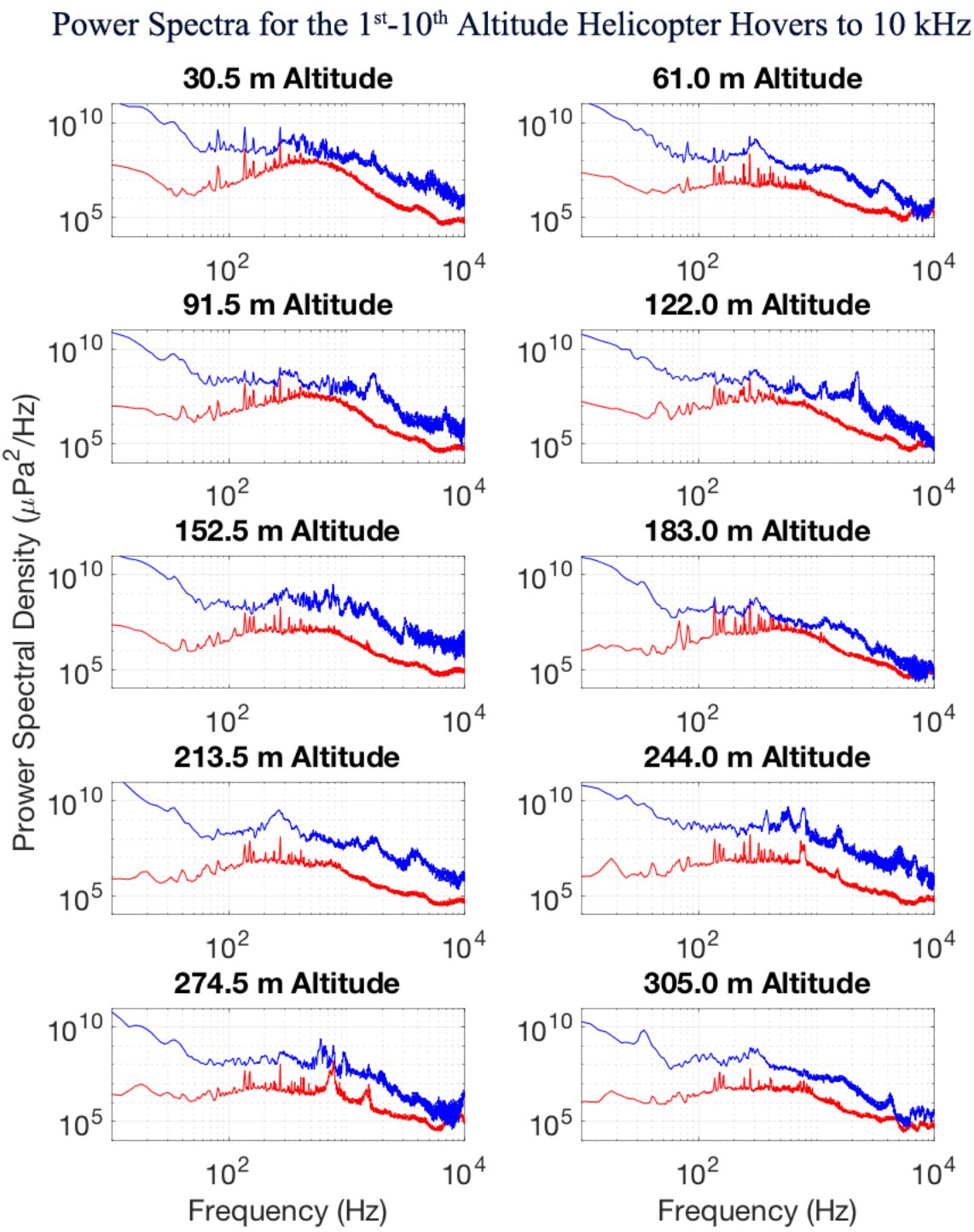

Figure 4.11: Spectra from the surface in-air sensor (blue) and an underwater hydrophone (red) for the first ten of the 30 s helicopter hovers. The hovers begin at 30.5 m and increase by 30.5 m until a max height of 610 m. The spectra were formed from the 30 s time series for each hover with a frequency resolution of 2 Hz.

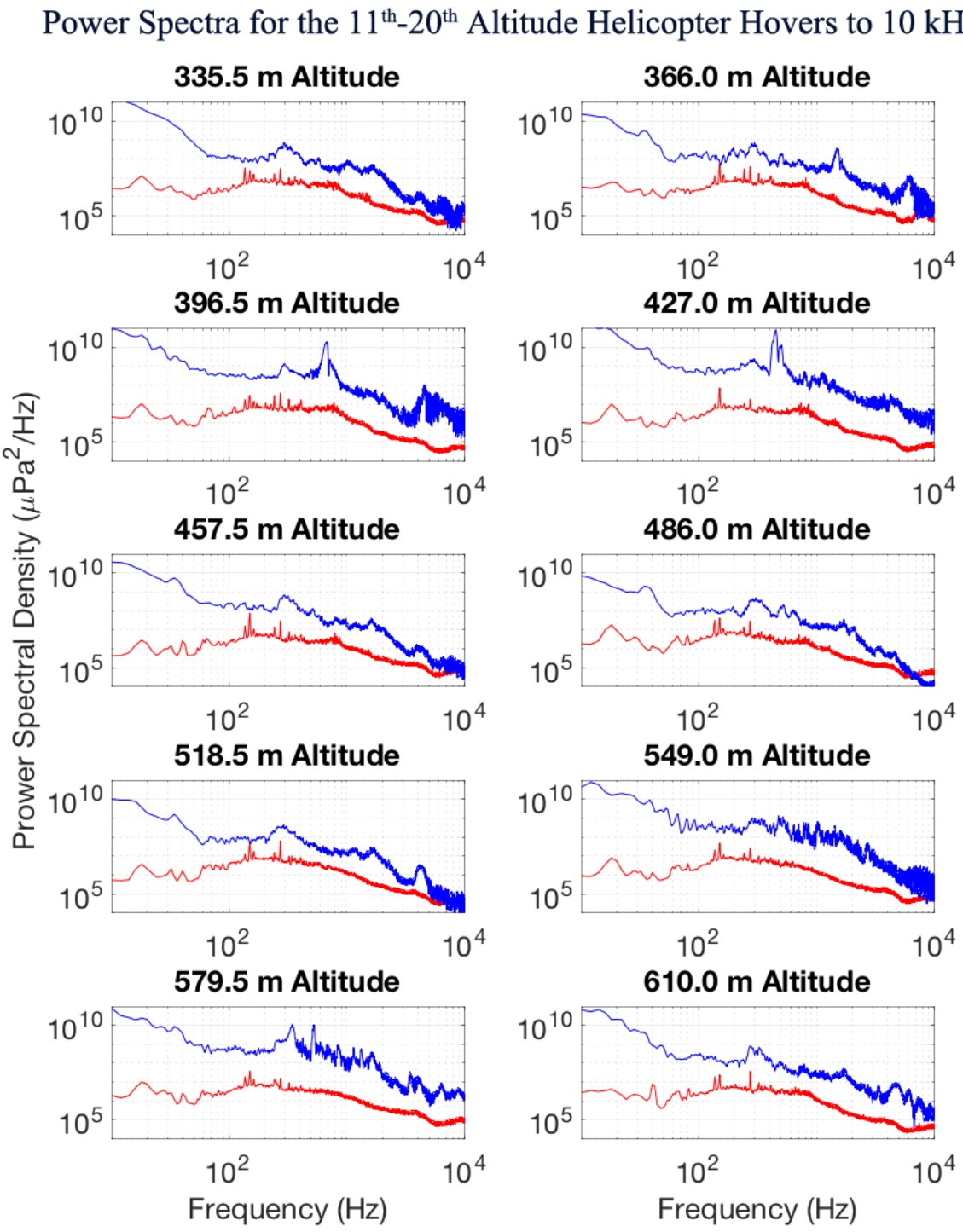

Figure 4.12: Spectra from the surface in-air sensor (blue) and an underwater hydrophone (red) for the last ten (11-20) of the 30 s helicopter hovers. The hovers begin at 30.5 m and increase by 30.5 m until a max height of 610 m. The spectra were formed from the 30 s time series for each hover with a frequency resolution of 2 Hz.

In Figure 4.11 and Figure 4.12 the pressure detected is shown in absolute units, $\mu Pa^2/Hz$, at the in-air surface sensor (blue) and at a single underwater hydrophone (red) for all twenty altitudes. The units of pressure are used instead of the usual decibels, as decibels are a relative unit and are not equivalent between the mediums of atmosphere and seawater[5]. The pressure levels at both sensors decay as expected, although the characteristic sharp peaks of the helicopter's harmonics are not present in the spectrum of the microphone data at higher altitudes. In the atmosphere the strong spectral lines of the main rotor and tail rotor decrease rapidly, no longer visible as peaks in the spectrum above $213.5\,m$. As the helicopter increased in altitude, the distance between the sound source and the surface sensor also increased in horizontal range. The intensity from the helicopter sound decays in air spherically as $1/r^2$, with r being the absolute distance between helicopter and the microphone The increase in horizontal range with altitude reduces the energy received by the microphone in the atmosphere[6].

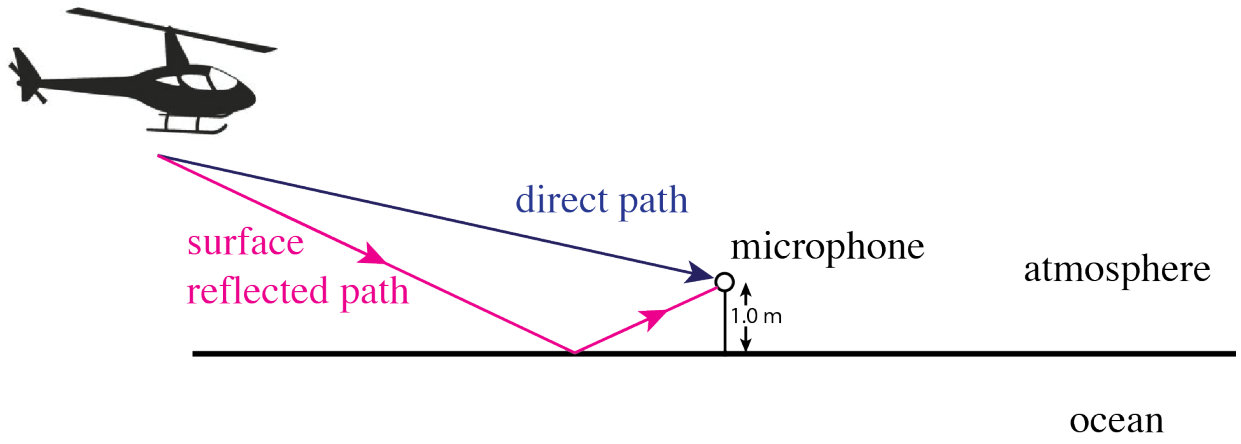

Figure 4.13: Ray schematic of the direct and surface reflected paths received by the microphone.

Figure 4.13 is a ray representation with the helicopter as a point source and the microphone as a point receiver. Above the surface the microphone only detects two rays. These

two rays received are the direct ray and the sea-surface reflected ray. This produces the classical surface-image or Llyod-mirror interference pattern[7]. Comparatively, the underwater sensor receives a refracted direct ray, as well as numerous other rays that are refracted into the water column within the 13° cone (Figure 2.4). Also shown in Figure 2.4, there are additional rays refracted into the water column outside the 13° cone due to the roughness of the sea surface.

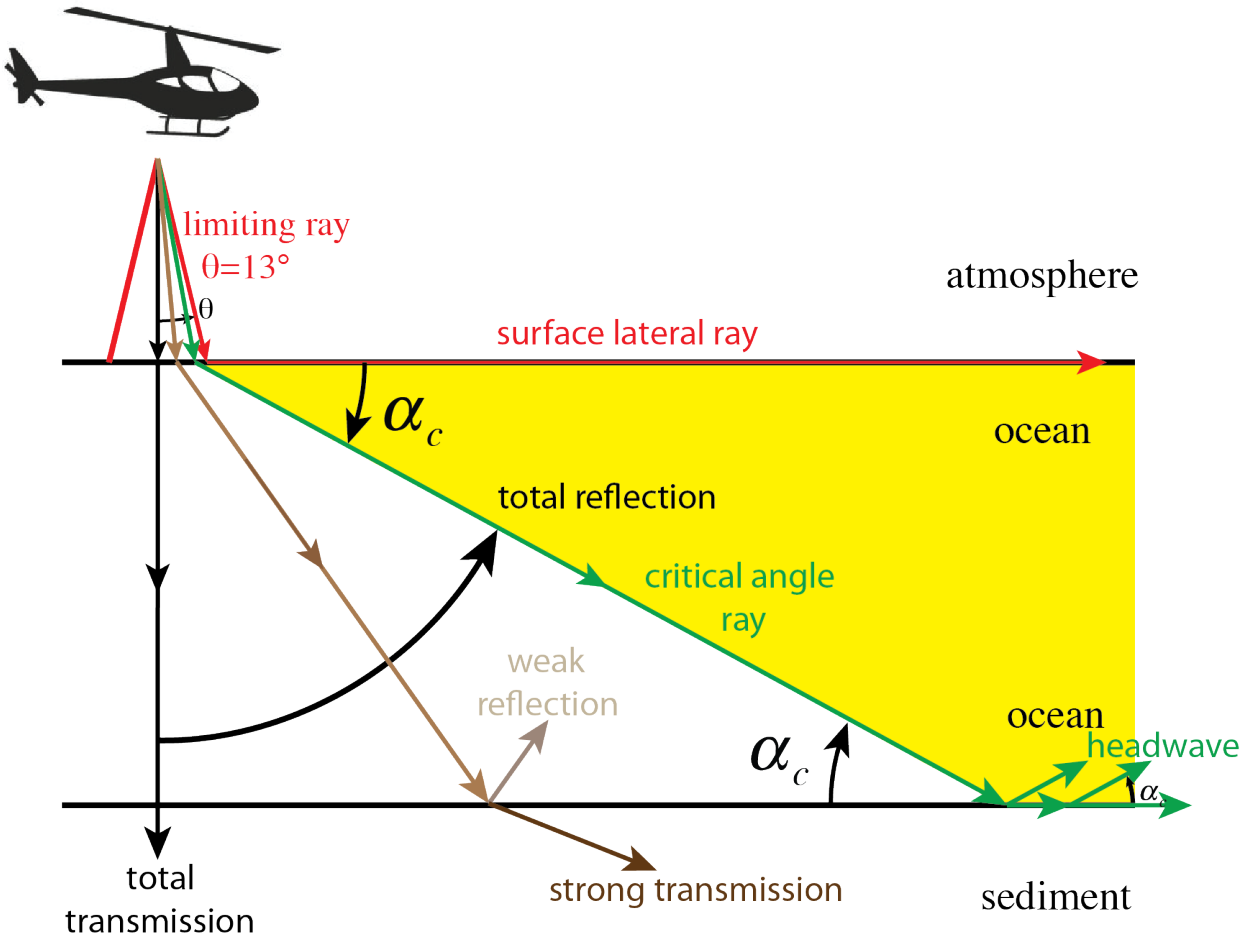

Figure 4.14: Ray diagram of the different regions of sound transmission in the underwater waveguide.

The geometry of an ideal underwater waveguide creates two regions, which are separated by the critical angle with the seabed. For angles less than the critical we have total reflection

within the waveguide, shown by the yellow region in Figure 4.14. For angles greater than the critical angle and less then 90° we have partial transmission into the seabed. This is also shown in Figure 4.15 by the reflection coefficient of ocean-sediment interface. For the ideal case the reflection coefficient is 1 for angles up to the critical angle. For angles above the critical angle the reflection coefficient decreasing rapidly as most of the sound is transmitted into the fine-grained sediment layer.

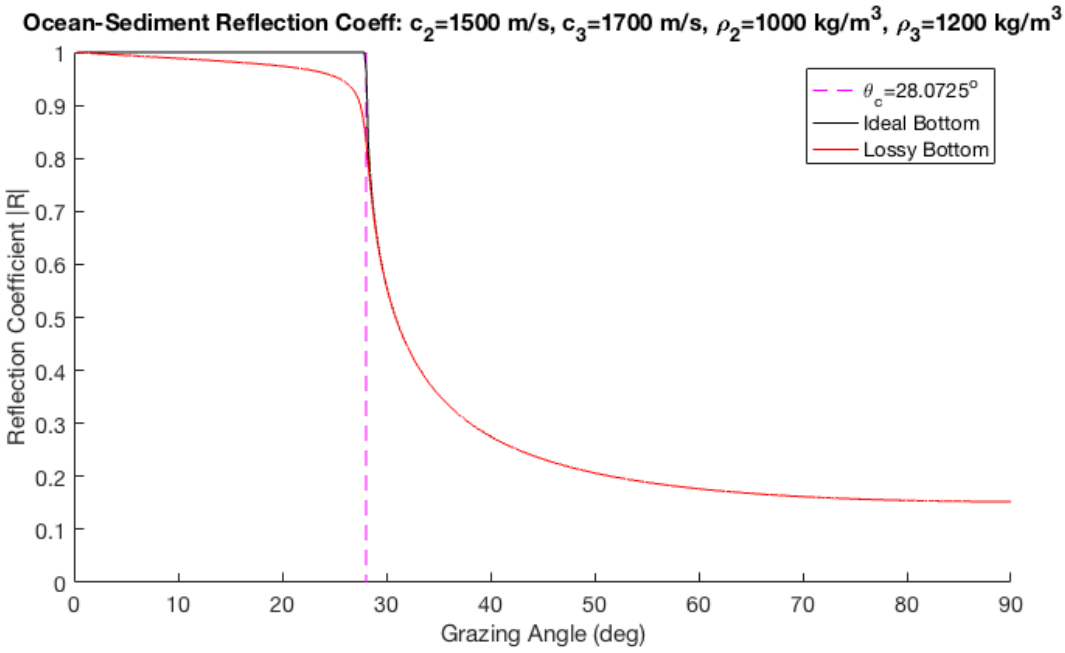

Figure 4.15: Reflection coefficient as a function of grazing angle for a fine to very-fine grained sediment for the ideal waveguide case as well as with attenuation.

Once refracted into the water column the sound propagates within the waveguide by two methods: by normal modes or the head wave. The superpositions of the rays reflected between the sea surface and sediment form the propagating normal modes. Normal modes spread cylindrically within the water column as its intensity decays as $1/r$. The intensity of the propagating head wave decays as $1/r^4$, as proven in Section 3.7. Air-to-liquid sound

propagation has been documented using wave theory[8, 9] and ray theory[10 11 12 13]; see also Chapman and Ward[14, 15].

Four figures are presented displaying the altitude dependence of the spectral properties of the underwater sound field produced by the hovering Robinson R44 helicopter. The first two Figures 4.16 and Figure 4.17, displays the noise bandwidth of the R44 Robinson helicopter, while Figures 4.18 and Figure 4.19 focus on the harmonics of the main rotor and tail rotor along with the additional noise produced up to $1\ kHz$. During the experiment, there were additional aircraft from the surrounding civilian airports and military bases in the experiment area. An example of this is the additional visible spectral signature of a distant US Navy Osprey aircraft, as it flew from east to west, during two the altitude hovers of $244\ m$ and $274.5\ m$. The sound from this aircraft, although a great distance away, propagated within the underwater waveguide and appears as bumps around frequencies $800\ Hz$ & $1500\ Hz$ in the underwater spectra. The propagating normal modes, along with the reduced cylindrical spreading, sustain the strong harmonics lines produced by the Robinson R44 helicopter in the underwater spectra with increasing altitude and range. The spectral lines of the strongest frequencies produced by the helicopter are present in the underwater spectrum at all altitudes.

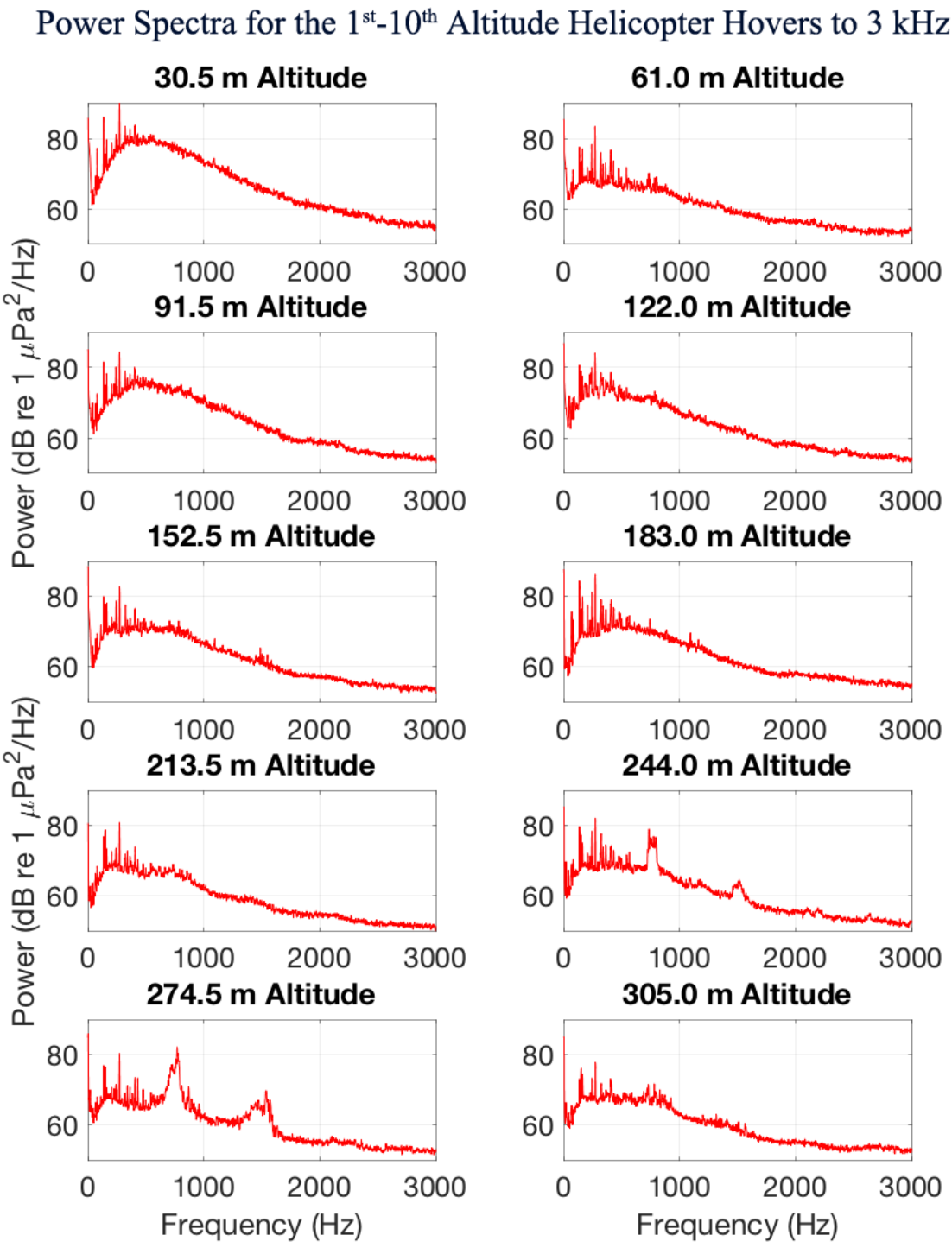

Figure 4.16: Spectra from an underwater hydrophone for the first ten of the 30 s helicopter hovers. The hovers begin at 30.5 m and increase by 30.5 m until a max height of 610 m. The spectra were formed from the 30 s time series for each hover with a frequency resolution of 2 Hz, and display the entire frequency bandwidth (13 Hz − 3 kHz) of the sound produced by the R44 Robinson helicopter.

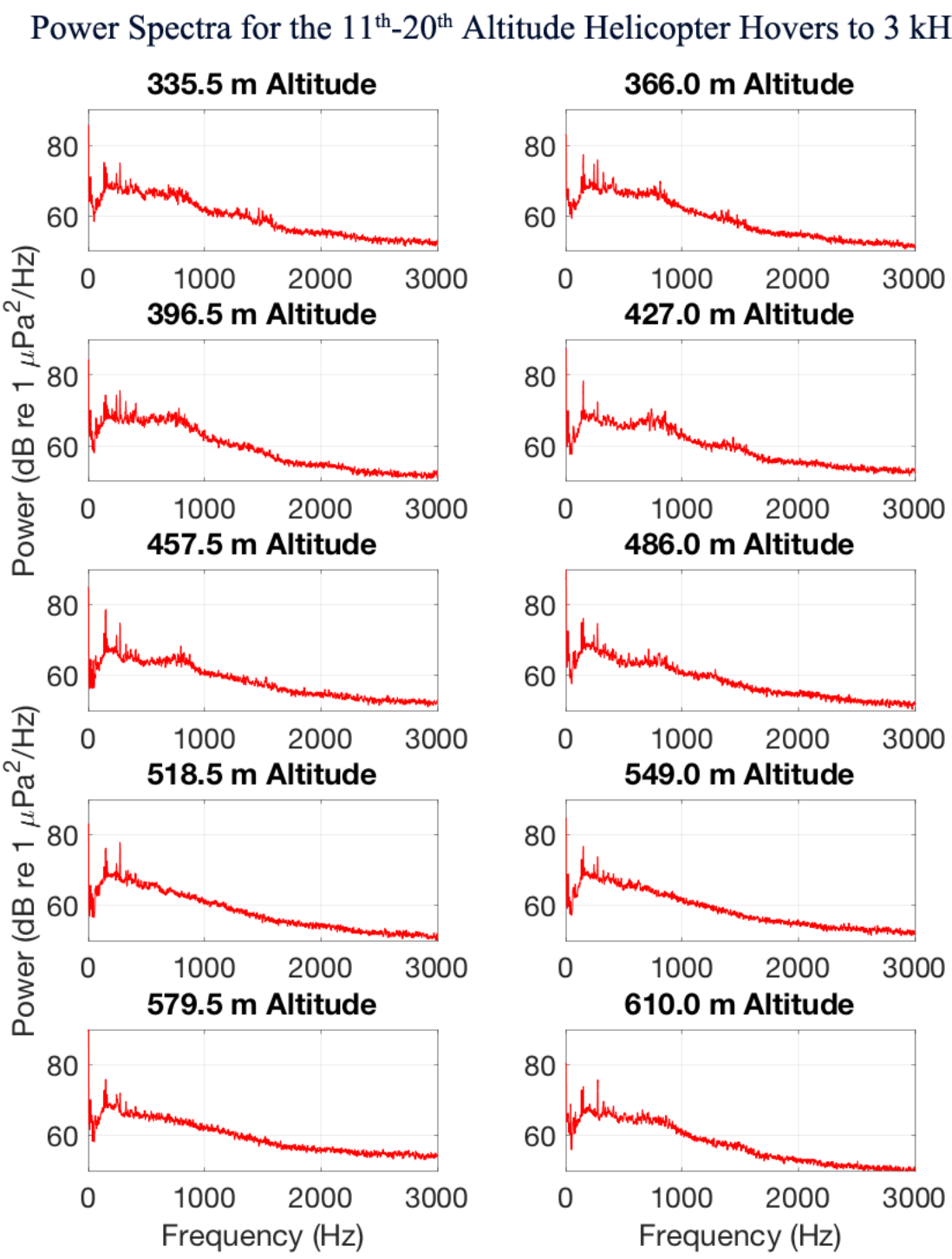

Figure 4.17: Spectra from an underwater hydrophone for the last ten (11-20) of the 30 s helicopter hovers. The hovers begin at 30.5 m and increase by 30.5 m until a max height of 610 m. The spectra were formed from the 30 s time series for each hover with a frequency resolution of 2 Hz, and display the entire frequency bandwidth (13 Hz – 3 kHz) of the sound produced by the R44 Robinson helicopter.

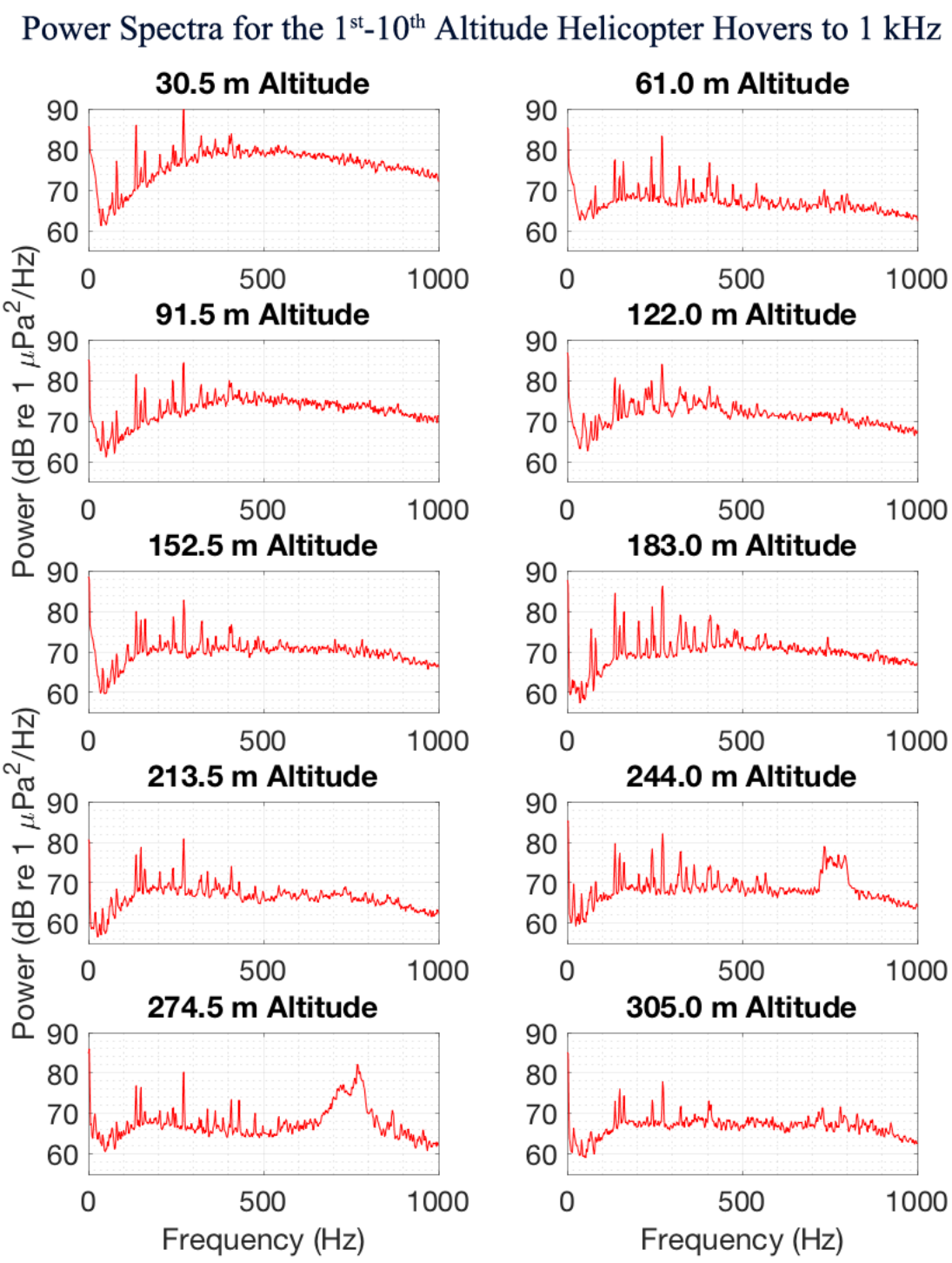

Figure 4.18: Spectra from an underwater hydrophone for the first ten helicopter hovers. The spectra was formed from the 30 s time series for each hover with a frequency resolution of 2 Hz, and display the main harmonics produced by the R44 Robinson helicopter to a frequency of 1 kHz.

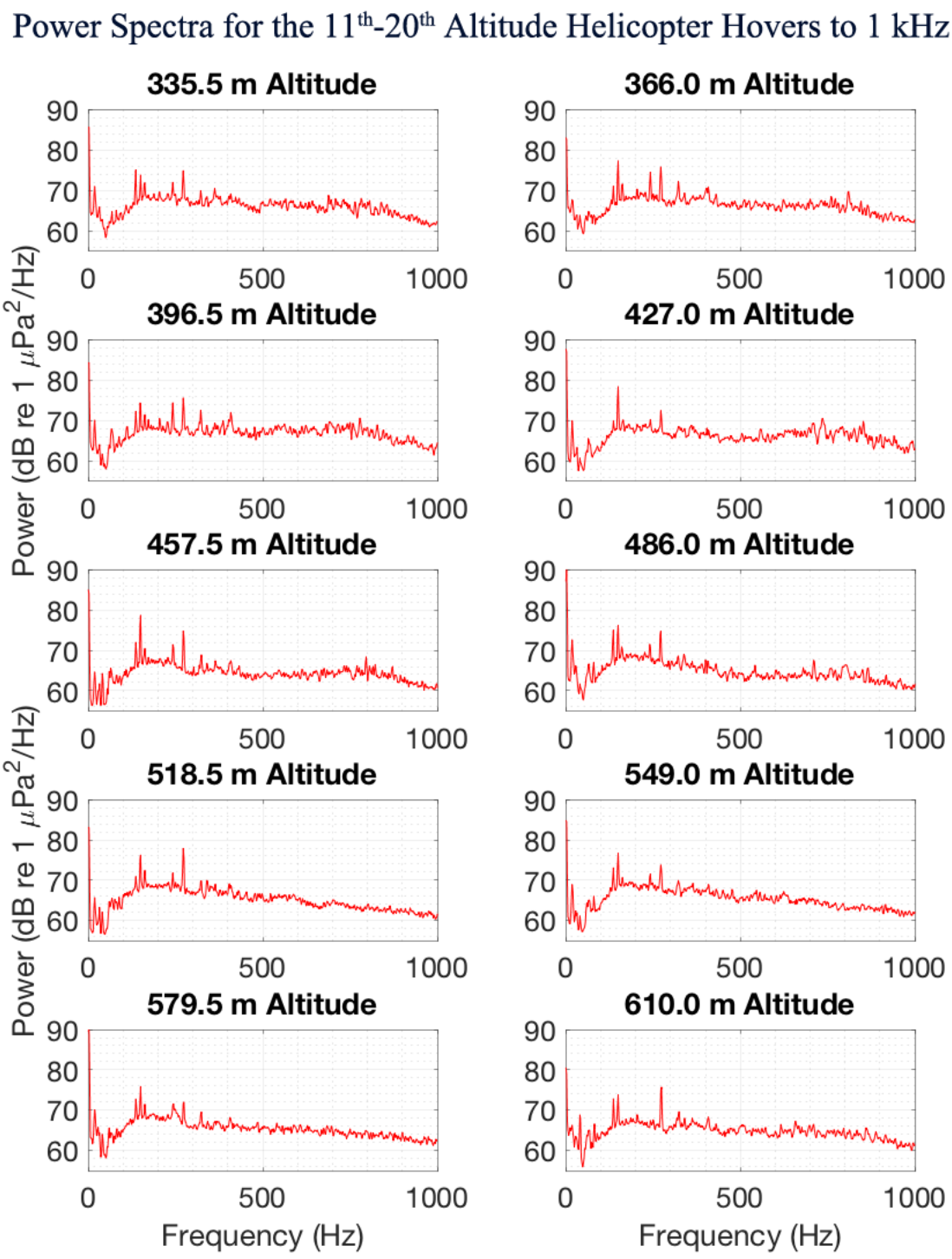

Figure 4.19: Spectra from an underwater hydrophone for the last ten helicopter hovers. The spectra was formed from the 30 s time series for each hover with a frequency resolution of 2 Hz, and display the main harmonics produced by the R44 Robinson helicopter to a frequency of 1 kHz.

In Figure 4.20, five of the $30\,s$ altitude hovers, $30.5\,m$, $152\,m$, $305\,m$, $457\,m$, and $610\,m$, show the decline in power of the harmonics and the overall noise produced within the helicopter frequency bandwidth with increasing altitude. The ambient noise level is also shown and was determined using a $30\,s$ segment of data before the helicopter arrived at the sensor station.

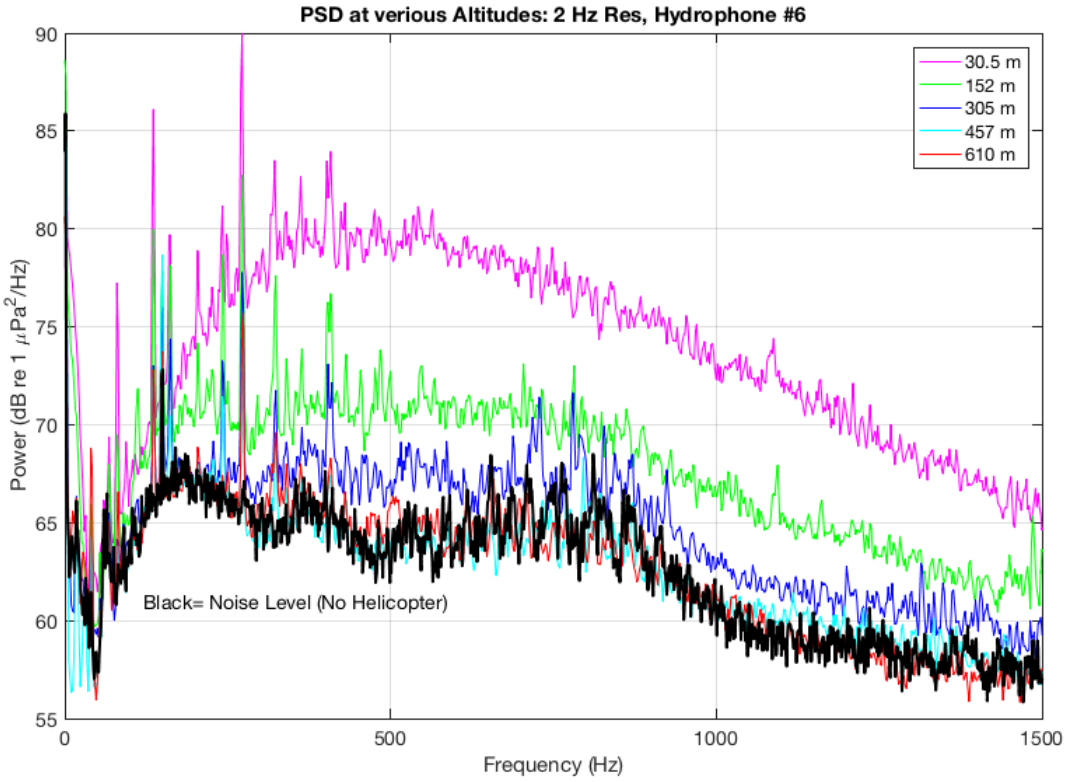

Figure 4.20: Power spectrum of the helicopter hovering at altitudes 31, 152, 305, 457, and 610 meters on an underwater receiver. The ambient noise spectrum before the helicopter is on station is shown in black.

The measured dB levels for the harmonics of $80\,Hz, 136\,Hz, and\ 272\,Hz$ are shown in Table 4.1. The harmonic at $80\,Hz$ is the sixth harmonic of the main rotor and the fundamental frequency of the tail rotor, and is the first dominate peak in the underwater spectra. Lower

frequency spectral lines fall below the modal cut-off of the channel. The harmonic at 136 Hz is the fundamental engine harmonic, and may contain a small contribution from the main rotor. The harmonic at 272 Hz is the second harmonic of the helicopters engine and is the dominant peak within the underwater spectra.

Table 4.1: Ambient noise levels for three helicopter harmonic frequencies.

	80 Hz	136 Hz	272 Hz
Ambient Noise	62.2 dB	65.8 dB	65.6 dB

Table 4.2: Table of three harmonic frequencies (80 Hz, 136 Hz, and 272 Hz) produced by the Robinson R44 helicopter for all 20 altitudes in decibels received on an underwater sensor.

Altitude	80 Hz	136 Hz	272 Hz	Altitude	80 Hz	136 Hz	272 Hz
30.5 m	77.23 dB	86.09 dB	89.98 dB	335.5 m	65.08 dB	75.10 dB	74.89 dB
61.0 m	71.08 dB	77.58 dB	83.38 dB	366.0 m	63.94 dB	71.07 dB	75.82 dB
91.5 m	72.52 dB	81.57 dB	84.43 dB	396.5 m	64.87 dB	72.24 dB	75.54 dB
122.0 m	71.26 dB	80.70 dB	84.05 dB	427.0 m	62.61 dB	69.88 dB	72.42 dB
152.5 m	69.48 dB	79.97 dB	82.75 dB	457.5 m	63.80 dB	71.96 dB	74.79 dB
183.0 m	73.39 dB	84.45 dB	86.22 dB	488.0m	67.02 dB	75.01 dB	74.72 dB
213.5 m	68.45 dB	76.88 dB	80.83 dB	518.5 m	65.24 dB	70.92 dB	77.86 dB
244.0 m	70.25 dB	79.67 dB	82.05 dB	549.0 m	65.90 dB	73.06 dB	73.75 dB
274.5 m	67.88 dB	76.85 dB	80.23 dB	579.5 m	65.37 dB	72.74 dB	71.98 dB
305.0 m	64.15 dB	73.01 dB	77.77 dB	610.0 m	66.56 dB	72.80 dB	75.69 dB

The spectral power for the strong harmonic of 272 Hz, harmonic of the main rotor, tail rotor, and the R44's engine, from each 30 s hover intervals at each experimental hover altitude are shown in Figure 4.21.

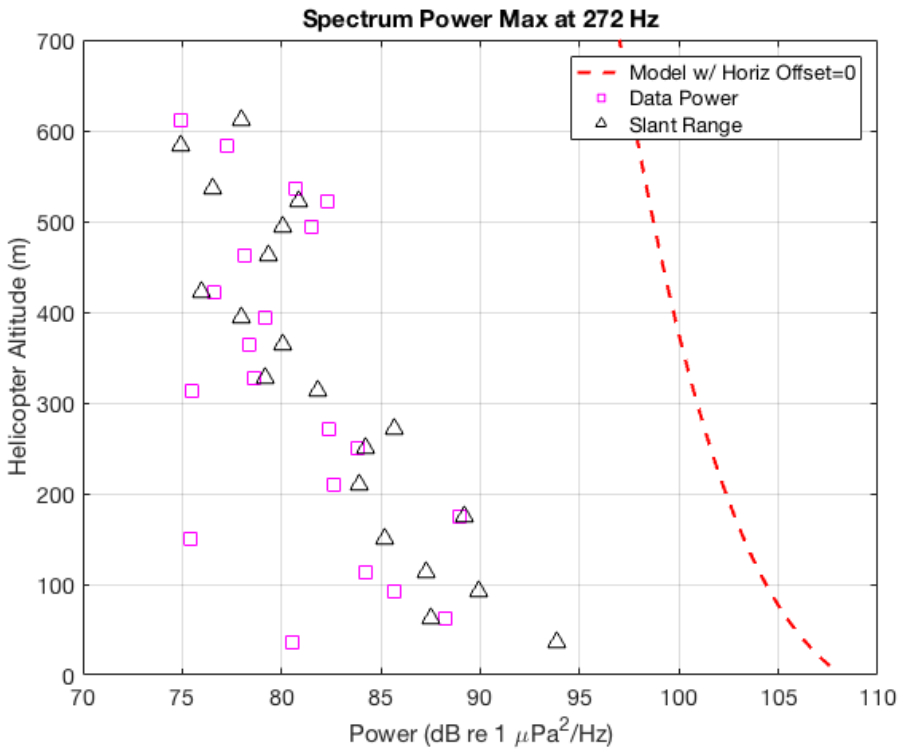

Figure 4.21: Spectral peak power level at the 272 Hz line from 20 averaged altitudes, 30.5 m to 610 m with 30.5 m increments (magenta squares). Analytical shallow water model (black diamonds) computed with the average GPS altitude and range. The dashed red line is the analytical shallow model with r=0, helicopter maintaining altitude directly above the underwater sensor, plotted for reference.

The magenta squares are the maximum value of the power spectrum from the data in the vicinity of 272 Hz versus the average altitude during each hover calculated from the helicopter GPS barometric sensor. The black triangles are the predicted underwater spectral power from the three-layer model, Equation 3.19b, with the scaling constant Q given a value of 30,000, the average GPS position used for r, and the barometric sensor data for z_s. The dashed red line is the

shallow-water model's predicted spectral power if the helicopter maintained altitude directly above the underwater sensor ($r = 0$).

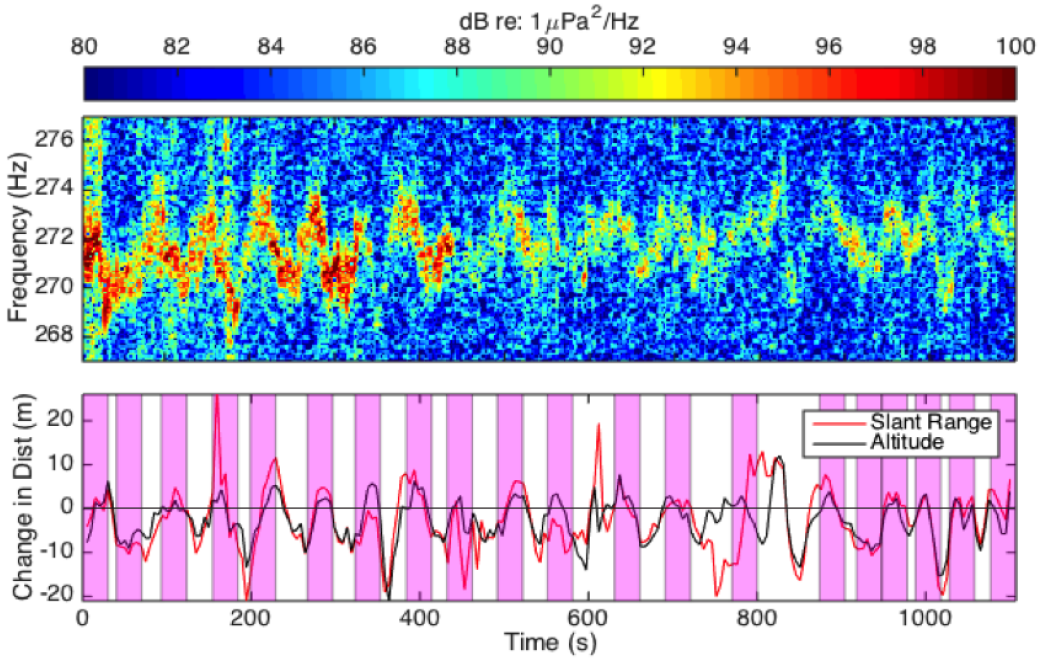

Figure 4.22: Spectrogram (top) of the shallow water experiment time series during the altitude hovers from 31 to 610 meters, centered around the 272 Hz harmonic of the engine and main rotor. The lower graph shows each altitude hover of 30 seconds as vertical magenta strips, with the GPS altitude change in black (change in GPS altitude data from value to value), and the slant range change, which is the linear distance between the helicopter and the housing unit of the array, in red.

The frequencies of the harmonics produced by the R44 Robinson helicopter fluctuated slightly during flight ($< 6\,Hz$) due to the flight dynamics of the helicopter. The spectral lines around $272\,Hz$ in Figure 4.22 show a constant shifting of frequency throughout the experiment, with the bottom plot showing the twenty hovers shaded with magenta. The slant range displayed is the absolute distance between the helicopter and the underwater sensor. The GPS unit recorded data at $0.1\,Hz$ during this experiment. The "Change in Dist (m)" of the y-axis is the physical change in meters between each GPS data point from the helicopter.

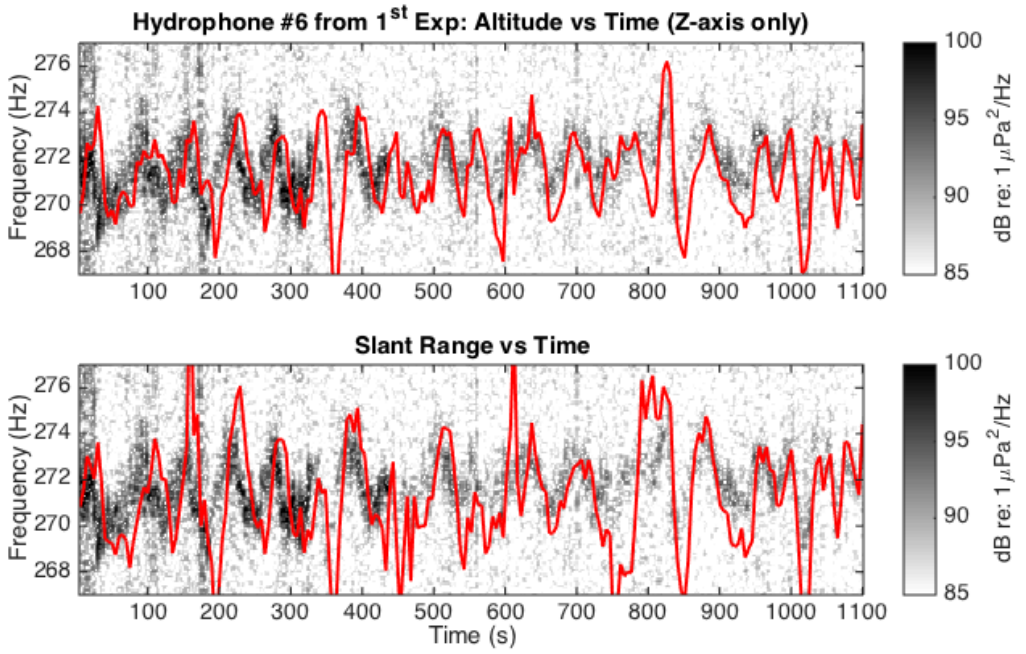

Figure 4.23: Spectrograms of complete time series, from the first hover to last, overlaid with the change in GPS altitude (top) and change in slant range (bottom). Fluctuations in the frequency of the helicopter's harmonic correlate with the small excursions with the nominal altitude.

Small fixed-wing aircraft typically operate with propeller blades of a fixed pitch and increase or decrease their lift by changing the propellers RPM, or the physical characterizes of the wings (i.e. flaps). Helicopters differ as their rotors maintain a relatively fixed RPM, increasing or decreasing their lift by changing the pitch of the main rotor blades. Maintaining a constant position during a hover requires continuous adjustment of the helicopters controls to counter changing wind velocity, direction, and density fluctuations.

A shown in Figure 4.23 the frequency-shift displayed in the $272\,Hz$ harmonic is more consistent with changes in the helicopters altitude, and not the linear distance between the helicopter and the receiver. Changes in the pitch of the main rotor blades, to increase or reduce lift, also change the drag characteristics on the main rotor. This increase in drag on a main rotor blades is compensated with a slight increase in the engines RPM. As the rotors are coupled to the

engine this also increases the main rotor and tail rotor RPM's. By Equations 2.2 and 2.3 this also changes the harmonic frequencies of all three. Whereas a decrease in lift reduces the drag on the main rotor and subsequently reducing the RPM causing the harmonics to shift lower in frequency.

4.4 Head Wave Generation with the Helicopter End-Fire to the Array

The primary purpose of this experiment was to investigate the underwater sound signature of an air-borne helicopter with two over-fights and several hover altitudes over the sensor station. Before, between, and after these fight operations the helicopter moved around the sensor station at low altitude in order to position itself for each operation. This provided opportunities to analyze the underwater sound signature with the helicopter at different positions relative to the array. One position of particular interest was as with the helicopter at end-fire relative to the HLA at low altitude and velocity. This end-fire section of the flight path is shown in Figure 4.24, highlighted in red. As the helicopter passed beyond end-fire the fight path is shown in pink.

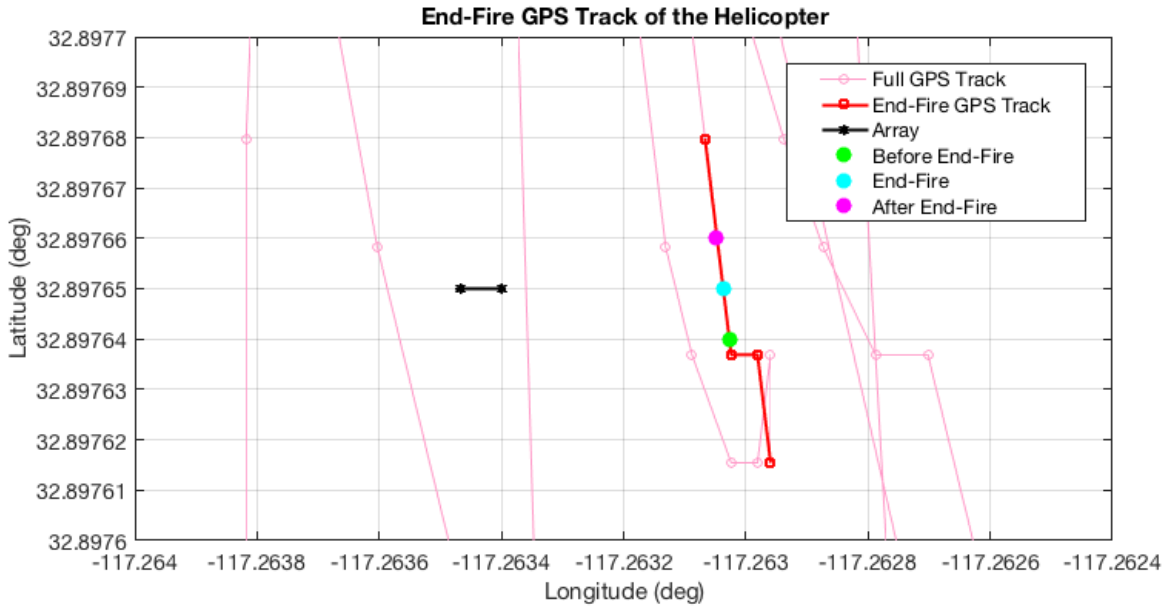

Figure 4.24: GPS data of the helicopter flight path during the experiment (pink track) and the helicopter low-altitude flight path as it passes through the end-fire (red track) relative to the HLA (black). Also shown are the positions of the R44 helicopter for the acoustical data used to produce the real coherence functions, with corresponding color, shown in Figure 4.25.

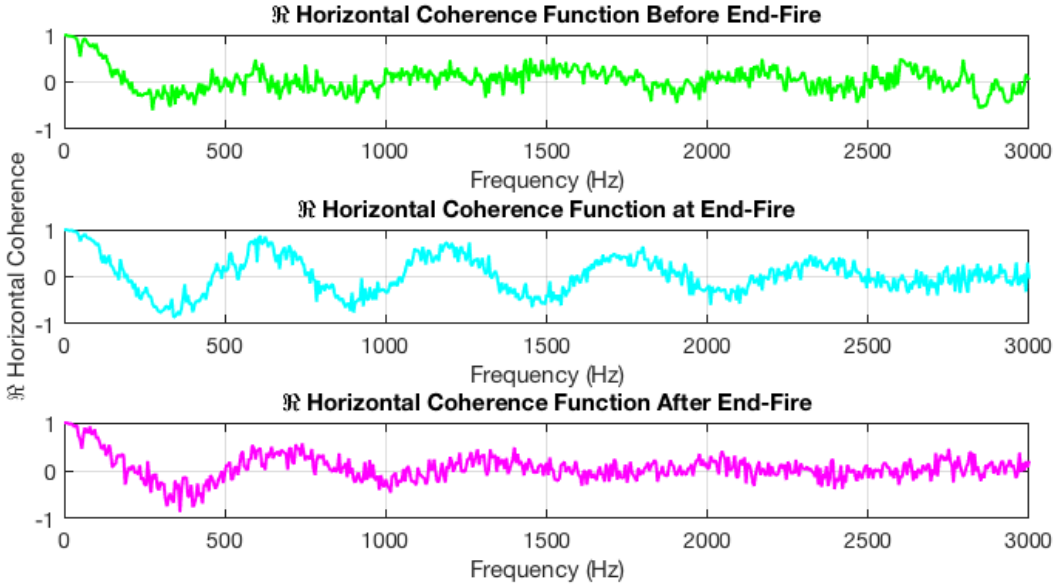

Figure 4.25: The real part of the horizontal coherence function from the experiment data as the passed through the end-fire position relative to the HLA. The top plot is as the helicopter average position is at the green dot Figure 4.24. The middle plot shows as the helicopter passes through the end-fire orientation, shown by a Cyan Dot in Figure 4.24. The lower plot is taken as the helicopter is at the magenta dot in Figure 4.24.

In analyzing the data, the real part of the horizontal coherence function was formed from the acoustic pressure recorded on two underwater sensors located $2.97\,m$ apart. When the Robinson R44 helicopter was not at the end-fire position relative to the array, the real coherence function was found to be relatively flat in frequency after the initial drop from the value of 1. As the helicopter approaches the end-fire position, the coherence function becomes more sinusoidal with an increase in zero crossings throughout the bandwidth produced by the helicopter, reaching a pinnacle when the helicopter is at the end-fire position relative to the array. This prompted the development of the theory, previously presented in Chapter 3, for the coherence function of the head wave. This progression of the helicopter through the end-fire position can be seen in Figure 4.25, which shows the real part of the coherence function with the helicopter approaching the end-fire position, at end-fire position, and as the helicopter departs end-fire position.

The top plot of Figure 4.25 shows a downward slopping function at low frequencies, which after $\sim 200\ Hz$ fluctuates around zero with a noisy progression to higher frequencies. This plot corresponds to the helicopter approaching the end-fire position in the location of the green dot in Figure 4.24. The middle plot corresponds to the helicopter in the end-fire position relative to the array (cyan dot in Figure 4.24). This middle plot of the real coherence function shows a strong sinusoidal signal with several zero crossings within the bandwidth of sound the R44 helicopter produces ($13\ Hz - 2.5\ kHz$), which represents, at least in portion, the head wave. The third plot is after the helicopter has passed through the end-fire position, corresponding to the magenta dot in Figure 4.24. Here we see a flatter coherence function, above $\sim 200\ Hz$, with only a couple zero crossings that have spread in frequency relative to the end-fire position.

This progression of the horizontal coherence function as the helicopter passes the end-fire position relative to the array was determined to be a viable pursuit in creating an inversion

technique to recover the sediment sound speed. The strong sinusoidal signal with several zero crossings would not only provide an estimate of the sediment sound speed across the frequency bandwidth, but also provide the ability to estimate the sediment sound speed at each zero crossing's frequency. As shown in Chapter 3, a sound source, at end-fire to a HLA, produces a head wave horizontal coherence function that depends only on the sound speed within the sediment and the separation between the sensor pair. Utilizing the frequencies produced by a helicopter and a larger sensor separation, the sediment sound speed could be estimated at frequencies as low as $13\,Hz$. In Chapter 5 a second experiment will be presented which was designed and conducted to detect the head wave excited by the R44 Robinson helicopter at low-altitude, while approaching an underwater HLA in the end-fire position.

4.5 Summary

This chapter looked at the acoustic measurements from the initial experiment, performed on the 6th of April 2015, utilizing an air-borne Robinson R44 helicopter to examine its potential as a sound source in robust inversion methods in shallow-water marine environments. It was found that the acoustic signature of the Robinson R44 helicopter could readily be detected at usable levels by underwater sensors $0.5\,m$ above the seabed in shallow water of a depth of $16.5\,m$.

Two fight operations were performed to investigate the transmission of helicopter sound into the water column. Two fly-overs were performed at a low altitude of $30.5\,m$ above the shallow-water sensor station that showed the Doppler shift of the harmonics produced by the helicopter were detectable. This characteristic Doppler shift has been used in the pass with fixed-wing aircraft to determine the sediment sound speed and atenuation[4]. Beginning at $30.5\,m$ and

incrementing by $30.5\,m$ to a maximum altitude of $610.0\,m$ the underwater intensity of the helicopter sound signature was investigated at twenty altitudes above the sensor station. The underwater sound signature of the helicopter was detectable at useable levels, $> 5\,dB$ above the ambient noise at all altitudes. It was also found that the stronger harmonics peaks produced by the Robinson R44 helicopter where detectable on the underwater receivers when at high altitudes when it was not detected on the surface microphone. The underwater intensity of the helicopter's sound signature was found to be consistent with the shallow-water analytical model derived in Chapter 3.

During the planned flight operations of this experiment, the helicopter maneuvered around the sensor station for proper positioning. This provided valuable data of the helicopter passing through the end-fire position relative to the underwater HLA. The horizontal coherence function was formed from two of the underwater sensors when the helicopter was at end-fire. This was found to show a strong sinusoidal signal with several zero crossings throughout the helicopter bandwidth. The head wave coherence function was derived from the shallow-water analytical model, Chapter 3, and found to show this sinusoidal signal. Apart from frequency, the head wave coherence function depends on only the sediment sound speed and the separation of the two sensors. A second experiment was designed and performed to investigate the detection of the head wave produced by a Robinson R44 helicopter at end-fire to an HLA. This second experiment and subsequent inversion method is presented in the next chapter, Chapter 5, which determined the sediment sound speed to be $1682.42 \pm 16.20\ m/s$, which is consistent with the very fine sediment at the experiment site.

Chapters 4, in part, is a reprint of the material as it appears in the Journal of the Acoustical Society of America: D. A. Bevans, M. J. Buckingham, “Estimating the Sound Speed of a Shallow-water Marine Sediment from the Head Wave Excited by a Low-flying Helicopter”, 142: 2273 (2017). The dissertation author was the primary investigator and author of this manuscript, and Dr. Michael J. Buckingham directed and supervised the research.

References

1. L. J. Hogarth, J. Babcock, N. W. Driscoll, et al.,"Long-term tectonic control on Holocene shelf sedimentation offshore La Jolla, California", Geology **35** (3), 275-278 (2007).

2. M. J. Buckingham, E. M. Giddens, J. B. Pompa, et al., in *Proceedings of the Sixth European Conference on Underwater Acoustics*, edited by A. Stepnowski (Gdansk University of Technology, Gdansk, 2002), pp. 465-470.

3. C.-T. Chen and F. J. Millero,"Speed of sound in seawater at high pressures", J. Acoust. Soc. Am. **62** (5), 1129-1135 (1977).

4. E. M. Giddens and B. M. J.,"Geoacoustic inversions in shallow water using Doppler-shifted modes from a moving source", J. Acoust. Soc. Am. **116** (4, Pt. 2), 2557 (2004).

5. A. B. Wood, *A Textbook of Sound*, Third ed. (G. Bell and Sons Ltd., London, 1964).

6. H. H. Hubbard, (American Institute of Physics, New York, 1995), Vol. **1**, pp. 426.

7. F. B. Jensen, W. A. Kuperman, M. B. Porter, et al., *Computational Ocean Acoustics*. (American Institute of Physics, New York, 1994).

8. M. S. Weinstein and A. G. Henney,"Wave solution for air-to-water sound transmission", J. Acoust. Soc. Am. **37** (5), 899-901 (1965).

9. H. Medwin and J. D. Hagy Jr.,"Helmholtz-Kirchhoff theory of sound transmission through a statistically rough plane interface between dissimilar fluids", J. Acoust. Soc. Am. **51** (No. 3, Part 2), 1083-1090 (1972).

10. A. A. Hudimac,"Ray theory solution for the sound intensity in water due to a point source above it", J. Acoust. Soc. Am. **29** (8), 916-917 (1957).

11. R. J. Urick,"Noise signature of an aircraft in level flight over a hydrophone in the sea", J. Acoust. Soc. Am. **52** (No. 3, Pt. 2), 993-999 (1972).

12. R. W. Young,"Sound pressure in water from a source in air and vice versa", J. Acoust. Soc. Am. **53** (6), 1708-1716 (1973).

13. J. F. Waters,"Computer Programs for Underwater Sound Fields Due to Airborne Sources", (1972).

14. D. M. F. Chapman and P. D. Ward,"The normal-mode theory of air-to-water sound transmission in the ocean", J. Acoust. Soc. Am. **87** (2), 601-618 (1990).

15. W. J. Richardson, C. R. Greene Jr., C. I. Malme, et al., *Marine Mammals and Noise*. (Academic Press, New York, 1995).

Chapter 5

Estimating the Sound Speed of a Shallow-Water Marine Sediment from the Head Wave Excited by a Low-Flying Helicopter Experiment

5.1 Introduction

In this chapter this second experiment performed on the 14th of December 2016, will be discussed in detail including experiment setup, equipment, and the horizontal coherence function measured by the underwater sensors to demonstrate the inversion technique detailed in Chapter 3. Much of the experiment setup and equipment (Figure 4.1) is the same as the initial helicopter experiment discussed in Chapter 4. The helicopter, acting as an acoustic source, performed a series of low-level maneuvers with hovers while maintaining an end-fire position to the array. From the data collected during this experiment the two-point horizontal coherence function of the head wave was calculated and the inversion technique applied. By matching the zero crossings of the measured and theoretical horizontal coherence functions, the sound speed of the sediment was recovered and found to be $1682.42 \pm 16.20\ m/s$. This sound speed is consistent with the grain size and sediment type at the site. In addition, the measured horizontal coherence was found to be in agreement with the FFP wave-number computer model SCOOTER.

5.2 The Robinson R44 Helicopter Head Wave Experiment

Figure 5.1: The Robinson R44 helicopter hovering above the sensor station at end-fire to the array during the head-wave experiment.

To demonstrate the head-wave inversion technique, an experiment was conducted in shallow water, 16.5 m deep, about 2 km off the coast of Del Mar, southern California, in which a Robinson R44 helicopter (Figure 5.1) hovering at low level acted as an airborne sound source. During the experiment the helicopter, at a low altitude, maintained an end-fire position to the underwater HLA while it approached slowly from the south. A Sea-Bird temperature-depth probe was deployed several times during the course of the experiment to determine the sound speed profile in the channel. From the data of these hover operations the sound speed of the marine sediment was determined through comparison with the theory of the head wave coherence function. The sound speed was found to be consistent with an earlier Vibracore survey of the area by Scripps scientists[1], the seabed at the experiment site is known to consist of a layer,

about 10 m thick, of fine-grained to very-fine-grained, olive-green, homogeneous sand.

Figure 5.2: The research vessel Saikhon during the head-wave experiment.

Operating from a small support research vessel, the Saikhon (Figure 5.2), divers deployed the FlyBy array, at a depth of 16 m (i.e., 0.5m above the seabed). A detailed schematic of the experimental setup and equipment is given in Figure 4.2. The HLA, known as the FlyBy array, was stretched between two sand anchors and aligned on a bearing of 340°, roughly parallel to the coastline, with the southern end of the array located at 32^{o} 53.859^{o} N, 117^{o} 15.808^{o} W. South of the HLA a third sand screw was installed and a mooring line attached. This line was used to

secure the surface unit, Figure 4.5, after the HLA installation. The DAQ system was updated for this experiment with a silent solid-state hard drive and a faster embedded controller (PXI-8101). Otherwise, the DAQ and battery system remained the same as detailed in Section 4.2. Once the underwater potion of the setup was complete the DAQ system was powered on to begin the automated collection of data. Once confirmed to be recording the acoustic data, the surface unit was released on the mooring line. With the completion of the sensor station, two marker buoys were deployed in the water south of the array. These buoys were positioned in-line with the array at the distances of $25\ m$ and $50\ m$ for the southern end of the array. The helicopter pilot used these buoys as visual aids during his approach positioned at end-fire relative to the array. Once the buoys were deployed, the support vessel anchored several hundred meters to the west of the sensor station.

The hydrophones have an omnidirectional response (Figure 4.3) and flat frequency response (Figure 4.4) from 3 Hz to 20 kHz with built-in low noise 20 dB pre-amps. A microphone (ITC 6050C) calibrated in air ($5.3 \times 10^{-8}\ \mu Pa/V$) was mounted to the surface unit and positioned $1\ m$ above the sea surface to record the air-borne acoustic signature. The DAQ collected the microphone and hydrophone data with all the channels time synchronized at a rate of $102.4\ Hz$. A schematic of the experimental arrangement (not to scale), with the R44 helicopter in a hover, end-fire to the FlyBy array, is shown in Figure 5.3, along with the sound speed profile in the channel, which was computed using the Chen and Millero[2] algorithm with the SeaBird temperature-depth data and an assumed salinity of 34‰.

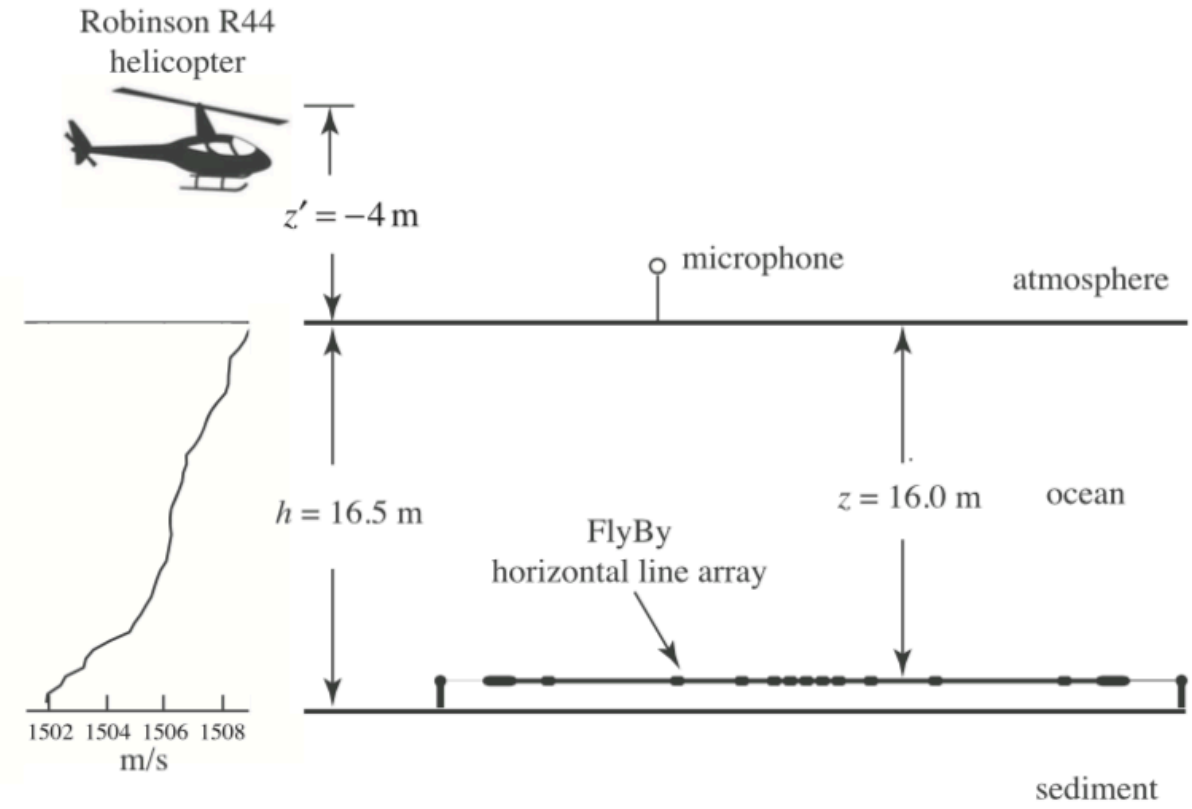

Figure 5.3: Schematic (not to scale) of the shallow-water head-wave experiment in which as R44 helicopter acted as an airborne sound source located in an end-fire position relative to the 11-element FlyBy horizontal line array. The sound speed profile in the channel, as derived from the SeaBird temperature-depth data, is shown on the left.

On board the Robinson R44 helicopter was an Adafruit altitude-encoding GPS, giving height above the geoid, and, as back up, a Garmin 396 GPS with barometric altitude encoding. Attached to the floating DAQ battery housing was an additional Adafruit altitude-encoding GPS, which provided the elevation of the sea surface relative to the geoid and the location of the in-air microphone, from which the true altitude of the R44 helicopter above the sea surface was inferred, although, as mentioned earlier, the altitude of the helicopter is not actually needed in the inversion for the sediment sound speed. An Adafruit altitude-encoding GPS unit was also on board the support vessel in order to track its movements during the experiment. An internally

mounted GoPro video camera monitored the instrument panel throughout the helicopter flight.

Although a different Robinson R44 helicopter was used in this experiment it was also operated out of Montgomery-Gibbs Executive Airport in San Diego, CA. On completion of the sensor station and secure anchoring of the R/V Saikhon, the R44 helicopter lifted off to begin its flight operations. The R44 performed a series of low-level maneuvers around the experiment site, including flights at cruise speed ($\approx 90\ kn$) normal to and along the track of the FlyBy array at an altitude of $10\ m$ or less. With the main rotor at an altitude of $4\ m$, half a dozen $30 - s$ hovers were performed, end-fire to the FlyBy array, at horizontal ranges between 0 and $300\ m$ from the array center, as shown in the GPS track in Figure 5.4. The purpose of the hovers was to excite the head wave at the seabed, with a view to performing an inversion for the sediment sound speed using the expression for the horizontal coherence in Equation 4.69. The complete in-flight time of the helicopter during these operations was roughly $30\ min$.

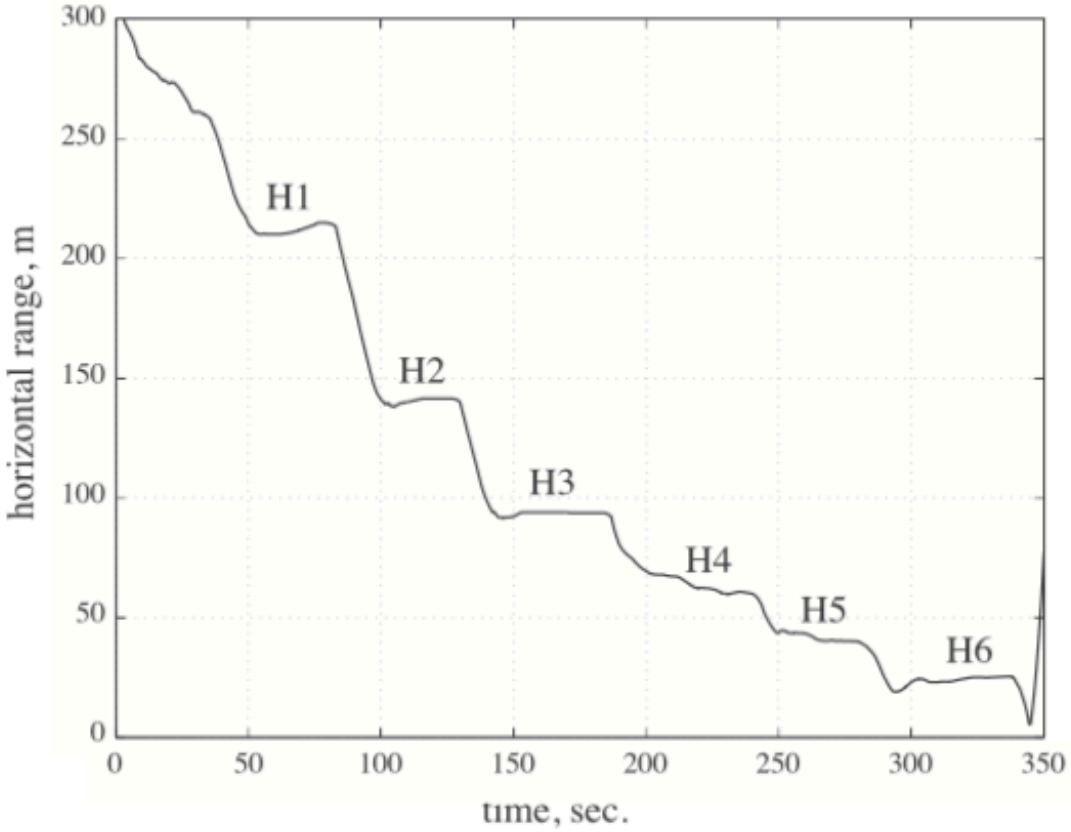

Figure 5.4: GPS end-fire range of the R44 helicopter from the mid point of the FlyBy hydrophone array. Hovering periods are labeled H1, H2, …, H6. The head wave was detected during the H5 hover at a range of approximately 35 m.

5.3 Sediment Sound Speed from the Head-Wave

A horizontal range window (Figure 5.5) exists within which the head wave is discernible at the sensor station. If the source (the R44 helicopter in the present case) is too far away from the receiver, the head-wave pressure field, because of its rapid $1/r^2$ geometrical spreading (Equation 3.65), will be too weak to detect against the normal-mode background field. On the other hand, if the source is too close to the receiver, the range will not be sufficient for the head wave to become established at the sensor station. The minimum horizontal range, r_{min}, necessary for the head wave to exist at the receiver is illustrated by the simple ray geometry in

Figure 2.3. Under the experimental conditions described above, with the main rotor of the R44 helicopter at an altitude of $4\ m$, the minimum source-to-receiver range needed for head-wave excitation is $r_{min} \approx 33\ m$.

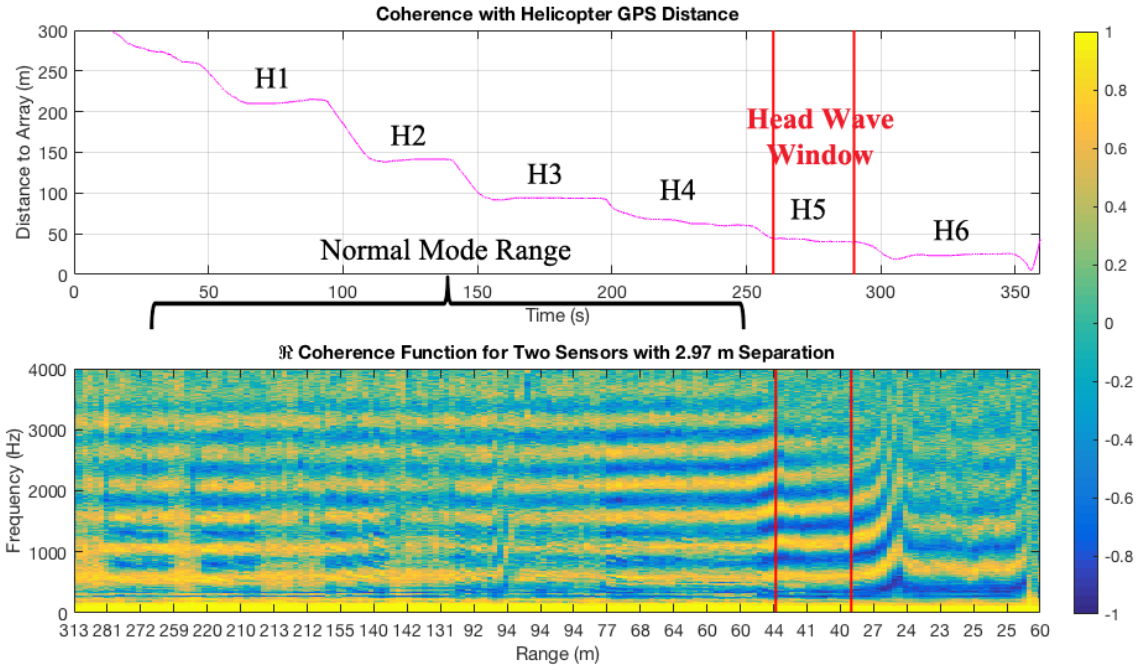

Figure 5.5: The GPS hover data with helicopter range and time presented again lined up with a waterfall plot of the real coherence function from the data with helicopter range. The normal mode region with range is shown by bracket and the head wave window is marked with red lines in both. The strength of the coherence function is strongest in the bandwidth of the sound produced by the helicopter in this window and there is a noticeable change when the helicopter is in the head wave range relative to the sensors.

The underwater acoustic signature of the R44 helicopter, whilst hovering in the end-fire position at various horizontal ranges, was recorded on the hydrophones of the FlyBy array. From these pressure time series, the horizontal coherence function was formed between pairs of sensors in the array. An example of the real and imaginary parts of the measured coherence

function, for a horizontal range of approximately 40 m from the R44 to the mid point of a pair of FlyBy sensors, 2.97 m apart, is shown in Figure 5.6. (A greater sensor separation would have been preferable but this was not possible due to a poor signal-to-noise ratio on several of the FlyBy hydrophones.)

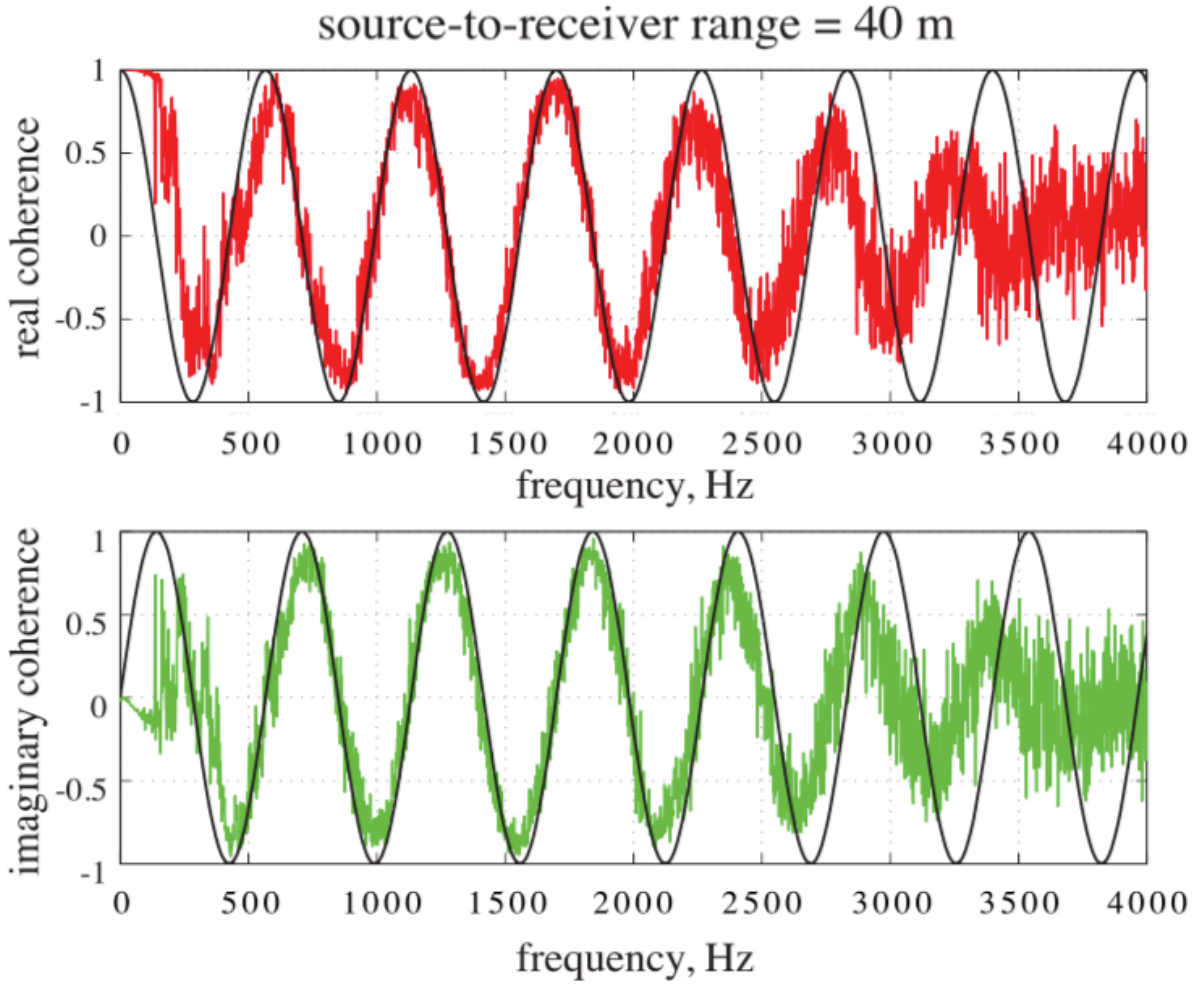

Figure 5.6: Real and imaginary parts of the horizontal coherence function versus frequency from two horizontally aligned hydrophones separated by 2.97 m. The jagged curves represent data taken with the R44 helicopter at a horizontal range of 40 m from the mid-point between the two sensors. In this end-fire position, the helicopter is within the range window where the head wave is an established component of the acoustic field. The value of the sediment sound speed used in plotting the theoretical expression in Equation 3.69, shown as the solid smooth curves, is $c_3 = 1682.42\ m/s$.

In this position, the helicopter was within the head-wave range window. Both the real and imaginary parts of the coherence function exhibit well-defined sinusoidal oscillations over the frequency band of the helicopter sound, which, as shown by the power spectrum in Figure 2.1, extends to about $2.5\ kHz$. These sinusoidal oscillations, with the real and imaginary parts accurately in quadrature, are consistent with the theoretical expression for the coherence function of the head wave in Equation 3.69. Beyond the $2.5\ kHz$ bandwidth of the helicopter sound, ambient noise becomes predominant and the sinusoidal character of the coherence function is eroded accordingly.

In Figure 5.6, the solid smooth curves represent the theoretical expression for the horizontal coherence function of the head wave in Equation 3.69, evaluated with $R = |r_1 - r_2| = 2.97\ m$ and the sound speed in the sediment set to $c_3 = 1682.42\ m/s$. This estimated value for the sediment sound speed is consistent with the known sediment type[1, 3] at the experiment site, a fine to very-fine sand. It corresponds to a sound speed ratio of 1.12 when the bottom-water sound speed is $1502\ m/s$, as was the case in this experiment (see Figure 5.3).

To obtain the above value of c_3 from the data, the zeros in the real and imaginary parts of the coherence function data were matched to those in the theoretical expression in Equation 3.70 The nth zero, $f(n)$, occurs when the argument of the cosine and sine functions in Equation 3.70 is equal to $n\pi/2$, with odd and even values of n, respectively, corresponding to the zeros in the real and imaginary parts of the coherence function. Thus, the value of c_3 estimated from the nth zero is given by Equation 3.70. A simple technique was used to recover the zeros, $f(n)$, from the data, which relies on finding the minima in the magnitude of the real and imaginary parts of the experimentally determined coherence function. These minima, which are readily obtained from

an m-file in MATLAB, correspond precisely to the required zeros in the real and imaginary coherence data. Table 5.1 lists the zeros in the coherence function data, as returned by this procedure, along with the corresponding values of the sediment sound speed calculated from Equation 3.70. Only zeros 6 to 14 were used in the computation, since they fall within the frequency band where the helicopter-generated head wave is the dominant component of the coherence function data. The estimated value of the sediment sound speed, used in computing the solid smooth curve in Figure 5.6, is the mean of the values in Table 5.1, with the error in the estimate given by the standard deviation: $c_3 = 1682.42 \pm 16.20\ m/s$.

Table 5.1: Estimated zeros, $f(n)$, in the measured coherence curves and the corresponding sediment sound speed computed from Equation 3.70.

n	$f(n)$ (Hz)	$c_3(n)$ (m/s)
6	842.2	1667.5
7	1003.1	1702.4
8	1146.9	1703.1
9	1285.9	1697.4
10	1395.3	1657.6
11	1545.3	1668.9
12	1703.1	1686.1
13	1850.0	1690.6
14	1965.6	1668.0

As can be seen in Figure 5.6, over the bandwidth of the R44 helicopter acoustic signature, the theoretical curves for the real and imaginary parts of the head-wave coherence are very well

matched to the R44 coherence data. From this agreement between theory and experiment, it may be inferred, not only that the sound from a light helicopter can excite the head wave in a shallow-water channel, but also that the helicopter-generated head wave can be used as the basis of an inversion technique for recovering the sound speed in the sediment.

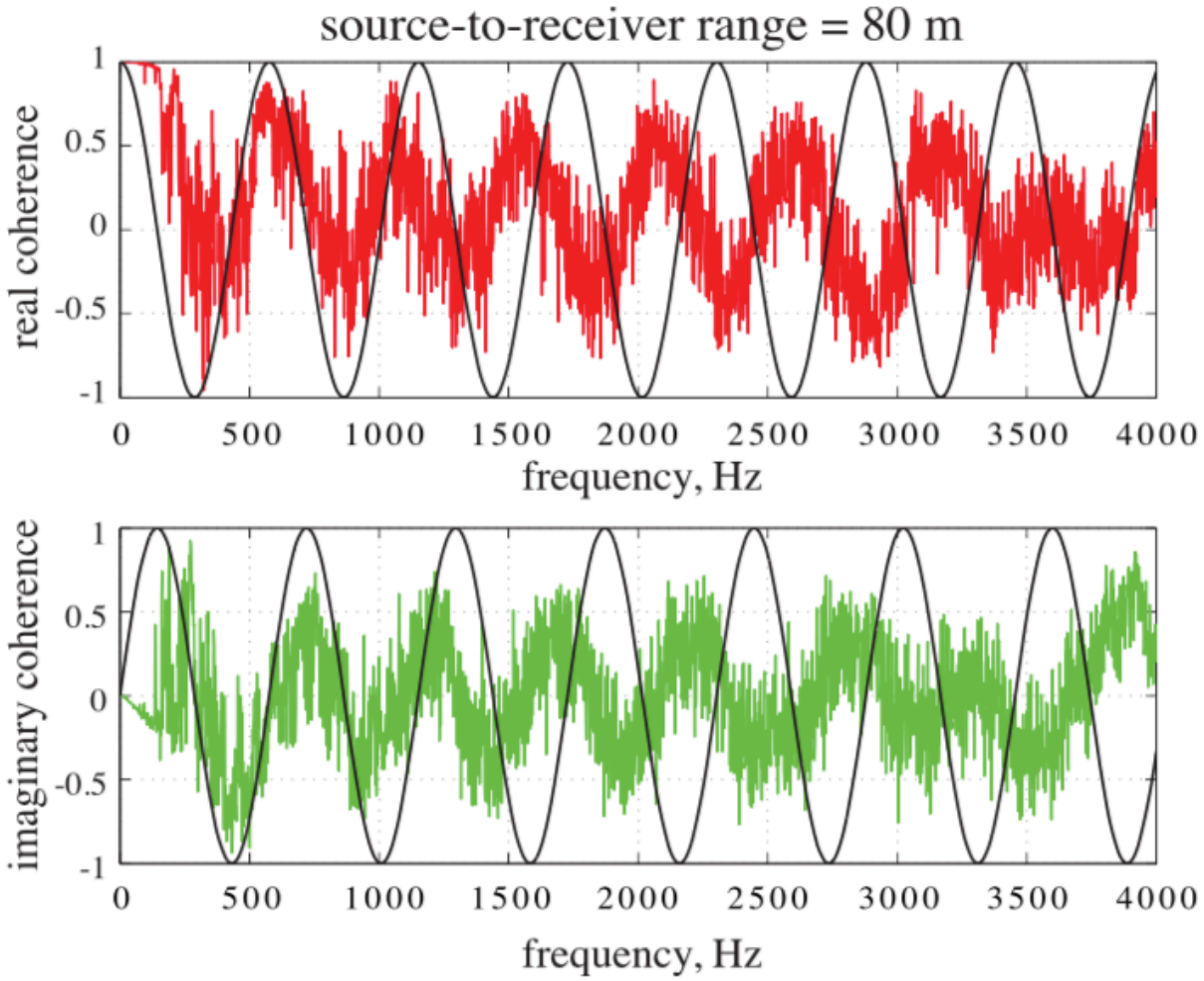

Figure 5.7: Real and imaginary parts of the horizontal coherence function versus frequency from two horizontally aligned hydrophones separated by 2.97 m. The jagged curves represent data taken with the R44 helicopter at a horizontal range of 80 m from the mid-point between the two sensors with all else the same as in Figure 5.6, including the solid, smooth theoretical curves representing the head wave. At this (relatively long) range, the head wave, although established at the sensors, is too weak to be detected. The measured coherence function is dominated by normal modes, which exhibit intermodal interference, manifested as non-uniformly distributed zero crossing in the noisy coherence data.

If this conclusion is to hold up, then, in the absence of the head wave, the theoretical head-wave coherence curves in Figure 5.6 should not match the data. To check that this is so, the horizontal coherence with the helicopter outside the head-wave range window must be examined. Figures 5.5 and 5.6 show the horizontal coherence data with the R44 at a "long" range of 80m and a "short" range of 10m, respectively, with all else the same as in Figure 5.6, including the theoretical curves. At both ranges, the head wave is negligible or absent, and it is evident that the theoretical head-wave curves do not in fact align with the data. To be specific, the zero crossings of the non-head-wave data and the head-wave theoretical curves in Figures 5.5 and 5.6 are heavily mismatched, in stark contrast to the agreement between the head-wave theory and head-wave data seen in Figure 5.6.

At the longer range of 80 m, the head wave, due to its high geometrical spreading, is negligible and the normal modes dominate the underwater sound field generated by the helicopter. Even so, the modal field is quite weak, as can be seen in Figure 5.7, where the coherence is much noisier than in the head wave case in Figure 5.6. There are vestiges of sinusoidal behavior in Figure 5.7 but the zero crossings are not uniformly distributed, unlike their counterparts in Figure 5.6 that are associated with the head wave. The irregularity of the zero crossings in Figure 5.7 arises mainly from inter-modal interference, which also makes the coherence function in this "long range" regime very sensitive to small, incremental changes in the helicopter range.

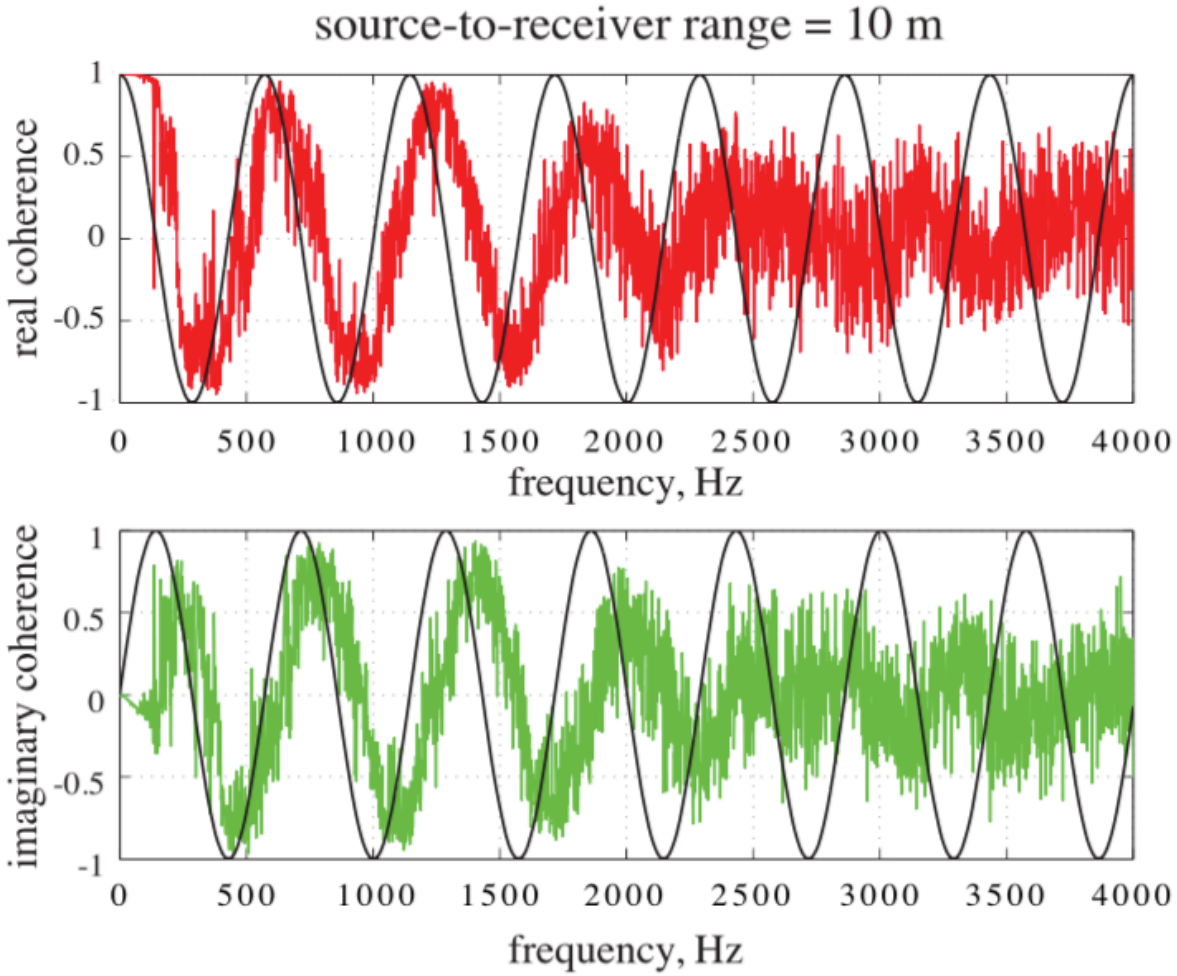

Figure 5.8: Real and imaginary parts of the horizontal coherence function versus frequency from two horizontally aligned hydrophones separated by 2.97 m. The jagged curves represent data taken with the R44 helicopter at a horizontal range of 10 m from the mid-point between the two sensors with all else the same as in Figure 5.6, including the solid, smooth theoretical curves representing the head wave. At this (relatively short) range, less than r_{min}, the head wave is not established at the receivers. The underwater sound field is dominated by the direct (i.e., surface-refracted) and bottom-reflected arrivals, which, being steeper than the critical grazing angle of the head wave, give rise to zero crossings in the coherence data that are higher than those in the curves from the head wave theory.

At the shorter range of 10 m, the head wave is not established at the sensor station. Nevertheless, as illustrated in Figure 5.8, the experimental coherence curves retain their sinusoidal character, exhibiting zero crossings that are uniformly spaced but with higher values than their head-wave counterparts in Figure 5.6. Such behavior, with the helicopter almost

overhead, is consistent with an underwater sound field that is dominated by the direct (i.e., surface-refracted) and bottom- reflected arrivals, whose grazing angle is steeper than the critical grazing angle of the head wave. A steeper grazing angle translates into a higher phase speed, and a higher phase speed gives rise to higher zero crossings in the coherence function, exactly as exhibited by the data in Figure 5.8.

Based on the horizontal coherence curves in Figures 5.4, 5.5, and 5.6, it is reasonable to conclude that the head wave generated by the R44 helicopter is detectable within a source-range window bounded by simple ray geometry at the low end and a rapid, $1/r^2$, geometrical decay at the high end. As demonstrated above, with the source in the head-wave range window, an inversion can indeed be performed to recover the sound speed in the sediment.

5.4 Numerical Simulation of the R44-Generated Sound Field

The expression in Equation 3.69 for the horizontal coherence of the head wave is an approximation that is valid only when the source is within the head-wave range window. For a more general representation of the horizontal coherence that holds for all ranges of the source helicopter, from overhead, throughout the head-wave range window and beyond into the normal mode region, it is convenient to turn to numerical modeling. The aim of the exercise is to consolidate the conclusions reached above concerning the extraction of the sediment sound speed from the head wave.

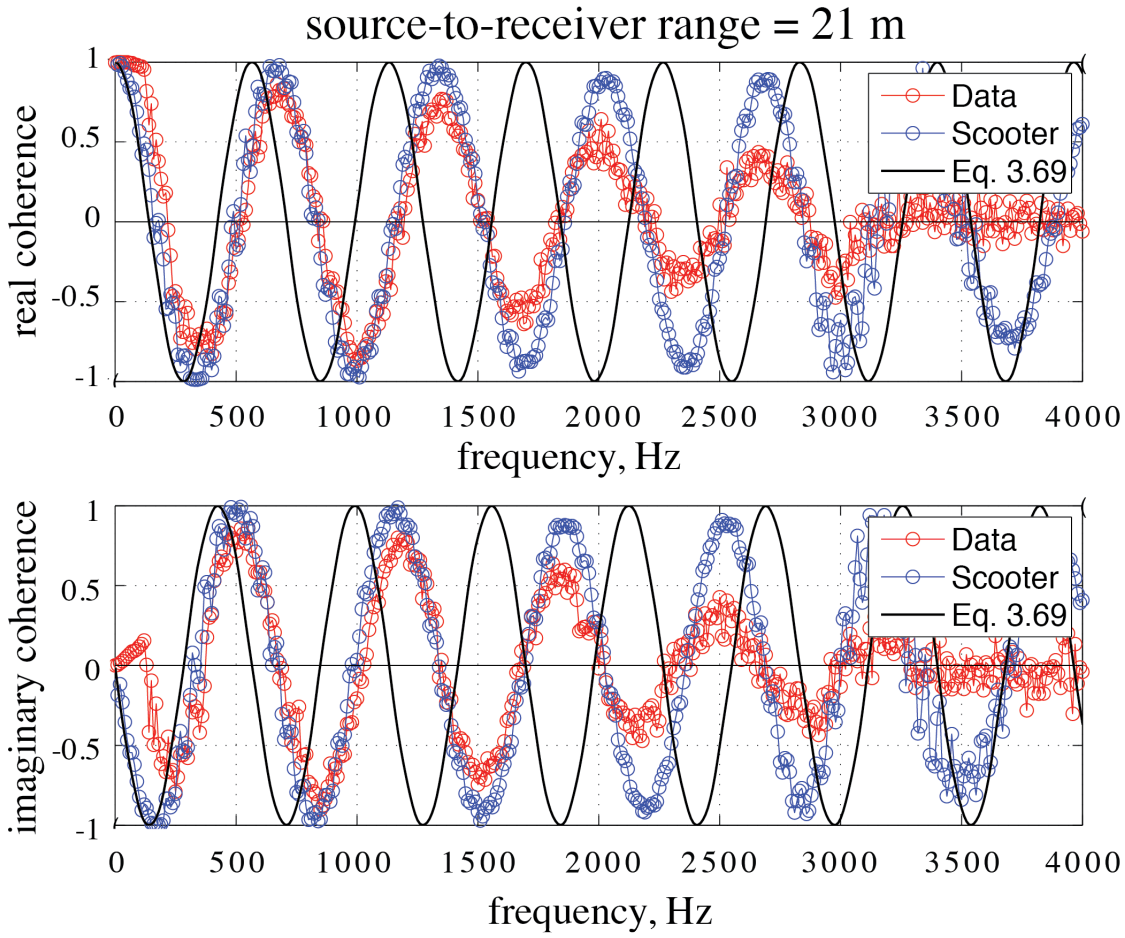

Figure 5.9: Real and imaginary parts of the coherence function versus frequency from two horizontally aligned hydrophones separated by 2.97 m. The red curves represent experimental data, the blue curves were computed using Scooter, and the black curves are from the analytical head-wave expression in Equation 3.69. The sediment sound speed used in evaluating Scooter and Equation 3.69 is $c_3 = 1682.42\ m/s$. The horizontal ranges between the source and the mean position of the two sensors is 21 m, too close for the head wave to be established.

Scooter[4] is a fast field program (FFP), based on a wave-number integral, that computes the (complex) acoustic pressure field in a horizontally stratified, multi-layer waveguide. Although the normal modes, the head wave, and the various ray arrivals at short ranges are not separated out in the FFP formulation, they are all accounted for in the wavenumber integral. Using Scooter, the acoustic pressure field in the three-layer waveguide illustrated in Figure 3.3 was computed for all points in the water column. The coherence function, as defined in Equation

3.68, was then constructed from the computed pressure at two horizontally aligned points, 2.97 m apart and 0.5 m above the seabed, corresponding to the experimental configuration considered earlier. The main rotor of the helicopter was represented as a compact source at a height of 4 m above the sea surface and the sound speed in the water column was set at 1502 m/s, consistent with the bottom-water sound speed measured in the experiment. The sound speed in the sediment was taken to be $c_3 = 1682.42\ m/s$, that is to say, the value estimated from the zero crossings of the head-wave coherence curves in Figure 5.6.

For three source-to-receiver ranges, Figures 5.9, 5.10, and 5.11 show the frequency dependence of the horizontal coherence data and, for comparison, the corresponding computations from the Scooter simulation. Also included in each figure, for reference, is the analytical head-wave expression in Equation 3.69 At each of the source ranges shown in the figures, and indeed at all ranges between 10 and 80 m, the computed coherence from Scooter is very well matched to the experimental coherence data, particularly the zero crossings, over the frequency bandwidth of the source.

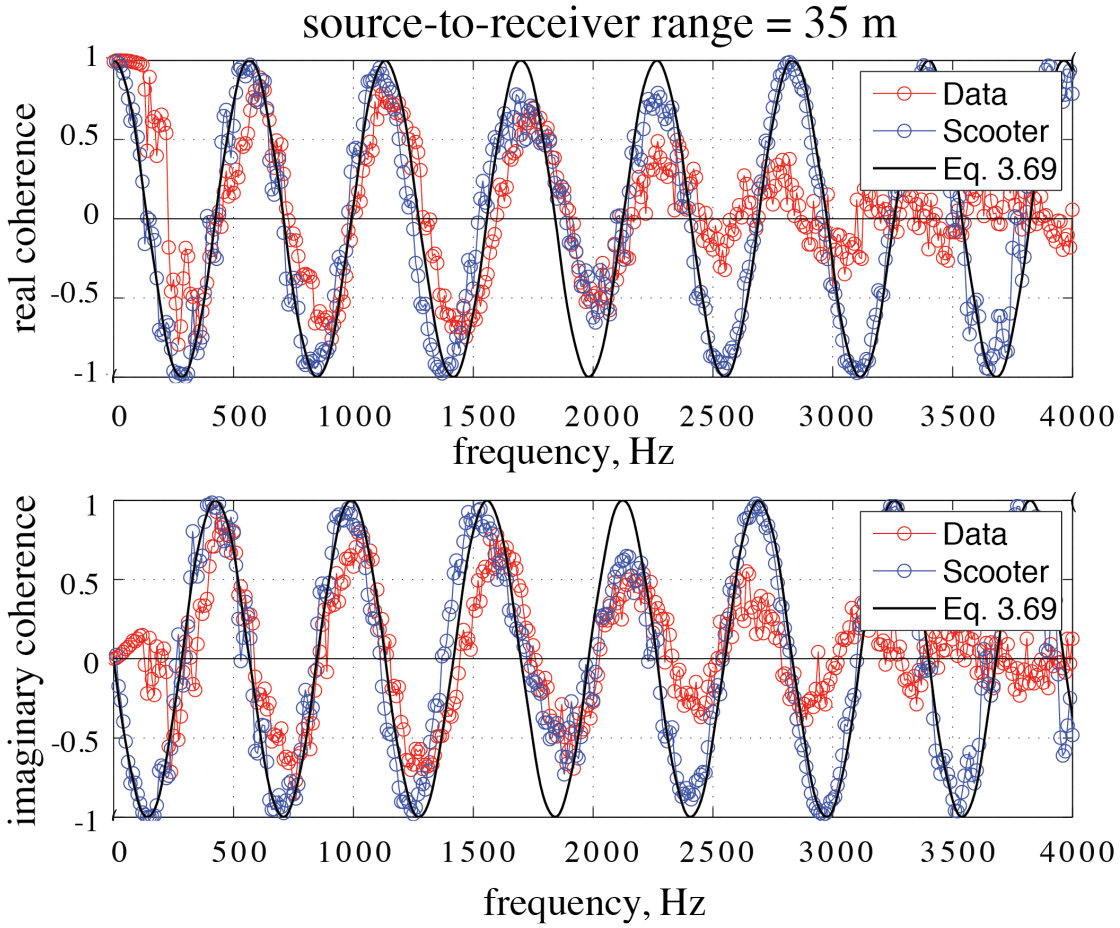

Figure 5.10: Real and imaginary parts of the coherence function versus frequency from two horizontally aligned hydrophones separated by 2.97 m. The red curves represent experimental data, the blue curves were computed using Scooter, and the black curves are from the analytical head-wave expression in Equation 3.69. The sediment sound speed used in evaluating Scooter and Equation 3.69 is $c_3 = 1682.42\ m/s$. The horizontal ranges between the source and the mean position of the two sensors is 35 m, within the head wave range window.

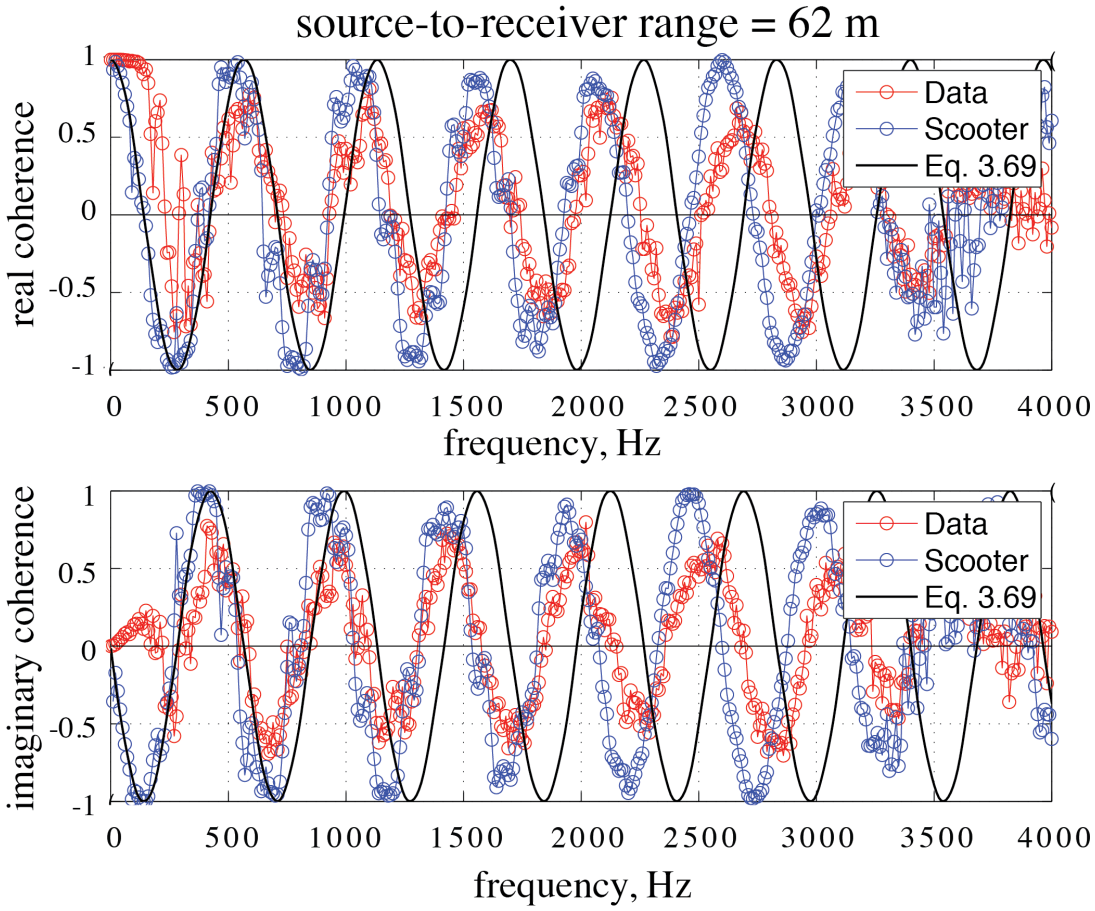

Figure 5.11: Real and imaginary parts of the coherence function versus frequency from two horizontally aligned hydrophones separated by 2.97 m. The red curves represent experimental data, the blue curves were computed using Scooter, and the black curves are from the analytical head-wave expression in Equation 3.69. The sediment sound speed used in evaluating Scooter and Equation 3.69 is $c_3 = 1682.42\ m/s$. The horizontal ranges between the source and the mean position of the two sensors is 62 m, too far for the head wave to be discernible.

For the helicopter range ($35\ m$) within the head-wave range window (Figure 5.10), all three curves, the data, the Scooter simulation, and the analytical head-wave expression in Equation 3.69, essentially overlay one another, with all the zero-crossings within the bandwidth of the helicopter source showing good agreement. At the shortest source range ($21\ m$), (Figure 5.9), the head-wave expression in Equation 3.69, does not match either the data or Scooter, though the latter two match each other. Equation 3.69 underestimates the zero crossings,

consistent with air-to-water refracted-ray arrivals, steeper than the critical grazing angle of the bottom, dominating the acoustic field in this regime. At the longest source range ($62\ m$), shown in Figure 5.11, Equation 3.69 again does not align with either the data or with Scooter, which match each other, but instead overestimates the zero crossings. This is consistent with normal mode domination of the field, since the modal equivalent rays are shallower than the critical grazing angle of the seabed.

5.5 Summary

In summary, the theoretical expression for the head-wave coherence function in Equation 3.69, evaluated with the estimated value of the sound speed in the sediment, $c_3 = 1682.42\ m/s$, closely matches both the helicopter-generated data and the numerical results from Scooter, as shown in Figure 5.10, when the R44 is within the head-wave range window. When the R44 is too close to or too far from the sensor station, the coherence data and Scooter match each other, but diverge from the characteristic form for the head wave in Equation 3.69, as illustrated in Figures 5.7 and 5.9, respectively. These observations are supportive of the conclusion reached earlier that the sediment sound speed can be recovered from a simple two-point measurement of the horizontal coherence function, provided the helicopter is within the head-wave range window.

Chapters 5, in part, is a reprint of the material as it appears in the Journal of the Acoustical Society of America: D. A. Bevans, M. J. Buckingham, “Estimating the Sound Speed of a Shallow-water Marine Sediment from the Head Wave Excited by a Low-flying Helicopter”,

142: 2273 (2017). The dissertation author was the primary investigator and author of this manuscript, and Dr. Michael J. Buckingham directed and supervised the research.

References

1. L. J. Hogarth, J. Babcock, N. W. Driscoll, et al.,"Long-term tectonic control on Holocene shelf sedimentation offshore La Jolla, California", Geology **35** (3), 275-278 (2007).

2. C.-T. Chen and F. J. Millero,"Speed of sound in seawater at high pressures", J. Acoust. Soc. Am., **62**, 1129-1135 (1977).

3. M. J. Buckingham,"Compressional and shear wave properties of marine sediments: Comparisons between theory and data", J. Acoust. Soc. Am., **117** (1), 137-152 (2005).

4. M. B. Porter,"The KRAKEN normal mode program", Report No. NRL/MR/5120-92-6920 **Naval Research Laboratory, Washington, DC** (1991).

Chapter 6

Concluding Remarks

5.1 Conclusions

The power spectral density of the sound produced by a Robinson R44 helicopter in a hover spans a bandwidth of approximately 2.5 kHz. When the helicopter operates at low level over the sea surface, some of this sound penetrates into the ocean and is incident upon the seabed, where it excites the head wave, which can be detected on a hydrophone provided the source is not too close to or too far from the receiver. From a two-point measurement on a pair of horizontally aligned hydrophones, the horizontal coherence function of the head wave can be formed, provided the source is within a source range window where the head wave is detectable.

A theoretical argument leads to an analytical expression, which indicates that the real and imaginary parts of the horizontal coherence function of the head wave, with the air- borne source in the end-fire position, are sinusoidal functions of frequency in quadrature with each other. Apart from frequency, these sinusoids depend only on the horizontal separation of the two sensors, which may be assumed known, and the sound speed in the sediment. It follows that a simple inversion procedure, based on matching the zeros in the analytical expression for the horizontal coherence function and the corresponding zeros in the coherence data, has potential for recovering the sediment sound speed.

To test this proposition, an experiment was performed in shallow water off the coast of southern California in which a horizontal line array of hydrophones, the FlyBy array, mounted 0.5 m above a fine- to very-fine sand seabed recorded the sound produced by a hovering

Robinson R44 helicopter in an end-fire position relative to the array. A comparison of the zeros in the head-wave coherence data and the corresponding zeros in the analytical expression for the head-wave coherence returns a sediment sound speed of $1682.42 \pm 16.20 m/s$, which is compatible with the known properties of the sediment at the experiment site.

The analytical model for the horizontal coherence of the head-wave holds only for source ranges within the head-wave range window. It is within this range window that the inversion for the sediment sound speed must be performed. As a check on the theoretical model, a numerical underwater- acoustic propagation code, Scooter, was used to compute the horizontal coherence at all source ranges, from overhead to well beyond the head-wave range window. The Scooter simulation shows very good agreement with the experimental horizontal coherence data at all the source ranges examined, both inside and outside the head-wave range window; and inside the head-wave range window, Scooter and the analytical model match very well.

In interpreting the helicopter-generated horizontal coherence function, it has been assumed that the sound speed profile in the sediment is essentially uniform. If, however, the sediment profile exhibited a positive gradient, upward refraction could occur giving rise to diving waves,[5] which could re-enter the water column and possibly be mistaken for the head wave. The re-entry angle of the diving waves would be range-dependent, which would be evident in the horizontal coherence function in the form of zero crossings that varied with source range. Throughout the head-wave range window, however, no such range dependence in the zero crossings is observed in the helicopter horizontal coherence data. Moreover, as illustrated in Figure 5.10 for the source within the head-wave range window, the horizontal coherence functions from the helicopter data and the Scooter simulation are in very good agreement. Indeed, this alignment between the data and the Scooter simulation is present at all source

ranges, and in particular at the beginning of the head-wave range window, where the head wave switches on within a very short range increment of about $1\,m$. Such behavior, which is characteristic of the head wave, is inconsistent with diving waves, essentially eliminating the possibility that the latter are significant in the helicopter- generated horizontal coherence data.

With the source at long ranges, well beyond the head- wave range window, it is possible that a surface-reflected head wave could be present in the horizontal coherence data. This would occur at a source range of about $70\,m$, but essentially no evidence of such a head wave can be seen either in the experimental data or in the Scooter simulation. Presumably the surface-reflected head wave is present but completely dominated by the normal mode component of the wave field.

To conclude, it has been demonstrated that a light helicopter such as a Robinson R44 has application as a low-frequency sound source for underwater acoustics experiments. At the shallow-water site where the experiments were performed, the underwater sound from the helicopter includes a head wave, which contains information about the sound speed in the sediment comprising the seabed. A simple inversion procedure, applied to the zeros in the horizontal coherence function of the helicopter-generated head wave, has been introduced, which returns an estimated sediment sound speed of $1682.42 \pm 16.2\,m/s$. This value is consistent with sediment type at the experiment site, which is known to be a fine to very-fine sand.

5.2 Head Wave Technique Applications

The head wave inversion technique developed throughout this work has several applications within underwater acoustics, particularly in recovering sediment sound speed in coastal regions and the in-situ measurement of sediment sound speed at low frequencies. Much of the seabed properties in shallow-water coastal regions remain unmapped. Due to this, it is common to have unknown sediment properties in areas where underwater acoustic experiments are conducted. Accurate seabed properties, such as sediment sound speed, are important in the processing of underwater acoustic data and real-world applications through ocean-acoustic propagation models. The accuracy of these models depends on the input of correct seabed and water column properties. The head wave technique provides a low-cost alternative for recovering the sediment sound speed to conventional ship-based seabed characterization. In using a helicopter as the source of acoustic excitation it also provides a low-cost alternative to an underwater low-frequency source. The low frequencies, $\sim 10\ Hz$, produced by the main rotor of the helicopter provide a useful test for theoretical model verification of compressional wave and shear wave propagation in unconsolidated marine sediments.

The technique that has been developed has particular application within the Navy. The Navy is well equipped to apply the head wave technique during operations in shallow water coastal regions. Helicopters in the Navy are used for many operations, one of which is to deploy sonobuoys. A sonobuoy is an expendable underwater sonar system contained in a canister that is dropped or ejected from an aircraft or ship. Once the sonobuoy enters the water and system is deployed from the canister separating into two parts. An inflatable surface buoy with a radio transmitter and GPS remains on the surface for communication with aircraft or ships, while

instruments descend below the surface to a pre-assigned depth. Typically the underwater components of a sonobuoy consist of stabilization components and one or more hydrophones, but can also consist of thermistors known as a bathythermobuoy. Sonobuoys consisting of multiple hydrophones have them arranged in various array configurations, one of which is a horizontal aperture of known sensor separation. A helicopter equipped with one or more sonobuoys, consisting of a horizontal aperture, would have the ability to recover the sediment sound speed through the head wave technique.

Operating in a region of unknown sediment properties, the Navy has the ability to deploy a helicopter equipped with sonobuoys with a horizontal aperture from land or ship. During the flight of the helicopter a single sonobuoy, for a point measurement, or multiple buoys can be deployed along a coastline or scattered within a bay. As the helicopter deploys the sonobuoys it can also drop a bathythermobuoy, which can recover the sound speed profile and the depth of the water column at each site. To recover the sediment sound speed within the frequency bandwidth of the helicopter, all that is required is an over-flight by the helicopter above each sonobuoy. This provides a valuable tool to collect additional information for operations within unknown coastal regions as well as the sediment sound speed for ocean-acoustic propagation models, which are used to track and locate objects within the water column.

The developed head wave inversion technique is can be applied to test theoretical models of wave propagation in unconsolidated marine sediments. For model verification, there is a pressing need for measurements as low as $10\,Hz$ of the phase speed and attenuation of compressional and shear waves in sand, silt, and clay sediments. Some, if not all, of these measurements could be recovered from the developed technique as the main rotor of the helicopter can produce these low frequencies. In Chapter 3, the sensor separation was shown to

dictate the lowest frequency, as well as the frequency separation, of the zero crossings of the horizontal coherence function of the head wave, Figure 3.7, providing a means to make these needed measurements.

The lowest frequency produced by the Robinson R44 helicopter main rotor, at operating RPM, is 13.3 Hz. The sediment sound speed at this low frequency can be recovered with a sensor separation of 32 m, assuming a $c_3 = 1700\ m/s$ in Equation 3.70. At such a large sensor separation the detection of the head wave over the propagating normal modes would be difficult at higher frequencies. This is due to the range intensity difference between the propagating normal modes and the head wave ($1/r^2\ vs\ 1/r^4$). This intensity dependence difference is overcome at lower frequencies $(< f_{cutoff})$, as frequencies below the modal cutoff frequency of the channel, Equation 2.3, do not propagate within the water column. This technique applied over a wide range of sensor separations, ranging from a meter to $10's$ of meters, would supply horizontal coherence zero crossings that would recover the sediment sound speed across the entire bandwidth of the helicopter.

Chapters 6, in part, is a reprint of the material as it appears in the Journal of the Acoustical Society of America: D. A. Bevans, M. J. Buckingham, "Estimating the Sound Speed of a Shallow-water Marine Sediment from the Head Wave Excited by a Low-flying Helicopter", 142: 2273 (2017). The dissertation author was the primary investigator and author of this manuscript, and Dr. Michael J. Buckingham directed and supervised the research.